INSTITUTO POLITÉCNICO NACIONAL
Centro de Investigación en Ciencia Aplicada y Tecnología Avanzada
Unidad Legaria

CICATA-LEGARIA

CONTRIBUCIÓN A LA CARACTERIZACIÓN TÉRMICA DE MATERIALES Y DETECCIÓN DE DEFECTOS SUB-SUPERFICIALES UTILIZANDO TERMOGRAFÍA INFRARROJA Y OTROS MÉTODOS DE GENERACIÓN DE IMÁGENES

Tesis que para obtener el grado de
Doctorado en Tecnología Avanzada presenta:

Angel Sergio Cifuentes Castro

Asesores de tesis:
Dr. Ernesto Marín Moares
Dr. Agustín Salazar Hernández

Ciudad de México, mayo, 2017

INSTITUTO POLITÉCNICO NACIONAL
Centro de Investigación en Ciencia Aplicada y Tecnología Avanzada
Unidad Legaria

CONTRIBUTION TO MATERIAL THERMAL CHARACTERIZATION TECHNIQUES AND SUBSURFACE DEFECT DETECTION USING INFRARED THERMOGRAPHY AND OTHER IMAGING METHODS

This dissertation is submitted to the National Polytechnic Institute for the degree of Doctor in Advanced Technology by:

Angel Sergio Cifuentes Castro

Advisors:

Dr. Ernesto Marín Moares

Dr. Agustín Salazar Hernández

Mexico City, May, 2017

eman ta zabal zazu

Universidad del País Vasco

Euskal Herriko Unibertsitatea

CONTRIBUTION TO MATERIAL THERMAL CHARACTERIZATION TECHNIQUES AND SUBSURFACE DEFECT DETECTION USING INFRARED THERMOGRAPHY AND OTHER IMAGING METHODS

This dissertation is submitted to the University of the Basque Country for the degree of Doctor in Science by:

Angel Sergio Cifuentes Castro

Advisors:

Dr. Ernesto Marín Moares

Dr. Agustín Salazar Hernández

Mexico City, May, 2017

Table of Contents

Acknowledgements

This work would not have been possible without the participation and support of different people and institutions. I would like to acknowledge the following institutions for their support throughout this PhD:

- *Consejo Nacional de Ciencia y Tecnologia (CONACyT), through their National Scholarship and Mixed Scholarship Program.*
- *Comisón de Operación y Fomento de Actividades del IPN (COFAA-IPN), for their financial support for attendance to different events and their BEIFI scholarship program.*
- *Centro de Investigación en Ciencia Aplicada y Tecnología Avanzada (CICATA) Legaria and Instituto Politécnico Nacinal, not only one of my home universities, but also their financial support for airfares without which this work would not have been possible.*
- *Universidad del País Vasco-/Euskal Herriko Unibertsitatea, Departamento de Física Aplicada I, my other home university for their support in bringing me in and their backing to ensure that my reasearch stays there were a success.*

I would also like to acknowledge the following people who through their support and encouragement made this PhD possible:

- *My thesis advisors, Ernesto Marín (IPN) and Agustín Salazar (UPV), and researcher Arantza Mendioroz (UPV) who were always there to guide my work and to whom I have a deep gratitude.*
- *My colleague and friend, Nelson Pech May (CINVESTAV), who collaborated with me in several experiments shown in this dissertation.*
- *Dr. Alberto Oleaga who managed all the administrative issues regarding my stay in Bilbao and was always there to help.*
- *The staff at the Advanced Technology Postgraduate Program at CICATA-Legaria.*

A special thank you is in order for my lab-mates and friends both at UPV and IPN, Vasyl, Kelly, Salvador, just to name a few. And finally, I would like to thank my family, friends and loved ones:

My mom and dad without them this would have been impossible. My brother and sister who were always there for me and Luis, Ander and Cindy, with whom I've shared countless moments and have been a major support during this time.

Resumen

Las técnicas basadas en el estudio de fenómenos de difusión térmica han demostrado, a través de varias décadas, su valor como herramienta en la caracterización de materiales y detección de defectos sub-superficiales. Estas técnicas tienen la ventaja de ser no invasivas y pueden, en muchos casos, ser configuradas de tal forma que la detección se pueda realizar de manera remota.

Esta tesis doctoral utiliza métodos de generación de imágenes para estudiar la difusión de calor en una muestra. Dos variantes principales fueron empleadas. La primera utiliza variaciones en el índice de refracción, inducidas térmicamente, en un fluido que rodea a la muestra para así evaluar el comportamiento de la temperatura en la superficie del objeto de estudio. Este fenómeno es comúnmente conocido como el efecto espejismo.

Las variaciones en el índice de refracción distorsionan el paso de haces de luz de prueba y esta distorsión es grabada utilizando cámaras de video digitales. Los resultados de estos experimentos pueden ser vistos en el capítulo dos de este trabajo, en donde se mide con éxito la difusividad térmica de múltiples muestras.

La segunda variante utilizada en este trabajo es la termografía. En esta técnica, un sensor de imagen que funciona en la porción infrarroja del espectro electro magnético es utilizada para cuantificar la radiación electromagnética que es emitida por la superficie de un objeto dado. Esta radiación infrarroja mantiene una relación con la temperatura la cual es descrita por la ley de Stefan-Boltzmann lo cual permite el estudio de la distribución térmica superficial en una muestra opaca.

Tres diferentes arreglos experimentales que utilizan termografía infrarroja son mostrados en el tercer capítulo. Dos de estos se basan en la ya bien conocida técnica de flash y demuestran la habilidad para estudiar tanto la difusividad como la efusividad térmica de forma simultánea en varias muestras. El otro arreglo experimental utiliza termografía con amplificación sensible a fase para estudiar la conductividad y difusividad térmica en malos conductores de calor mediante el análisis de su interacción con el aire circundante.

El último capítulo de este trabajo utiliza una cámara termográfica en la detección de defectos sub-superficiales al aplicar excitación ultrasónica sobre la muestra de tal forma que defectos de contacto dentro del objeto de estudio generen calor. La temperatura de superficie es registrada con la cámara termográfica y su evolución temporal es analizada de tal forma que permite la determinación de los parámetros geométricos del defecto. La técnica queda validada a través de trabajo experimental y simulación numérica.

Abstract

Techniques based in the study of thermal diffusion phenomena have proven throughout the last decades to be an important tool in material characterization and sub-superficial defect detection. These techniques have the advantage of being non-invasive and can, in many cases, be configured so that remote, non-contact sensing can be performed.

In this doctoral dissertation imaging methods have been used to study the diffusion of heat in a sample. Two main variants were employed. The first utilizes the thermally induced variations in the refractive index of a fluid surrounding a sample to indirectly evaluate the behavior of the temperature of the sample surface.

This is a phenomenon commonly known as the “mirage effect”. These variations distort the path of probe lighting and this is in turn recorded using a camera. The results of these experiments can be seen in chapter two where two different experimental configurations are employed to successfully measure thermal diffusivity.

The second variant used for this work is thermographic imaging. In this sensing technique, an imaging sensor working on the infrared (IR) part of the electromagnetic spectrum is used to assess the electromagnetic radiation being emitted from the surface of an object. This IR radiation holds a relation to the temperature of the object as described by the Stefan-Boltzmann law allowing us to study thermal distribution on the opaque sample surface.

Three different experimental set-ups are shown in chapter three. Two of these rely on the well-known flash technique and show the ability to study the thermal diffusivity and effusivity simultaneously in a variety of samples. The other set-up uses lock-in amplified thermographic images to study the thermal conductivity and diffusivity in poor heat conductors by analyzing their interaction with the surrounding air.

The last chapter of this dissertation utilizes a thermographic camera in the detection of sub-superficial defects. Ultrasonic excitation is applied to a sample so that contact defects within the object generate heat. This technique is commonly known as vibrothermography. The surface temperature is then recorded and its temporal evolution is studied so that the geometry of the defect can be recovered. Experimental work and numerical simulations are used to validate the technique.

Resumen Extendido

El estudio de las ciencias térmicas ha traído consigo grandes avances científicos a través de la historia. Desde la teoría del calórico de Lavoisier, pasando por la acertada descripción de fenómenos de difusión térmica dada por Joseph Fourier hasta hoy en día cuando una gran cantidad de nuevas tecnologías nos han dado la capacidad de estudiar fenómenos térmicos en un detalle que anteriormente habría resultado difícil de imaginar.

Es el objetivo de este trabajo demostrar que la caracterización de la difusividad térmica de materiales utilizando el efecto espejismo puede ser realizada utilizando sensores de imagen, tanto de grado científico como comercial. También se pretende exponer que la caracterización térmica puede ser realizada utilizando cámaras termográficas, las cuales proveen una resolución temporal, espacial y de temperatura lo suficientemente alta como para utilizar modelos más sofisticados que permiten la completa caracterización térmica de un material a través de, no solo su difusividad, sino también su conductividad o efusividad térmica. Además, en el presente trabajo, se demuestra la habilidad de utilizar estas cámaras en la detección de defectos no superficiales utilizando fuentes de excitación ultrasónica y modelos de difusión térmica.

La caracterización térmica de materiales requiere del entendimiento de diferentes tipos de fenómenos generados cuando ocurre la transferencia de calor. Es a través del estudio de estos fenómenos que el investigador puede determinar los parámetros térmicos en una muestra dada. En el primer capítulo de esta tesis doctoral se exploran los diferentes tipos de mecanismos de transferencia de calor:

- Convección
    - La convección transfiere la energía térmica de una superficie a un fluido adyacente, el cual puede ser un líquido o un gas. El fluido en contacto térmico con la superficie es calentado a través del proceso de conducción y luego este calor es arrastrado a través del movimiento macroscópico del fluido (flujo). Entre mayor es el flujo mayor es la transferencia de calor por convección.
- Radiación
    - Todo cuerpo en el universo que se encuentra a una temperatura mayor a la del cero absoluto emite radiación. Esta emisión puede ser atribuida a cambios en la configuración electrónica de los átomos que conforman la materia. La transferencia de calor radiativa no requiere un medio para transportar la energía ya que este transporte se realiza a través de ondas electromagnéticas las cuales pueden viajar a través del vacío. Este es de hecho el mecanismo que transfiere calor del sol a la tierra.
- Conducción

- La conducción es el modo de transferencia de calor mediado por actividad atómica y molecular. La transferencia de energía ocurre desde partículas de mayor energía en una sustancia a aquellas de menor energía debido a las interacciones entre ellas. La conducción ocurre en sólidos, líquidos y gases y es comúnmente la forma de transferencia de calor más importante dentro de un sólido o sólidos en contacto.
- En sólidos, la conducción puede ser atribuida a las vibraciones de moléculas en una red en forma de fonones y/o por el transporte de electrones libres. Una mayor energía molecular estará asociada con una mayor temperatura. En el caso de líquidos y gases, las partículas están libres de una red y son capaces de moverse. Cuando las partículas colisionan ocurre la transferencia de energía. Cuando existe un gradiente de temperatura se genera la conducción de calor en dirección a la menor temperatura.

En muchos escenarios experimentales las fuentes de calor utilizadas son de una naturaleza periódica. Esto ha llevado a muchos autores a adoptar los principios introducidos por la física de ondas en fenómenos electromagnéticos y acústicos para describir las fluctuaciones periódicas de temperatura.

El tratamiento de fuentes de calor periódicas como ondas data tiempos de Joseph Fourier quien en 1822 a través de su trabajo titulado "*La theorie analytique de la chaleour",* demostró que los problemas de conducción de calor podían ser descritos al expandir las distribuciones de temperatura en una serie de ondas.

Las ondas térmicas son de sumo interés para el entendimiento de los fenómenos fototérmicos. Una gran cantidad de técnicas no destructivas han sido basadas en fenómenos de difusión térmica ondulatorios y han sido correctamente descritos utilizando la física de ondas térmicas. Estas técnicas permiten la caracterización térmica de materiales, la determinación de espectros de absorción e incluso la detección de defectos ocultos en diferentes tipos de muestras entre muchas aplicaciones.

Diferentes parámetros físicos; como por ejemplo la densidad, la conductividad térmica o la capacidad calorífica juegan un papel en los fenómenos de difusión de calor. Esto permite el estudiar dichos fenómenos a través de las variaciones inducidas en estos parámetros. Un parámetro que varía de forma importante con la temperatura y es utilizado en este trabajo es la variación del índice de refracción en un medio. Esta variación, conocida como efecto espejismo, es utilizada en el segundo capítulo de este trabajo para estudiar distribuciones de temperatura.

La variación del índice de refracción debida a la temperatura genera un gradiente de índice de refracción. Bajo ciertas condiciones el investigador es capaz de estudiar la distribución de temperatura en una muestra solida de forma indirecta utilizando el gradiente generado en el medio circundante.

El capítulo numero dos propone dos diferentes configuraciones experimentales utilizando cámaras y procesamiento digital de video en las cuales permiten obtener la difusividad térmica de una muestra sólida en contacto con un fluido:

- Deflexión fototérmica de múltiples haces:

  Esta configuración es una variante del ya demostrado método de deflexión de haz ortogonal. Un láser de bombeo es enfocado en un área pequeña en la superficie de la muestra y es modulado para generar ondas térmicas. Estas ondas se propagan a través de la muestra y calientan el medio circundante. Las variaciones de temperatura en el medio se traducen en variaciones del índice de refracción. La disparidad en el índice de refacción produce una deflexión el un haz de luz de prueba atravesando el medio. Esta deflexión es tradicionalmente detectada utilizando un fotodetector de cuadrante.

  Para este trabajo se plantea utilizar el método de la pendiente de la fase para la determinación de la difusividad térmica. Este método ha sido ampliamente utilizado por múltiples autores, su popularidad se debe a su simplicidad. El método requiere el conocimiento de la variación en fase de las ondas térmicas con la distancia. Al graficar esta fase,ϕ, contra la distancia,r, se obtiene una línea recta cuya pendiente, m, está relacionada con la difusividad térmica, α, y la frecuencia de modulación f de la siguiente forma:

$$-m_{\phi} = \sqrt{\frac{\pi f}{\alpha}}$$

  Usualmente el experimentador debe de hacer un barrido en distancia con el haz de prueba y estudiar el desfasamiento en cada punto. Este barrido puede ser tardado en dependencia de la cantidad de puntos que se desean obtener. Aquí proponemos el utilizar una cámara para grabar la deflexión de múltiples haces de forma simultánea, eliminando la necesidad de hacer un barrido y optimizando así el proceso de medición. Esto se logra grabando un video y haciendo un post-procesamiento de amplificación sincrónica para lograr extraer la fase de la deflexión del haz de forma precisa. El trabajo se sustenta mostrando mediciones experimentales de muestras patrón.

- Método de sombras fototérmico.

  Se presenta una novedosa aplicación del método de sombras (shadowgraph) para obtener la difusividad térmica de un sólido opaco. Esta variante utiliza la sombra proyectada por la muestra cuando se interpone a un haz de luz colimado. La muestra es calentada periódicamente utilizando un haz de bombeo lo cual genera ondas térmicas las cuales se propagan dentro de la muestra y a sus alrededores. Los cambios en el índice de refracción en el medio circundante distorsionan la sombra. El fenómeno es videograbado y amplificado

sincrónicamente para lograr determinar la difusividad térmica de la muestra por medio del método de la pendiente de la fase.

Se expone una simulación del método tomando en cuenta una muestra en forma de filamento. La simulación confirma la validez del método de la pendiente para la fase cuando la difusividad y conductividad térmica del medio son mucho menores a los de la muestra. Además, se muestran resultados experimentales con muestras patrón, las cuales validan el método.

En este experimento se hace uso de una cámara científica FLIR SC2500 para la mayoría de las mediciones. También se demuestra la posibilidad de utilizar una cámara web para estudiar las distorsiones en la sombra, haciéndolo un método sumamente asequible.

El tercer capítulo de este trabajo explora la caracterización térmica de materiales utilizando cámaras termográficas. Se exploran métodos resueltos en tiempo y resueltos en frecuencia. La termografía utiliza arreglos de detectores sensibles a radiación electromagnética con longitud de onda en el infrarrojo. Al medir la intensidad de esta radiación utilizando un arreglo de plano focal se logra hacer un mapeo o imagen el cual está directamente relacionado con la distribución de temperatura del objeto. Cada sensor dentro de este arreglo es responsable de generar un pixel en la imagen. Esto permite estudiar la difusión espacial del calor. También permite utilizar la gran cantidad de pixeles para hacer un promedio y obtener niveles de ruido muy bajos ($\sim 3mK$).

Los experimentos reportados en este capítulo permiten la completa caracterización térmica de las muestras a medir. Todas las técnicas determinan la difusividad térmica mientras que las técnicas de flash reportadas aquí ofrecen la capacidad de obtener la efusividad térmica, ϵ. Además, mostramos un experimento utilizando termografía sensible a fase el cual permite la obtención de la conductividad térmica, k. Estas cantidades están relacionadas entre sí por las siguientes expresiones.

$$\alpha = \frac{k}{\rho c_p} \; y \; \epsilon = \sqrt{k \rho c_p}$$

donde ρ es la densidad y c_p es la capacidad calorífica específica.

Se reportan dos experimentos resueltos en tiempo basados en la técnica de flash:

- Medición simultánea de difusividad y efusividad térmica en solidos utilizando la técnica de flash en la configuración de cara frontal.

  Esta técnica, basada en la ya conocida técnica de flash utiliza la interacción de una muestra con un medio líquido en su cara trasera para permitir la determinación tanto de la

difusividad como efusividad térmica, ofreciendo así una caracterización térmica completa de la muestra.

La técnica de flash es uno de los métodos más utilizados para medir la difusividad térmica. Involucra el calentar la cara frontal de una placa ópticamente opaca utilizando un pulso de luz de corta duración y alta energía. En la configuración de cara frontal se estudia la evolución de la temperatura en dicha superficie. Sin embargo, en la técnica tradicional solo resulta práctico el obtener la difusividad térmica ya que la conductividad térmica aparece acoplada a la cantidad de energía absorbida; la cual resulta en la mayoría de los casos difícil de medir con exactitud.

Este trabajo demuestra que al utilizar un fluido en la cara trasera de la placa se puede conseguir medir los valores de difusividad y efusividad térmica mediante un ajuste multiparamétrico a un modelo matemático que toma en cuenta la interacción con el fluido. El estudio se valida tanto en simulación como de forma experimental además de explorar las limitantes de la técnica.

- Estudio de las propiedades térmicas de composites de poliéster cargados con nano-fibras de carbono orientadas utilizando la técnica de flash en su configuración de cara frontal.

  El incrementar la conductividad térmica en composites de poliéster ha sido un tema de interés en diferentes áreas como por ejemplo en la industria aeronáutica. Es conocido que el utilizar nano-fibras de carbono incrementa la conductividad del composite. Para facilitar la alineación de estas fibras dentro de la matriz empleando un campo magnético se utilizan nano-fibras con nanopartículas de hierro. Esta alineación tiene un fuerte impacto en las propiedades térmicas efectivas del material. Es la medición de estas propiedades efectivas la que resulta de interés para este trabajo.

  En este estudio se demuestra la capacidad de la técnica de flash en su configuración de cara frontal para medir la efusividad y la difusividad térmica en estos materiales.

Dentro de este capítulo también se incluye una técnica resuelta en frecuencia:

- Medición simultanea de la difusividad y conductividad térmica en aislantes térmicos utilizando termografía infrarroja sensible a fase.

  La termografía infrarroja sensible a fase es un método de caracterización dinámico que consiste en iluminar la muestra con un haz de luz de intensidad modulada y registrar el componente oscilatorio en la elevación de la temperatura utilizando una cámara termográfica.

Utilizando un haz de luz fuertemente enfocado sobre la muestra se utiliza la fase y amplitud de la onda térmica para recuperar la difusividad y conductividad térmica al tomar en cuenta el efecto de la conducción de calor al aire circundante. El método resulta apropiado para malos conductores de calor ya que la interacción de estos con el aire es mayor. Dado que las propiedades del aire circundante son conocidas un ajuste multiparamétrico a un modelo matemático que toma en cuenta estas interacciones permite la obtención de la difusividad y conductividad térmica a partir de una sola medida. El método ha sido validado experimentalmente y a través de un análisis de sensibilidad.

El capítulo número cuatro, el último de este trabajo doctoral, trata con una técnica de ensayo no destructivo capaz de detectar defectos sub-superficiales. La técnica es conocida por muchos como vibrotermografía e involucra el muestreo de la integridad y uniformidad interna de una muestra utilizando una cámara termográfica para observar el patrón de temperatura producido por la disipación de energía que ocurre cuando una excitación vibratoria es aplicada en dicha muestra. La técnica requiere que la muestra sea sometida a vibraciones mecánicas usualmente generadas por ultrasonido.

El defecto convierte la energía mecánica en energía térmica principalmente por fricción. Esta energía térmica se propaga a través del objeto hasta llegar a la superficie donde es observado a través de una cámara infrarroja.

La técnica propuesta en este trabajo hace uso de un modelado matemático resuelto en tiempo lo cual ofrece mediciones rápidas de un par de segundos de duración. La medición es grabada por la cámara termográfica para después realizar un ajuste multiparamétrico donde las variables geométricas del defecto son los parámetros a ajustar.

La técnica ha sido validada experimentalmente utilizando una serie de defectos sub-superficiales calibrados para geometrías rectangulares y semicirculares. Este trabajo demuestra que se puede obtener un buen estimado de las características geométricas de dichos defectos utilizando mediciones cortas, lo cual resulta de alto interés en diferentes aplicaciones.

El presente trabajo doctoral demuestra la utilización de sensores de imagen para el estudio de fenómenos de difusión de energía térmica. Las principales ventajas vistas al utilizar este tipo de sensores es la capacidad de resolver el comportamiento espacial de campos temperatura y la habilidad de mitigar el ruido aleatorio en una medición al utilizar el promedio de un alto número de pixeles.

Introduction

Motivation

The study of thermal sciences has entailed a great deal of scientific advances throughout history. From Lavoisier's caloric theory, where heat was envisioned as an invisible substance that seemed to flow from one body to another to the accurate description of the thermal diffusion phenomena given by Joseph Fourier, to now in days, when a vast number of new technologies have given us the ability to study thermal phenomena in detail and develop new, better and improved techniques that have led to many advances in material science. This historic testament leaves no doubt of the importance of studying and understanding the transfer of heat.

Advances in the fields of electronics have given us new and improved imaging sensors. This work utilizes these imaging sensors, going from simple webcams to sophisticated thermal cameras, to perform thermal science based measurements. These cameras are used to obtain spatially varying temperature information or to obtain high signal to noise ratios, the data is then processed and interpreted through adequate theoretical models. Many of these models may be understood through the concept of thermal wave physics (Chapter 1).

It's the development of new and improved techniques that motivates this work. Bringing the theoretical science developed over the years into procedures that allow for improvements in the thermal characterization of materials (Chapters 2 and 3) and, through the same theoretical framework, the detection of hidden defects (Chapter 4).

Thesis Statement

This work will show that thermal characterization, namely measurement of thermal diffusivity, through the mirage effect (Chapter 2) can be done using imaging sensors, both scientific grade and commercial grade. It will also be seen that thermal characterization of materials can be effectively carried out using thermal imaging cameras, which provide the high temporal, spatial and temperature resolution to use more sophisticated models that allow for full thermal characterization of materials obtaining the thermal diffusivity and either the thermal effusivity or conductivity (Chapter 3). Finally results showing the detection and sizing of sub-superficial defects using a thermal imaging camera and ultrasonic excitation (Chapter 4).

1. Introduction to thermal characterization of materials using thermal waves and transient phenomena.

The thermal characterization of materials requires the understanding of the different phenomena involved when heat transfer (the transit of thermal energy) occurs. It is through the study of these phenomena that the researcher can determine the thermal parameters that characterize a given sample. It is the aim of this chapter to provide a brief and concise overview of these phenomena so that the following chapters will be clearer to the reader.

1. Heat transfer mechanisms

Heat transfer is defined as the process by which thermal energy is exchanged between systems by means of different mechanisms. The transfer of heat occurs when a thermal gradient is in existence or when two or more systems at different temperatures are put in contact. The process persists until thermal equilibrium (no heat flow between systems) is reached, i.e. when the temperature gradient ceases to exist or the temperature of the systems becomes the same. (Bergman and Incropera 2011)

The first law of thermodynamics tells us that for a closed system the heat transfer rate, Q, will equal the sum of the work transfer rate, W, and the change in internal energy, U, with respect to time, t.

$$Q = W + \frac{\mathrm{d}U}{\mathrm{d}t} \tag{1.1}$$

For processes that take place at constant volume regardless of pressure variations, as is the case for condensed matter samples, a good approach for equation 1.1 is

$$Q = \frac{\mathrm{d}U}{\mathrm{d}t} = mc\frac{dT}{dt} \tag{1.2}$$

$$\Delta U = mc\Delta T \tag{1.3}$$

where m is the mass, T the temperature and c is the specific heat of the material. The specific heat is defined as the change in the internal energy of a substance per unit of mass per unit of temperature and its units are J/kgK. The product of the mass density, ρ (kg/m^3) and the specific heat is called the (volumetric) specific heat capacity C (J/m^3K).

$$\mathrm{C} = \rho c \tag{1.4}$$

Three different heat transfer modes or processes exist:

- Conduction is said to occur when the thermal energy transit is given across a medium, or mediums, due to direct contact between their molecules.

- Convection involves the transport of heat by a moving fluid (liquid or gas), be it forced or natural.
- Radiative heat transfer transports thermal energy by means of electromagnetic radiation.

In many cases the total transfer of heat must be explained by a combination of the three modes listed above. Below, a more complete description of each transfer mode is presented.

Convection

Convection transfers thermal energy between a surface and an adjacent, flowing, liquid or gas. Basically, the fluid receives thermal energy through contact with a hot body or surface (through conduction), and then drags it away through the macroscopic motion of the fluid. The faster the flow the larger the convective heat transfer.

Forced convection implies that the flow is initiated by artificial means, e.g. a fan aimed at a car radiator. Natural convection arises from the temperature dependence of density in a fluid. Let us imagine a pot full of water being heated by a candle. Warm water is less dense then cold water. The water at the bottom of the pot will warm up and "float" to the surface. The cold water on the surface will then be displaced by the warm water and eventually encounter the hot surface at the bottom, the surface will once again transfer its heat to this water and propel it upward. This cyclical fluid motion provides the flow required by convection.

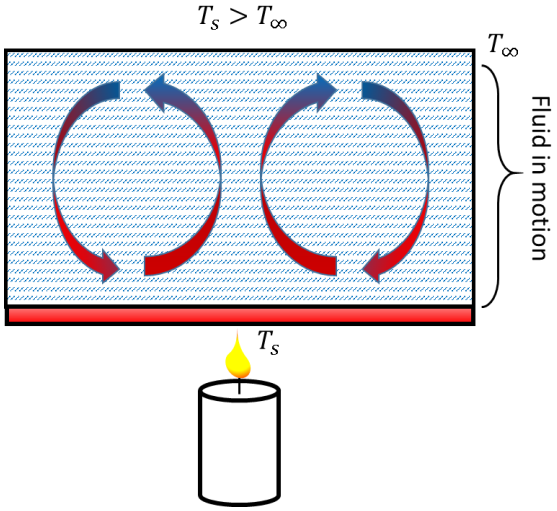

FIGURE 1-1 CONVECTION OF A LIQUID IN A CONTAINER BEING HEATED BY A CANDLE

Although convection is a complex process and its analysis is more often than not only solvable by numerical means (Marín, Calderón et al. 2009), in its most simple form the rate of convection heat transferred is proportional to the temperature difference, this is expressed by Newton's law of cooling:

$$\mathrm{q_{conv}} = h_{conv} A (T_s - T_\infty) \qquad (1.5)$$

Where q_{conv} is the convective heat flux (W/m^2) and the parameter h_{conv} (W/m^2K) is known as the convection heat transfer coefficient. This coefficient depends on the conditions found at the boundary layer between the hot surface or body and the fluid and is influenced by surface geometry and fluid properties.

Radiative heat transfer

Every single body in the universe with a nonzero temperature emits electromagnetic (EM) radiation. This emission can be attributed to the changes in the configuration of electrons of the constituent atoms or molecules (Modest 2003). Radiative heat transfer requires no medium to convey energy since this transport is carried out by electromagnetic waves, which can travel through vacuum. This is in fact how the energy of the Sun reaches Earth.

In the case of an opaque solid bounded by a surface, radiation will be emitted from the same surface due to the thermal energy of the bounded matter. If the body is a perfect emitter (blackbody) its emissive power will be given by the Stefan-Boltzmann law:

$$E_b = \sigma T_S^4 \tag{1.6}$$

Where T_s is the body's absolute temperature measured in Kelvin, and σ is the Stefan-Boltzmann constant ($\sigma = 5.67\times10^{-8} W/m^2K$). In the case of a non-blackbody radiator, i.e. a real body, the emissivity, ε, must be considered. This property provides a measure of how efficiently a surface emits radiation relative to a black body and can only take values from 0 to 1, with 1 being a blackbody and 0 a perfect reflector.

$$E_b = \varepsilon\sigma T_S^4 \tag{1.7}$$

Radiation may also be incoming or incident to a body, in this case, part of this energy may be absorbed. While emissivity tells us how well a body emits radiation, absorptivity α tells us how well a body absorbs it. Again, this property is bound to values between 0 to 1. A blackbody will also have an absorptivity equal to 1.

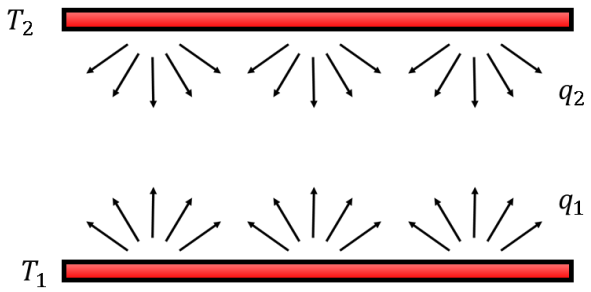

FIGURE 1-2. RADIATIVE HEAT TRANSFER BETWEEN TWO FLAT SURFACES

If a surface of emissivity ε is fully enclosed by a much larger surface at a temperature T_0 and they are separated by a medium which does not intervene with radiation and, if the surface

can be thought of as a gray surface, i.e. $\alpha = \varepsilon$, the heat transfer rate or heat flux,q_{rad}, between these two surfaces expressed per unit of area will be:

$$q_{rad} = \varepsilon\sigma A(T_s^4 - T_0^4) \tag{1.8}$$

It is important to note that radiative heat transfer is proportional to the fourth power of the temperature. This means that its importance will increase in a nonlinear fashion with increasing temperature.

The heat flux density can be obtained simply by dividing the heat flux by the area of the surface (equation 1.9).

$$\Phi_{rad} = \frac{q_{rad}}{\mathrm{A}} \tag{1.9}$$

Φ_{rad} is the area under the curve that describes the wavelength dependence of the spectral intensity emitted by a warm (nonzero temperature) body, I_λ. For a blackbody (i.e. $\varepsilon = 1$) the spectral intensity is described by Plank's law (equation 1.10).

$$I_\lambda = \frac{2\pi hc^2}{\lambda^5}\frac{1}{e^{\frac{hc}{\lambda k_b T}} - 1} \tag{1.10}$$

Where the Planck constant $h \cong 6.626\times10^{-34}(J \cdot s)$ and the Boltzmann constant $k_b \cong 1.380\times10^{-23}(J \cdot K^{-1})$. As the temperature of the emitting body increases the spectral intensity will be shifted toward shorter wavelengths.

$$T\lambda_{max} = b \tag{1.11}$$

Wien's displacement law describes this behavior (equation 1.11). This law states that the product of λ_{max} ,the wavelength corresponding to the maximum of the Planck law spectrum, and given temperature T will result in a constant $b \approx 2900\ (\mu m \cdot K)$ (Wien's constant).

If we take a closer look at equation 1.8, and assume a small temperature difference between the surroundings and the object in question, a Taylor series expansion around T_0 gives rise to the following linear relation:

$$q_{rad} = 4\varepsilon\sigma T_0^3 A(T_s - T_0) = h_{rad} A\Delta T \tag{1.12}$$

This relation allows us to make an analogy to equation 1.5 and define a radiation heat transfer coefficient, $h_{rad} = 4\varepsilon\sigma T_0^3$ (Marín 2009).

Just as heat generates EM radiation, EM radiation generates heat. When a source of light is shined on to a material the material will experience heating. This is known as the photothermal effect.

Conduction

Heat conduction is a mode of heat transfer mediated by atomic and molecular activity. The energy transfer occurs from the more energetic to the less energetic particles in a substance due to interactions between them. Conduction takes place in solids, liquids and gases and is usually the most important form of thermal transport within a solid or solid objects in thermal contact.(Çengel 2008)

In solids, conduction can be attributed to the vibrations of molecules in a lattice, in the form of lattice waves or phonons, and/or the transport by free electrons. Higher molecular energy will be associated with higher temperature. In the case of liquids and solids the particles are free of a lattice and capable of moving. When adjacent particles collide, energy transfer occurs. If a temperature gradient exists the transfer occurs in the direction of decreasing temperature giving rise to heat conduction.

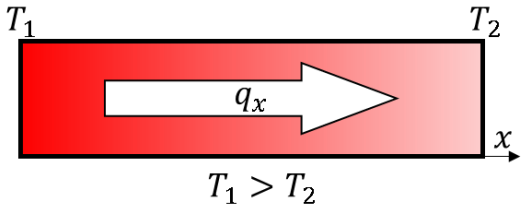

FIGURE 1-3. CONDUCTION OF HEAT THROUGH A SOLID

The heat conduction rate across a medium will depend on its geometry, thickness and the temperature differential.

Fourier's Law

Fourier's law of thermal conduction states that the rate of heat transfer through a material will be proportional to the negative temperature gradient and to the normal area to that gradient through which heat flow will occur (Bergman and Incropera 2011). It is important to note that Fourier's law is applicable to non-time varying temperature gradients. In the case of conduction through an isotropic homogenous material in a single dimension Fourier's law can be expressed as follows:

$$q_x = -k\frac{dT}{dx} \tag{1.13}$$

Where the heat flux q_x (W/m^2) is the heat transfer rate in the x direction. The heat flux is the rate of heat transfer per unit area. The parameter $k(W/mK)$ is a thermal property known as thermal conductivity and is characteristic of each material; it is a measure of the ability of a material to conduct heat. A more generalized form of Fourier's law, where conduction may occur in any direction, can be written in differential form as follows:

$$\vec{\mathrm{q}}_{cond} = -kA\vec{\nabla \mathrm{T}} \tag{1.14}$$

A high thermal conductivity indicates a material which is a good heat conductor while a low value indicates that the material is a poor heat conductor also known as a thermal insulator. Thermal conductivity is an important parameter in many areas of science and engineering.

For one dimensional steady state conduction in extended homogeneous and isotropic samples with a small temperature gradient Fourier's law can be expressed as follows:

$$q_{cond} = \mathrm{k}A\frac{T_2 - T_1}{x_2 - x_1} = \frac{kA\Delta T}{L} = h_{cond}A\Delta T \tag{1.15}$$

In this case T_1 and T_2 represent to planar isotherms at positions x_1 and x_2 and $L = x_1 - x_2$

Thermal conductivity's reciprocal is known as thermal resistivity, from which a thermal resistance (an analogue to electrical resistance) can be calculated for a material of a given thickness. Thermal resistance indicates the ability of a material to oppose heat flow. From Fourier's law one may derive the following expression for thermal resistance *R*:

$$R = \frac{L}{A \times k} \tag{1.16}$$

where A, is the cross-sectional area perpendicular to the heat flow.

The heat equation

Fourier's law works well for non-time varying systems but it fails to describe conductive heat transfer phenomena when time varying temperature gradients are found. A more complete formulation is required, this is where the heat equation comes in.

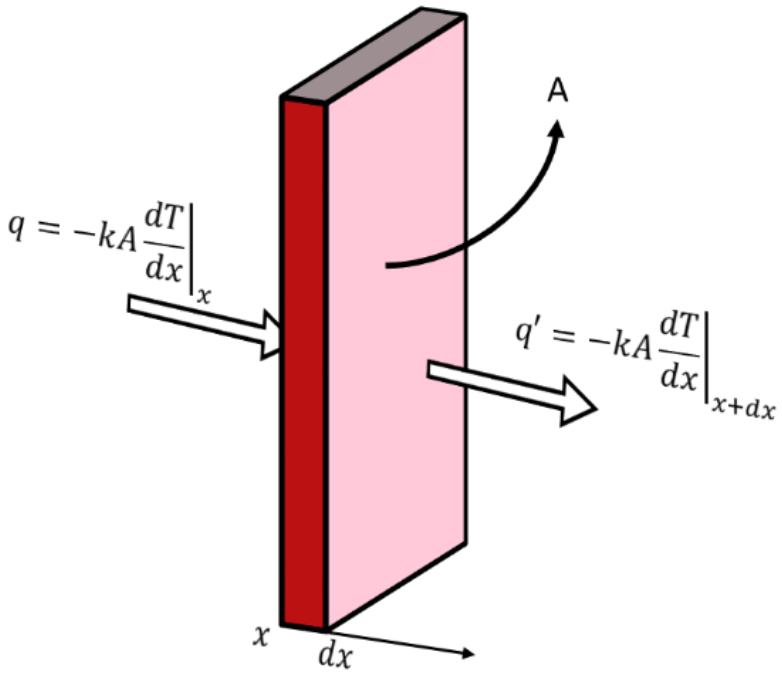

FIGURE 1-4. ILLUSTRATION FOR THE DEDUCTION OF THE THERMAL DIFFUSION EQUATION. THE SLAB IS CONSIDERED TO BE VERY THIN ($dx = \delta x$, WHERE $\delta x \to 0$)

Consider the problem depicted in Figure 1-4. The net heat flux can be written as:

$$q_{net} = -kA\left\{\left.\frac{\partial T}{\partial x}\right|_{x+\delta x} - \left.\frac{\partial T}{\partial x}\right|_{x+dx}\right\} = -kA\left\{\frac{\left.\frac{\partial T}{\partial x}\right|_{x+\delta x} - \left.\frac{\partial T}{\partial x}\right|_{x+dx}}{\delta x}\right\}\delta x = -kA\frac{\partial^2 T}{\partial x^2} \quad (1.17)$$

The temporal change of the volumetric internal energy, U, of a system is related to the net heat flux, q_{net}, through the first law of thermodynamics for a closed incompressible system (conservation of energy).

$$\frac{\partial U}{\partial t} = mc\frac{\partial T}{\partial t} = -q_{net} \quad (1.18)$$

By substituting equation 1.17 into equation 1.18 and considering that the mass can be expressed as $m = \rho\delta V = \rho A\delta x$ where δV is the sample volume and ρ is its mass density we can obtain the following equation(Çengel 2008):

$$\nabla^2 T - \frac{1}{\alpha}\frac{\partial T}{\partial t} = 0 \quad (1.19)$$

where the thermal diffusivity α (m^2/s) is a thermal property of the material and is related to the thermal conductivity and heat capacity as follows:

$$\alpha = \frac{k}{\rho c} \tag{1.20}$$

Equation 1.19 is the homogeneous parabolic heat diffusion equation. It is the equation that describes heat transfer in non-stationary systems. If internal heat sources are included in the analysis seen above than the heat diffusion equation will take the following form:

$$\nabla^2 T - \frac{1}{\alpha}\frac{\partial T}{\partial t} = -\frac{Q}{k} \tag{1.21}$$

Thermal diffusivity is associated with the heat propagation speed during changes of temperature over time (Salazar 2003). In a material with a high thermal diffusivity heat will move rapidly because the substance will conduct heat faster relative to its capacity to store it. A material with a small heat capacity or large thermal conductivity is bound to have a large thermal diffusivity.

2. Thermal waves

In many experimental settings heat sources are periodic. This has led many authors to adopt the principles set by wave physics used in phenomena such as electromagnetic and sound wave propagation to describe periodic heat fluctuations.

The treatment of periodic heat sources as waves dates back to the days of Jean Baptiste Joseph Fourier who, in his 1822 work *La theorie analytique de la chaleour,* showed that heat conduction problems could be described by expanding temperature distributions into a series of waves (Fourier 2009).

Thermal waves are of great interest for the understanding of the photoacoustic effect and other photothermal phenomena. Many non-destructive techniques have been based on wave-like thermal diffusion in materials and have been successfully described using thermal wave physics. (Marín 2009)

The following subsections will provide the reader with a concise overview of the thermal wave phenomena, the physics behind it and the different experimental schemes and detection methodology.

The mathematics behind thermal waves

Let us consider an isotropic homogeneous semi-infinite solid. The surface of said solid is being uniformly heated by an intensity modulated periodical light source:

$$I(t) = \frac{I_0}{2}\Re[(1 + e^{i\omega t})] \tag{1.22}$$

where I_0 (J/m^2) is the intensity's amplitude and ω is the angular modulation frequency and t is time. The hypothetical solid, of thermal diffusivity α, can absorb all incoming radiation on its surface and turn it into heat, in addition any heat transfer through radiation or convection can be neglected. Under these assumptions, the temperature distribution of the solid can be calculated using equation 1.19, i.e. the heat diffusion equation, using the following boundary condition:

$$-k\frac{\partial T(x,t)}{\partial x}\bigg|_{x=0} = \frac{I_0}{2}\Re[(1 + e^{i\omega t})] \tag{1.23}$$

The oscillatory solution is of interest for most applications and it can be split from the spatial distribution and expressed as:

$$T(x,t) = \Re[\theta(x)e^{i\omega t}] \tag{1.24}$$

this leads to:

$$\frac{\partial^2\theta(x,t)}{\partial x^2} - q^2\theta(x) = 0 \tag{1.25}$$

where the complex thermal wave number $q = \sqrt{i\omega/\alpha} = (1+i)/\mu$. The thermal diffusion length, μ, is defined bellow.

$$\mu = \sqrt{\frac{2\alpha}{\omega}} \tag{1.26}$$

The general solution for the oscillatory component of the heat diffusion equation utilizing the boundary condition seen above is:

$$\theta(x) = \frac{I_0}{2\epsilon\sqrt{\omega}} e^{-\frac{x}{\mu}} e^{-i\left(\frac{x}{\mu}+\frac{\pi}{4}\right)} \tag{1.27}$$

The parameter ϵ is the thermal effusivity of the sample:

$$\epsilon = \frac{k}{\sqrt{\alpha}} = \sqrt{k\rho c} \tag{1.28}$$

The thermal effusivity is an important parameter under non-stationary conditions and gives us a measure of the thermal inertia. It is of uttermost importance in problems involving the heating of surfaces and in multilayer systems. It will determine the superficial temperature and is a measure of the ability of the material to exchange heat with the environment (Salazar 2003) .

Equation 1.27 has the form of a plane wave, and like other wave types, it has an oscillatory response in space (e^{iqx}). This is what is known as thermal wave and the product of its first spatial derivative and thermal conductivity of the medium represent a heat flux wave.

It is important to note that, although the treatment of oscillatory thermal fields as waves works and simplifies the analysis of many systems, thermal waves are not real waves, they are temperature oscillations with wave-like features but fail to satisfy all the characteristics of a true wave, e.g. the transport of energy (Salazar 2006). The thermal wave approach is none the less useful for the description of many experimental situations and will be used extensively in this work.

Properties of thermal waves

We may interpret the thermal wave as an alternating heat flux that is related to an oscillating temperature field. In the previous section of this chapter the thermal resistance for stationary heat conduction was defined (see equation 1.16), by once again following the electrical analogy, the concept of thermal impedance can be introduced.

Phase Velocity

The thermal wave will propagate with a phase velocity v_f given by:

$$v_f = \omega\mu = \sqrt{2\alpha\omega} \tag{1.29}$$

Group velocity

Equation 1.25 is a linear ordinary differential equation, therefore the superposition of solutions will also be a solution. This would represent a group of thermal waves with angular frequencies in some given interval that diffuse in space as "packages" and will have a group velocity of:

$$v_g = 2v_f \tag{1.30}$$

Thermal impedance

The thermal impedance is the ratio between the change in the thermal wave amplitude and the thermal wave flux. In the case of a semi-infinite medium:

$$Z_t = \frac{T(x=0,t) - T_{amb}}{-k\left.\frac{\partial T(x,t)}{\partial x}\right|_{x=0}} \tag{1.31}$$

By substituting equation 1.27 into equation 1.31 and for simplicity setting $T_{amb} = 0$ and after a straightforward calculation one obtains:

$$Z_t = \frac{1-i}{\epsilon\sqrt{\omega}} = \frac{1}{\epsilon\sqrt{\omega}} e^{-i\frac{\pi}{4}} \tag{1.32}$$

Notice that while in steady-state conduction the thermal conductivity is the major parameter for the thermal resistance we can observe from equation 1.32 that for oscillating phenomena the parameter of importance is the thermal effusivity.

Using equation 1.32 we may write equation 1.27 as follows:

$$T(x,t) = \frac{I_0}{2} Z_t e^{-\frac{x}{\mu}} \cos\left(\frac{x}{\mu} + \omega t\right) \tag{1.33}$$

Highly dampened wave

The thermal diffusion length, μ, is the distance at which the amplitude will be reduced e times from its initial value at $x = 0$. Equation 1.27 represents a highly-dampened wave, whose wave length is $2\pi\mu$ and which suffers a phase shift with the distance as seen in the complex exponential.

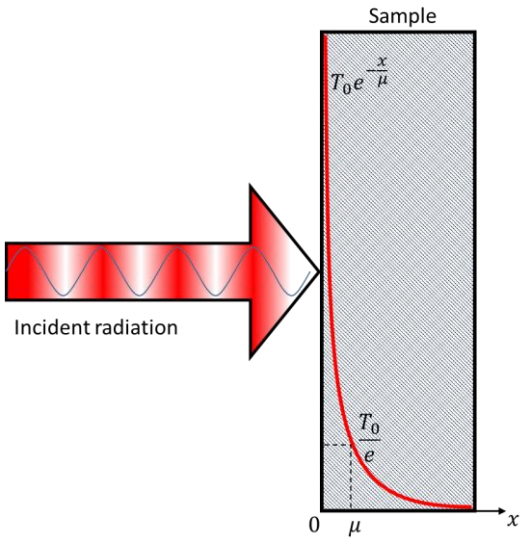

FIGURE 1-5. THERMAL WAVE AMPLITUDE INSIDE AN OPAQUE SAMPLE. μ DENOTES THE THERMAL DIFFUSION LENGTH.

The previous expression allows us to better visualize the dampened nature of the thermal wave and the relation that this dampening holds with the thermal diffusion length, as mentioned in the previous section. Given that the thermal wave length is $\lambda = 2\pi\mu$ it can easily be shown that by this distance the thermal wave will have been practically fully dampened with over 99% of its initial amplitude having faded.

Phase lag

Thermal waves exhibit a phase lag, $\Delta\phi$, between the thermal response of the system and the source of excitation. In the idealized unidimensional heat conduction example seen before:

$$\Delta\phi = \frac{x}{\mu} + \frac{\pi}{4} \tag{1.34}$$

In layman's terms, the phase lag may be viewed as a delay in the arrival of the heat produced by the materials opposition to the change in heat flow. A thermal insulator, which strongly opposes the heat flow, will induce a larger phase then a good conductor. This phase lag comes into play in many experimental schemes.

Reflection and transmission

Thermal waves can be transmitted and reflected in a similar fashion as electromagnetic waves (Almond and Patel 1996). Consider two semi-infinite regions and a thermal plane wave normal to the surface and incident from region 1 that is partially reflected and transmitted at the interface.

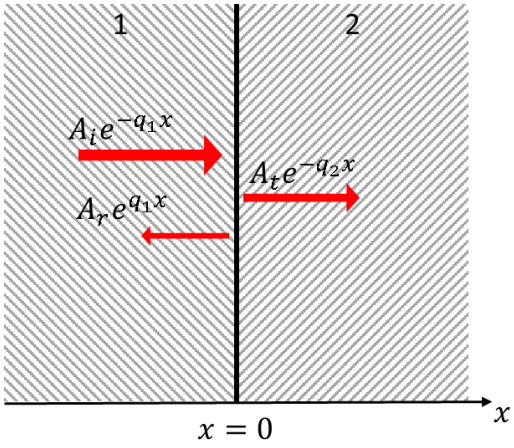

FIGURE 1-6. REFLECTION OF A THERMAL WAVE

The temperature field can be described by:

$$T(x,t) = \begin{cases} A_i e^{-q_1 x} + A_r e^{q_1 x} & x < 0 \\ A_t e^{-q_2 x} & x > 0 \end{cases}$$
$$A_k = \frac{I_0}{2\epsilon\sqrt{\omega}} e^{i\left(\omega t - \frac{\pi}{4}\right)}, k = i, r, t \tag{1.35}$$

Where sub-indexes i, r and t respectively stand for incident, reflected and transmitted thermal waves. Assume as well that the thermal resistance at the interface can be neglected so that:

$$T_1|_{x=0} = T_2|_{x=0} \;\therefore\; A_i + A_r = A_t \tag{1.36}$$

and, due to the heat flux continuity at the interface:

$$A_i - A_r = \left(\frac{k_2 q_2}{k_1 q_1}\right) A_t \tag{1.37}$$

Considering the two previous expressions it can be shown that:

$$A_t = \frac{2A_i}{1 + \frac{k_2 q_2}{k_1 q_1}} \tag{1.38}$$

$$A_r = A_i \frac{1 - \frac{k_2 q_2}{k_1 q_1}}{1 + \frac{k_2 q_2}{k_1 q_1}} \tag{1.39}$$

Equations 1.38 and 1.39 allow for the derivation of the reflection, $R_{1\to2}$, and transmission, $T_{1\to2}$, coefficients:

$$R_{1\to2} = \frac{A_r}{A_i} = \frac{b_{1\to2} - 1}{b_{1\to2} + 1} \tag{1.40}$$

$$T_{1\to 2} = \frac{A_t}{A_i} = \frac{2b_{1\to 2}}{1 + b_{1\to 2}} \tag{1.41}$$

with

$$b_{1\to 2} = \frac{\epsilon_1}{\epsilon_2} \tag{1.42}$$

Applications of thermal waves in material characterization

Many different physical parameters come into play in heat diffusion phenomena. We may then utilize these phenomena to study these quantities. For example, knowing the thermal response of a sample being heated using monochromatic light and varying the light's wavelength would allow us to do absorption spectroscopy. Although in the previous section only semi-infinite samples and uniform lighting schemes have been analyzed, the spatial and temporal distribution of heat depend strongly on geometrical parameters, e.g. impinging beam dimensions and distribution or the sample dimensions and boundaries. Also in thermal diffusion experimentation, the temperature distribution $T(r,t)$ will also be a function of the parameters that account for the diffusion and delocalization of heat-generating centers within the bulk of the sample, e.g. diffusivity, effusivity, carrier diffusion, etc.) (Fournier and Boccara 1988).

Thermal Characterization

Many different variants of photothermal experimentation allow for the thermal characterization of materials. The following subsection provide a brief overview of some of the methods use. Not all the schemes discussed below are directly relevant to this work, however the phenomenological concepts introduced in each of them have been deemed noteworthy.

The Slope Method

In 1861, Swedish scientist A.J. Ångström proposed a method to measure the thermal diffusivity of a solid rod. In Ångström's method a rod is heated at one end by an intensity modulated heat source. The phase lag and amplitude of the thermal wave generated on the rod is studied at two different points.

What Ångström was proposing was a variation of what now is known by many as the slope method. The slope method allows us to obtain the thermal diffusivity from the phase lag, ϕ, or from the amplitude's, A, attenuation and the distance to the heat source, r. Under certain conditions, a linear relation will appear for $\phi\ vs\ r$, and in the case of the amplitude depending on weather we have heat diffusion in (Salazar, Mendioroz et al. 2009):

- 1-D: $Ln(T)\ vs. r$ (e.g. plane wave, flat illumination or thin filament with a point heat source).
- 2-D: $Ln(r^{0.5}T)\ vs. r$ (e.g., cylindrical wave, thin slab with a point heat source).

- 3-D: $Ln(rT)\ vs.\ r$ (e.g. spherical wave, bulk sample with a point heat source).

The simplest case to analyze is, naturally, the 1-D lossless case (developed in previous sections), where the sample's interaction with the environment through conduction, convection or radiation can be discarded.

We know that the phase of plane thermal wave under loss-free conditions is given by equation 1.34 which may be rewritten as follows:

$$\Delta\phi = -\sqrt{\frac{\omega}{2\alpha}}x + \frac{\pi}{4} \tag{1.43}$$

It is easy to see how one may extract the thermal diffusivity α from the slope $\left(m = \left({}^{\omega}/_{2\alpha}\right)^{0.5}\right)$.

Equation 1.27 has an amplitude equal to:

$$\mathrm{A} = \frac{I_0}{2\epsilon\sqrt{\omega}}e^{-\frac{x}{\mu}} \tag{1.44}$$

By taking the natural logarithm of the expression we have:

$$\ln(\mathrm{A}) = \ln\left(\frac{I_0}{2\epsilon\sqrt{\omega}}\right) - \sqrt{\frac{\omega}{2\alpha}}x \tag{1.45}$$

Note that the slope is the same as with the phase, allowing us to get the thermal diffusivity just as easily.

It can be shown that the relations stated above hold for 1-D, 2-D and 3-D lossless heat transfer cases. When losses come into play certain considerations must be considered. Later chapters on this work deal with the determination of the thermal diffusivity taking this into account.

Thermal wave interferometer

Consider the propagation of a plane thermal wave (see equation 1.27) through a sample of thickness L. Suppose that the wave is generated at $x = 0$. The wave, upon arriving at the boundary 2 ($x = L$) will reflect and interfere. The reflected wave will then travel back to boundary 1 ($x = 0$) and be reflected once again, with the process repeating indefinitely. The temperature at the surface L is obtained by summing all the wave trains arriving at this point by means of the superposition principle (Bennett and Patty 1982).

$$\begin{gathered} T(L) = T_1 + T_2 + \cdots + T_n \\ = T_0\left(e^{-qL} + R_1R_2e^{-3qL} + \cdots + (R_1R_2)^n e^{-(2n+1)}\right) \\ = T_0e^{-qL}\sum_{n=0}^{\infty} r^n \end{gathered} \tag{1.46}$$

Where $T_0 = \frac{I_0}{2(\epsilon_g\sqrt{\omega})}$ is the temperature at $x = 0$, $r = R_1R_2e^{-2qL}$ and R_1 and R_2 are, respectively, the reflection coefficients at boundaries 1 and 2. $\sum_{n=0}^{\infty} r^n$ is a geometric series which converges to $\frac{1}{1-r}$ for $|r| < 1$ (as is commonly the case)so that equation 1.46 becomes:

$$T(L) = \frac{T_0 e^{-qL}}{1 - R_1R_2e^{-2qL}} \tag{1.47}$$

A thermally thin sample will be that for which:

$$qL \ll 1 \therefore L \ll \mu \tag{1.48}$$

For a thermally thick sample we have:

$$qL \gg 1 \therefore L \gg \mu \tag{1.49}$$

The limiting frequency between thermally thick and thin is that for which $\mu = L$:

$$f_c = \frac{\alpha}{\pi L} \tag{1.50}$$

The phase lag will be given by:

$$\phi = -\sqrt{\frac{\pi f}{\alpha}}L \tag{1.51}$$

For a thermally thick sample equation 1.47's amplitude reduces to:

$$A = T_0 e^{\sqrt{\frac{\pi f}{\alpha}}L} \tag{1.52}$$

Two experimental variants arise from the relations above. If the experimenter can change the sample thickness (think of a fluid in a container with sliding walls) then a linear relation will arise between the $\ln(A)\ vs.\ L$ and $\phi\ vs.\ L$ and the thermal diffusivity can be straightforwardly calculated from their slopes if the modulation frequency is well known.

If the sample thickness cannot be changed but the modulation frequency can then the thermal diffusivity can be calculated from the slopes between $\ln\left(A\sqrt{f}\right)\ vs.\sqrt{f}$ and $\phi\ vs.\sqrt{f}$.

Non-destructive testing, defect detection and Microscopy

Thermal waves have found multiple applications in the field of non-destructive testing (NDT). It is easy to visualize how a discontinuity in heat-flow, say a crack in a material, would interfere with the flow of heat and allow for its detection, but NDT through thermal wave experimentation also allow for the detection of sub-superficial structures and defects in samples. A way to visualize how this is possible by considering the thermal wave interferometer, previously explained. While a defect is by no means expected to behave as a

perfect, flat, boundary it will reflect incoming thermal waves, with different angles and intensities. The reflected waves will interfere and a thermal contrast is generated allowing the experimenter to visualize or detect features of the sample that lie well beneath the surface. Moreover, the penetration depth of the thermal wave can be controlled by adjusting the modulation frequency, this allows for a detailed scanning at different depths within a sample.

Not only are qualitative images possible, the sizing of defects has been demonstrated in different experimental configurations (Salazar, Mendioroz et al. 2010, Celorrio, Omella et al. 2014, Pech-May, Oleaga et al. 2014). In a forthcoming chapter in this work a NDT technique is explained in detail and experimental results are presented.

By doing a raster scan of a sample with a point source like heating element, e.g. a tightly focused laser spot, photothermal or thermal wave microscopy becomes possible. Thermal waves being generated on the sample´s surface will respond to optical and thermal contrast. Registering the amplitude and phase of the thermal wave generated at each point of the raster scan will give the experimenter a phase and amplitude image, with the amplitude image being highly susceptible to optical and thermal contrast effects and the phase image being more sensitive to thermal parameter variation in the sample.

Photothermal microscopy is worth mentioning as it has recently shown great promise in different applications and has entered the realm of super-resolution microscopy techniques(Nedosekin, Galanzha et al. 2014).

3. Time resolved heat diffusion and transient thermal phenomena

Modulated heat diffusion is not the only regime in which heat diffusion can be studied, the heat diffusion equation can be solved for transient or pulsed heating as well. In this type of setting a brief heat pulse is used and the heating and/or cooling processes are monitored. A pulsed heat source will produce heating in a very short-time, with a Dirac delta heating being the ideal case. A transient heat source requires more time to deposit the thermal energy.

Time resolved techniques tend to be noisier than oscillatory experiments but they are much faster. This speed has led to an increased interest for industrial applications. Thermal characterization and NDT for superficial defects are two important applications of time resolved techniques.

Transient thermal phenomena can be analyzed through the thermal wave approach. Formally the thermal wave solution is frequency domain solution whilst a transient solution will be a time-domain solution, both are related by a Laplace inversion. A time-domain response $T(t)$ may be obtained from a frequency-domain response by means of a Fourier series expansion (Almond and Patel 1996):

$$T(x,t) = \sum_n a(\omega_n) T(x,\omega_n,t) \tag{1.53}$$

where the component $T(x,\omega_n,t)$ is a planar thermal wave with ω_n as its angular frequency and $a(\omega_n)$ is a measure of the strength of this component.

Given a continuous spectrum of thermal wave modulation frequencies this expansion can be expressed as an integral transform. The resulting integrals can often be solved with ease in the complex plane by means of the Laplace inverse transform method. These transforms provide a simple route for obtaining the transient solutions of problems that have already been analyzed in the frequency domain.

One of the most well-known time resolved techniques is the flash technique for the measurement of thermal diffusivity. Proposed in 1961 by Parker et al, this simple and versatile technique can be applied to a wide range of experimental conditions. The basic principles of the flash technique as an exemplification of time resolved photothermal techniques is presented up next. For this simple case in which one dimensional heat diffusion is assumed and losses are ignored, the time domain analysis is shown.

The flash technique

Consider a thermally insulated solid of density ρ (kg/m^3), heat capacity C (J/kgK) and of uniform thickness L. The solid's surface is heated uniformly by an instantaneous pulse of radiant energy Q (J/m^2) that is absorbed at a small depth,ξ, so that (Parker, Jenkins et al. 1961):

$$T(x,0) = \begin{cases} \dfrac{Q}{\rho C \xi} & for\ 0 < x < g \\ 0 & for\ g < x < L \end{cases} \tag{1.54}$$

The temperature distribution for $t > 0$ is given by (Carslaw and Jaeger 1959):

$$T(x,t) = \frac{1}{L}\int_0^L T(x,0)dx + \frac{2}{L}\sum_{n=1}^{\infty} e^{-\frac{n^2\pi^2\alpha t}{L^2}} \times \cos\frac{n\pi x}{L}\int_0^L T(x,0)\cos\frac{n\pi x}{L}\,dx \tag{1.55}$$

If we consider total superficial absorption, i.e. $\xi \approx 0$ and the boundary condition set in equation 1.54, the back-surface temperature can be written as:

$$T(L,t) = \frac{Q}{\rho C L}\left[1 + 2\sum_{n=1}^{\infty} -1^n e^{-\frac{n^2\pi^2}{L^2}\alpha t}\right] \tag{1.56}$$

Based on the previous equation two ways of obtaining the thermal diffusivity are proposed in Parker's original paper:

$$\alpha = 1.38\frac{L^2}{\pi^2 t_{1/2}} \tag{1.57}$$

$$\alpha = \frac{0.48L^2}{\pi^2 t_x} \tag{1.58}$$

$t_{1/2}$ is the time at which the temperature rise is half that of the maximum, T_M. Equation 1.56 show a linear behavior for short times, if the linear behavior is extrapolated so that it intersects the time axis then t_x is the value of that intersect (see Figure 1-7).

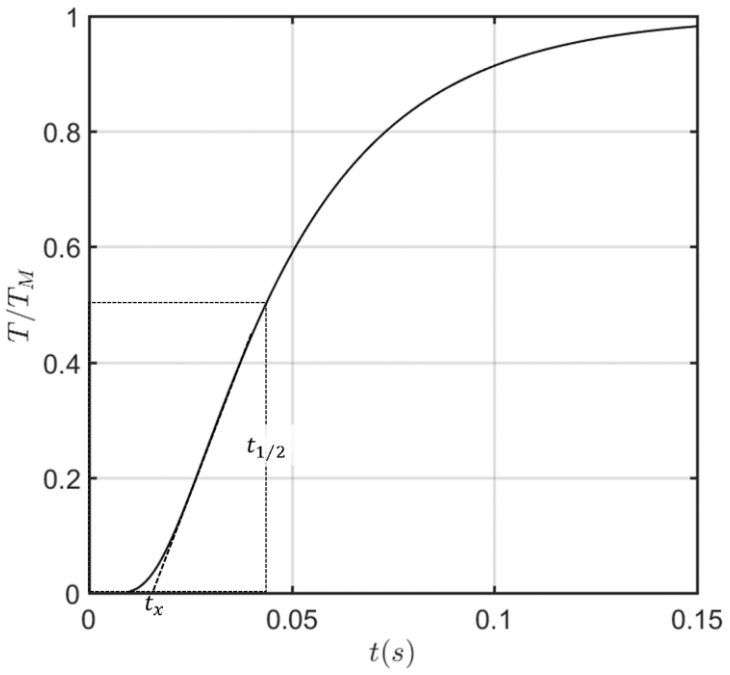

FIGURE 1-7. NORMALIZED NUMERICAL SIMULATION FOR EQUATION 1.56 FOR THE FOLLOWING PARAMETERS: $\alpha = 1\times10^{-5}, L = 1\times10^{-3}$. $t_{1/2}$ AND t_x ARE SHOWN.

The determination of the thermal diffusivity does not require the knowledge of the absorbed energy but this quantity is needed if the specific heat or thermal conductivity are required:

$$\rho C = \frac{Q}{LT_M} \tag{1.59}$$

One of the reasons the flash technique has become the gold standard for thermal diffusivity measurement is that equations 1.57, 1.58 and 1.59 are very simple expressions and can all be obtained from a single measurement in a relatively simple set-up (Vozár and Hohenauer 2004). The flash method will be covered to a greater depth in an upcoming chapter where front face detection is used.

4. Some thermal wave generation and detection schemes

Many different experimental schemes to study and generate thermal waves have been developed throughout the years. This subsection explores schemes thought notable for this work in a phenomenological fashion, references are presented in case the reader wishes further insight.

Thermal wave generation

To generate thermal waves one must provide a modulated heat source. One of the most common ways to generate them is through the photothermal effect. In fact, the study of

thermal waves and the PT effect is knitted very closely. The ability to modulate light's intensity, e.g. by mechanically chopping it, allows us to probe into different theoretical thermal wave frameworks, opening a broad range of experimental techniques.

Furthermore, advances in the previous century gave scientists the laser; a powerful highly monochromatic and spatially coherent light source. While monochromatic light could be generated before the laser, e.g. by means of a monochromator (still widely used in spectroscopy), laser beams have given experimentalists the ability to shape light from a tight diffraction limited spot to the simultaneous uniform lighting of a complete surface, paving the way for even more applications.

The photothermal effect

The process by which light is turned into heat is known as the photothermal (PT) effect. There are different pathways or processes for heat generation through light. When a beam of light impinges on the surface of an absorbing sample the heating will be a function of many different physical parameters and effects (Fournier and Boccara 1988), e.g. the absorption coefficient β of the media, the reflectance R, phosphorescence, fluorescence, photovoltaic effect, electron-hole pairs in semiconductors, etc. However, independently of the different possible heat generation pathways a heating quantum efficiency, η, can be defined as a ratio of the heat produced and the incident optical energy.

Considering a sample of thickness dx and at a depth x the amount of heat generated per unit of volume will be:

$$dQ = -\eta(1-R)\left(\frac{dI}{dx}\right)dx \tag{1.60}$$

If the absorption is superficial then:

$$dQ = \eta(1-R)\beta I_0 dx \tag{1.61}$$

Generating heat sources using light is attractive due to a variety of reasons. An important one is that there is no need to touch the sample under study, i.e. non-contact, this means that the sample will remain unaltered since the heat will be generated within itself.

Light source modulation

Some light modulating techniques relevant to this work are listed and briefly described next:

- *The optical chopper*

  An optical chopper is a device designed to periodically interrupt a light beam. Different chopping systems have been devised, e.g. the rotating mechanical chopper consists of a rotating light blocking disk with holes spread periodically at a constant radial distance. By rotating the disk and

positioning the light beam with the radial distance light may be modulated. The rotation speed controls the modulation frequency. Choppers operating with mechanical shutters or even tuning forks also exist.

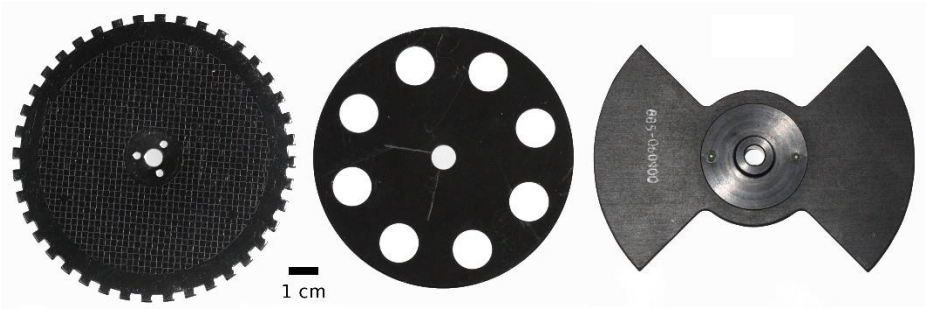

FIGURE 1-8. ASSORTMENT OF MECHANICAL CHOPPER DISKS. (WIKIPEDIA 2016)

- *Acusto-optic modulator (AOM)*

  An AOM utilizes the acusto-optic effect to diffract light using ultrasound. Essentially, the device consists of an acusto-optic material, usually quartz or glass, and an ultrasonic transducer. This device allows the user to control the deflection of the diffracted beams and their intensity, among other parameters.

  An AOM is also known as a Bragg cell, given that the light diffraction is most generally referred to as Bragg diffraction in analogy to the selective X-ray diffraction by the lattice planes of crystals first described by W.H. Bragg in 1913, but the actual phenomenon is known as Brillouin scattering. Further details into the acusto-optic effect and Brillouin scattering can be found elsewhere (Tsai 1990).

- *Electronic modulation and on off switching*

  The output power of electrical light sources depends on the current being fed to said source. Modulation of the current makes modulation of the light intensity possible. However, the electrical response of the system must be considered to have good control over the modulation parameters.

  With the invention of the light emitting diode (LED) and the diode laser electronic switching of light sources has become a common day occurrence. The fast response of these devices basically makes electronic switching an on/off modulation. An important advantage of this type of modulation is the flexibility in frequencies it offers. While a mechanical

chopper usually has a very limited frequency range, it is not uncommon for an electronically switched laser to operate anywhere from continuous wave (CW) operation up to the kilohertz range or more.

Other light modulation techniques include: electro-optic modulators, liquid crystal variable dimmers, electronically actuated mirrors and spatial light modulators among others.

Other heat source generation methods

Not only light can be used to generate the controlled heat source required for the study of thermal diffusion. Other methods are listed below:

- Joule effect
- Magnetocaloric effect
- Thermoelectric effect
- Inductive heating
- Ultrasonic excitation

Of these other methods, only ultrasonic excitation pertains directly to this work. In a forthcoming chapter the theory and results for a NDT experiment utilizing ultrasonic excitation will be presented.

Thermal wave detection

How are thermal waves detected so they can be studied? It might seem obvious, a thermometer placed on the sample would allow the experimenter to examine the temperature fluctuations due to thermal waves, this works for some situations but not for all. Under many experimental configurations sampling the temperature directly becomes a complicated task, e.g. a physical thermometer might block out the incident light used for thermal wave generation. Many physical parameters are related to temperature. We can use the variations induced in these parameters to indirectly measure thermal waves.

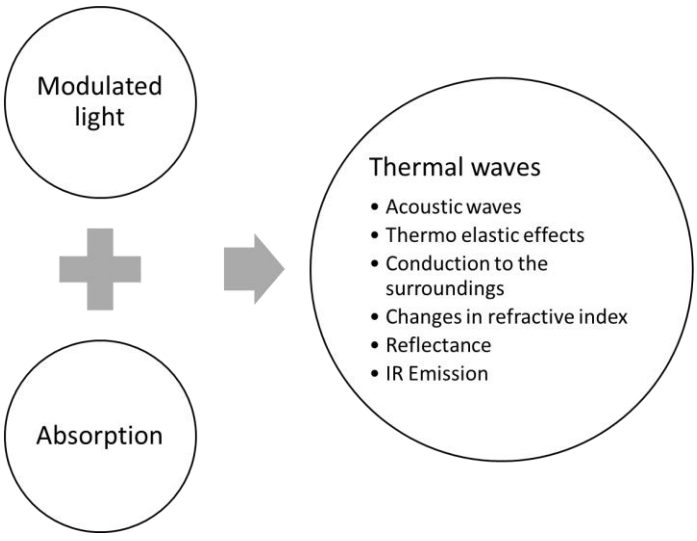

FIGURE 1-9. SOME OF THE EFFECT INDUCED BY THERMAL WAVES

This allows to classify detection methods in two broad categories. Direct methods are those that offer a signal that is directly generated by temperature oscillations and indirect methods are those whose signal generation relies on other temperature dependent phenomena, e.g. refractive index fluctuations. Below some direct and indirect methods are listed and briefly described.

Infrared Techniques

In previous sections the concept of IR thermal radiation was introduced as a form of heat transfer. It may also be used as a means of measuring the temperature of an object. The following techniques are based on this concept.

Photothermal Radiometry

Photothermal Radiometry or PTR is a detection technique that registers the time-varying part of the sample surface temperature induced by the absorption of a modulated light beam by means of an infrared (IR) detector. (Nordal and Kanstad 1979)

By collecting the infrared light emitted by an IR optically opaque sample surface and focusing it onto a detector the temperature of said surface can be obtained.

The detector is made from a specialized IR sensitive material, e.g. mercury cadmium telluride, which generates a voltage or current signal in proportion to the power of the incident radiation. Many detectors require extreme cooling, some by liquid nitrogen immersion, to mitigate the noise effects brought on by their own IR emission.

A great advantage of this noncontact technique is that no cell is needed and vacuum operation is possible. Also, the sensitivity of this technique increases as the third power of the temperature, so the method is well suited for high temperature measurements.(Fournier and Boccara 1988)

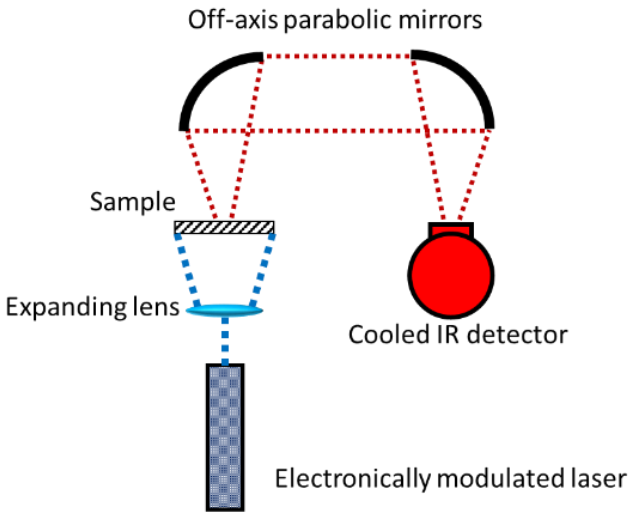

FIGURE 1-10. PTR EXPERIMENTAL SET-UP AS SEEN IN CICATA-LEGARIA

Infrared thermography

Infrared thermography (IRT) or thermal imaging is a technique that holds many similarities with PTR. Both techniques use the same phenomenon of IR emission to study the temperature of a body. IRT takes it one step further, instead of a single, large area detector, an array of small detectors is used along with image formation optics. The resulting image, known as a thermogram, is a map of the spatial temperature distribution on a given sample at a given time.

IRT camera detector arrays are usually constructed with IR sensitive materials, as with PTR. Thermal detectors, namely microbolometers are also used for the construction of cheaper, albeit less sensitive cameras (Maldague 2012).

IRT has found many applications in science and engineering including thermophysical property investigation and non-destructive testing. IRT is an important area of interest for this dissertation and will be explored to a greater depth in a forthcoming chapter.

Thermo-refractive methods

The refractive index holds a relation to temperature, therefore, changes in the refractive index of a substance can be used to probe its temperature. The following techniques exploit this dependence to indirectly quantify the temperature of a sample.

Thermal lens

Reported and described in 1965 by a team working at Bell Labs as a laser defocusing phenomena (Gordon, Leite et al. 1965) it didn't take long for its capabilities as a material characterization technique were exploited (Long, Swofford et al. 1976). When a laser beam (or other source of concentrated light) is passed through a semi-transparent medium part of this light gets turned into heat. This heating directly affects the refractive index of the medium forming a temperature dependent gradient which acts as a lens. The coefficient of refractive index with temperature, dn/dT, varies for different materials but is normally negative for gases and liquids and positive in solids. This means that gases and liquids will usually form a diverging lens while solids will form a convergent lens.

Thermal lens experiments have since evolved into "pump-probe" configuration, where a pump beam is used to excite the sample while a probe beam, with much lower power, is used to examine the induced lens. This technique is highly sensitive to the absorption characteristics of the medium and has been used with great success in spectroscopy. (Snook and Lowe 1995, Marcano O, Loper et al. 2001, Cabrera, Marcano et al. 2006)

Mirage effect

In general terms, a mirage is an optical phenomenon where light is refracted to produce a displacement, or in some cases a reflection, of an image of a distant object. Most people are familiar with mirages encountered when travelling on an open highway on a sunny day. The asphalt at a distance appears to turn into water, in fact what is seen there is a reflection of the sky above.

FIGURE 1-11. A MIRAGE ON A ROAD, COMMONLY CALLED "FAKE WATER". (INAGLORY 2007)

A mirage is created when a hot object transfers heat into a surrounding fluid this induces a refractive index gradient and causes the optical effect. Boccara, Fournier and Badoz showed in their 1980 publication that the deflection of a laser beam could be advantageously used for monitoring the temperature gradient field close to a sample surface (Boccara, Fournier et al. 1980). The idea is simple, we may study the temperature distribution of an object by analyzing the mirage it generates. The mirage effect will be explored to a further extent in a following chapter.

Signal processing in thermal wave experiments

Thermal wave experimentation poses some interesting signal processing challenges. PT techniques usually assume a small temperature increase which in turn convey a small signal whose amplitude and phase must be determined with good precision. A processing technique that allows this even in noisy environments is Lock-in Amplification (LIA). This technique is of interest for this work as it has been used in several of the experimental schemes in the upcoming chapters, the following section will provide a concise explanation of the technique.

Lock-in Amplification

LIA allows the recovery of amplitude modulated signals on a known carrier frequency, f, in an environment where the signal to noise ratio (SNR) is very low. A simple way of visualizing a LIA's operating principle is shown below and is through trigonometric identities (Marín and Ivanov 2009) . The following image shows a basic block diagram for LIA

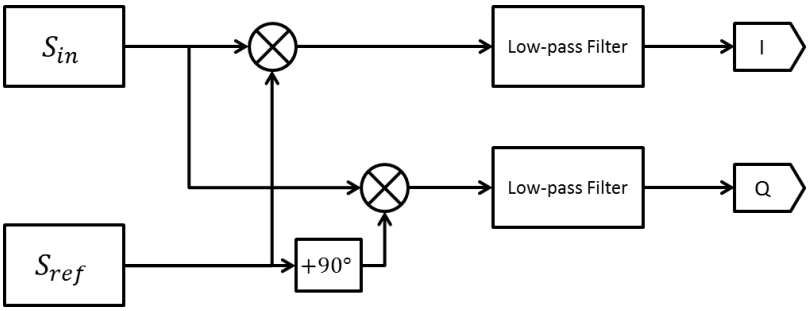

FIGURE 1-12. LIA BLOCK DIAGRAM

Assume that the carrier wave, $S_{ref}(t)$, is a sinusoid of frequency, f, and unit amplitude:

$$S_{ref}(t) = sin(2\pi ft) \tag{1.62}$$

In experiments involving LIA, $S_{ref}(t)$ should be synchronized to the signal driving the excitation element, e.g. a laser. The signal resulting from the experiment will be an amplitude modulated phase shifted signal and incoherent random noise, $G(t)$, whose frequency is, for the most part, different from that of the reference.

$$S_{in}(t) = Asin(2\pi ft + \phi) + G(t) \tag{1.63}$$

Next, the input signal is multiplied by the reference signal and a signal in quadrature, i.e. shifted by 90°, $S_{ref'}$.

$$P_I(t) = S_{in}(t) \times S_{ref}(t) \tag{1.64}$$

$$P_Q(t) = S_{in}(t) \times S_{ref'}(t) \tag{1.65}$$

Using the following trigonometric equations:

$$2\sin(a)\sin(b) = \cos(a-b) - \cos(a+b) \tag{1.66}$$

$$2\cos(a)\sin(b) = \sin(a+b) - \sin(a-b) \tag{1.67}$$

the multiplication can be rewritten as:

$$P_I(t) = \frac{1}{2}(Acos(\phi) - Acos(4\pi f + \phi))f + S_{ref}(t)G(t) \tag{1.68}$$

$$P_Q(t) = \frac{1}{2}\big(Asin(\phi) + Asin(4\pi f + \phi)\big) + S_{ref'}(t)G(t) \tag{1.69}$$

Note that in the previous equations all terms are oscillatory except for the first term in each of the equations, which are only generated when two components of equal frequency are multiplied. This means that these two values will behave as a signal offset so that the temporal average of P_I and P_Q will be:

$$I = \frac{A}{2}cos(\phi) \tag{1.70}$$

$$Q = \frac{A}{2}sin(\phi) \tag{1.71}$$

I and Q can be obtained by low-pass filtering signals P_I and P_Q. Notice that any harmonic response from the experiment would effectively be handled as noise in LIA. These two relations can be considered a simple two equation system with two unknown variables. Solving for A and ϕ we have:

$$\phi = tan^{-1}\left(\frac{Q}{I}\right) \tag{1.72}$$

$$A = \frac{1}{2}\sqrt{I^2 + Q^2} \tag{1.73}$$

Depending on the modulation frequency, a LIA measurement can be a lengthy procedure. To determine the offset values I and Q with good precision a sufficient number of cycles must be used. Note that in the case of frequency resolved measurements, e.g. those seen in thermal wave interferometer, the total experiment time can become quite extensive.

5. References

Almond, D. P. and P. M. Patel (1996). Photothermal Science and Techniques, Springer Netherlands.

Bennett, C. and R. Patty (1982). "Thermal wave interferometry: a potential application of the photoacoustic effect." Applied Optics **21**(1): 49-54.

Bergman, T. L. and F. P. Incropera (2011). Introduction to heat transfer, John Wiley & Sons.

Boccara, A., et al. (1980). "Thermo-optical spectroscopy: Detection by the''mirage effect''." Applied Physics Letters **36**(2): 130-132.

Cabrera, H., et al. (2006). "Absorption coefficient of nearly transparent liquids measured using thermal lens spectrometry." Condens. Matter Phys. **9**(2): 385-389.

Carslaw, H. S. and J. C. Jaeger (1959). Conduction of heat in solids, Clarendon Press.

Celorrio, R., et al. (2014). "Vertical cracks characterization using lock-in thermography: II finite cracks." Measurement Science and Technology **25**(11): 115602.

Çengel, Y. A. (2008). Introduction to Thermodynamics and Heat Transfer, Ed. 2, 2008, Mc Graw-Hill.

Fourier, J. (2009). The analytical theory of heat, Cambridge University Press.

Fournier, D. and A. Boccara (1988). Photothermal investigation of solids: basic physical principles. Photoacoustic Investigations of Solids and Fluids. J. A. Sell. San Diego, CA, Academic Press**:** 35-79.

Gordon, J., et al. (1965). "Long-transient effects in lasers with inserted liquid samples." Journal of Applied Physics **36**(1): 3-8.

Inaglory, B. (2007). "Hot Road Mirage." Retrieved 10 March, 2017, from https://commons.wikimedia.org/wiki/File:Hot_road_mirage.jpg.

Long, M., et al. (1976). "Thermal lens technique: a new method of absorption spectroscopy." Science **191**(4223): 183-185.

Maldague, X. P. (2012). Nondestructive evaluation of materials by infrared thermography, Springer Science & Business Media.

Marcano O, A., et al. (2001). "High-sensitivity absorption measurement in water and glass samples using a mode-mismatched pump-probe thermal lens method." Applied Physics Letters **78**(22): 3415-3417.

Marín, E. (2009). "Linear relationships in heat transfer." Latin-American Journal of Physics Education **3**(2): 9.

Marín, E. (2009). "Thermal wave physics: principles and applications to the characterization on liquids." RECEN-Revista Ciências Exatas e Naturais **6**(2): 145-169.

Marín, E., et al. (2009). "Similarity theory and dimensionless numbers in heat transfer." European Journal of Physics **30**(3): 439.

Marín, E. and R. Ivanov (2009). "LIA in a Nut Shell: How can Trigonometry help to understand Lock-in Amplifier operation? ." Lat. Am. J. Phys. Educ. **3**(3): 3.

Modest, M. F. (2003). Radiative heat transfer, Academic press.

Nedosekin, D. A., et al. (2014). "Super-Resolution Nonlinear Photothermal Microscopy." Small **10**(1): 135-142.

Nordal, P.-E. and S. O. Kanstad (1979). "Photothermal radiometry." Physica Scripta **20**(5-6): 659.

Parker, W. J., et al. (1961). "Flash Method of Determining Thermal Diffusivity, Heat Capacity, and Thermal Conductivity." J. Appl. Phys. **32**(9): 1679.

Pech-May, N., et al. (2014). "Vertical cracks characterization using lock-in thermography: I infinite cracks." Measurement Science and Technology **25**(11): 115601.

Salazar, A. (2003). "On thermal diffusivity." European Journal of Physics **24**(4): 351.

Salazar, A. (2006). "Energy propagation of thermal waves." European Journal of Physics **27**(6): 1349.

Salazar, A., et al. (2010). Characterization of delaminations by lock-in vibrothermography. Journal of Physics: Conference Series, IOP Publishing.

Salazar, A., et al. (2009). "The strong influence of heat losses on the accurate measurement of thermal diffusivity using lock-in thermography." Applied Physics Letters **95**(12): 121905.

Snook, R. D. and R. D. Lowe (1995). "Thermal lens spectrometry. A review." Analyst **120**(8): 2051-2068.

Tsai, C. S. (1990). Guided-wave acousto-optics: interactions, devices, and applications, Springer Science & Business Media.

Vozár, L. and W. Hohenauer (2004). "Flash method of measuring the thermal diffusivity. A review." High temperatures-High pressures **36**(3): 253-264.

Wikipedia, C. o. (2016, 28 February 2016). "Optical Chopper." Retrieved 9 March, 2017.

2. Mirage effect based methods for material thermal characterization

Chapter 1 gave a brief introduction to thermo-refractive techniques, a family of PT techniques used in thermal characterization and NDT. An important part of this dissertation is based on the mirage effect, a member of this family of techniques. This chapter's first section is intended to further the reader's understanding of the mirage effect, its main advantages and limitations and traditional experimental schemes. The subsequent sections will cover the new contributions made to this PT technique including the use of imaging devices to study the mirage effect.

1. Chapter Objectives

- Exploration and assessment of mirage based linear relation methods for thermal characterization.
- Development of new experimental configurations that optimize measurement time and reduce experimental complexity.

2. Introduction

As previously discussed, PT heating of a sample can generate a refractive-index (RI) gradient in the sample or in a neighboring medium. Two distinct mechanisms can generate the RI variations, viz.: thermal and acoustic. The second is generated due to the propagation of a PA wave which generates pressure dependent density fluctuations in the medium. The thermal RI variation is a direct consequence of the RI temperature dependence.

The thermal RI gradient generally provides a larger signal, but at distances greater than a couple of thermal diffusion lengths only the acoustic RI gradient can be detected given that PA waves attenuate due to the acoustic characteristics of a material. While both can be used to measure similar parameters, e.g. optical absorption coefficient, temperature and flow velocity of a sample, only the thermal RI gradient can be used for the determination of thermal diffusivity (Sell 1989). This makes the thermal RI gradient the object of interest for this thesis and any acoustic contribution will be neglected as all measurements will be taking place close to the sample surface.

Mirage Effect Fundamentals

The idea of mirage effect based methods is to take advantage of the effects of the temperature variations on the propagation of a probe beam. The RI associated with the temperature field can be expanded as a Taylor series around $\vec{r}_0$ as follows:

$$n(\vec{r}_0 - \vec{r}, t) = n(\vec{r}_0, t) + \vec{r}\frac{\partial n}{\partial r}\Big|_{r_0} + \frac{\vec{r}^2}{2}\frac{\partial^2 n}{\partial r^2}\Big|_{r_0} + \cdots \quad (2.1)$$

where

$$n(\vec{r}, t) = \frac{\partial n}{\partial T} T(\vec{r}, t) \quad (2.2)$$

with $T(\vec{r}, t)$ being the temperature rise. The RI perturbation leads to equation 2., where each of the first three terms is associated with three different techniques: interferometry, beam deflection and thermal lensing, respectively (Fournier and Boccara 1988). On the next section interest lies solely on photothermal beam deflection (PBD), i.e. the second term, and its potential for thermal diffusivity determination in solid samples. The final section of this chapter deals with a technique known as photothermal shadowgraph (PS) and is related to the second derivative of the RI.

A common element in mirage effect based techniques is the need to understand the behavior of the temperature field in the media surrounding a sample, the easiest scenario is, arguably, that of a slab.

Consider an optically opaque slab of thickness L and semi-infinite in other directions immersed in a fluid γ. The fluid has been split for analysis in to sections, γ_1 and γ_2.

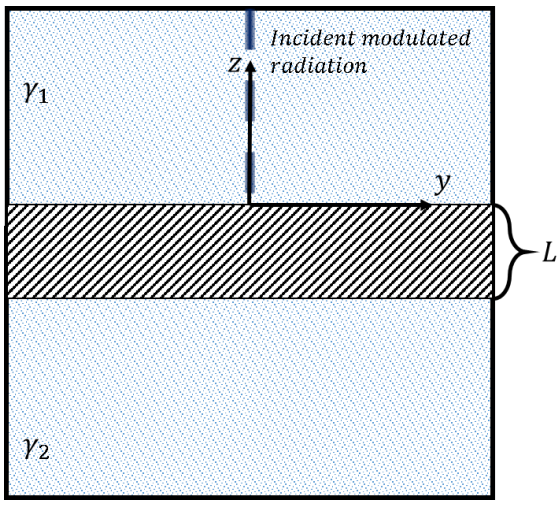

FIGURE 2-1 PROBLEM GEOMETRY.

The slab is heated by a light beam modulated a fixed angular frequency, ω, and is focused onto a tight spot with a Gaussian profile with a defining the beam radius at $1/e^2$ of its intensity. The heat deposited by the beam as a function of time and position $r = \sqrt{x^2 + y^2 + z^2}$ is:

$$Q(\vec{r}, t) = \begin{cases} \frac{P_0}{2\pi a} e^{-\frac{r^2}{a}} e^{i\omega t} & z = 0 \\ 0 & z \neq 0 \end{cases}$$

The heat diffusion equation in each medium can be written as:

$$\nabla^2 T_{\gamma_1} - \frac{1}{\alpha_\gamma}\frac{\partial T_{\gamma_1}}{\partial t} = 0 \tag{2.3}$$

$$\nabla^2 T_{\gamma_2} - \frac{1}{\alpha_\gamma}\frac{\partial T_{\gamma_2}}{\partial t} = 0 \tag{2.4}$$

$$\nabla^2 T_s - \frac{1}{\alpha_s}\frac{\partial T_s}{\partial t} = -\frac{Q(\vec{r},t)}{k_s} \tag{2.5}$$

where α is the thermal diffusivity, k is the thermal conductivity and subindices γ_1, γ_2, s denote the front face fluid, back face fluid and sample respectively. If convective and radiative heat losses can be neglected the following boundary conditions apply:

$$T_{\gamma_1}(z=0) = T_s(z=0) \qquad T_s(z=-L) = T_{\gamma_2}(z=-L) \tag{2.6}$$

$$k_{\gamma_1}\frac{\partial T_{\gamma_1}}{\partial t}\Big|_{z=0} = k_s\frac{\partial T_s}{\partial t}\Big|_{z=0} \qquad k_{\gamma_2}\frac{\partial T_{\gamma_2}}{\partial t}\Big|_{z=-L} = k_s\frac{\partial T_s}{\partial t}\Big|_{z=-L} \tag{2.7}$$

if the thermal conductivity of the sample is much larger than the surrounding medium ($k_s \gg k_\gamma$) It has been shown by others (Salazar, Sanchez-Lavega et al. 1989) that equations 2.3 through 2.5 will have the following solution:

$$T_{\gamma_1} = \frac{1}{2}\frac{P_0}{2\pi k_s}\int_0^\infty \delta J_0(\delta r) e^{-\frac{(\delta a)^2}{8}} \frac{1}{\beta_s}\left(\frac{1+e^{-2\beta_s L}}{1-e^{-2\beta_s L}}\right) e^{-\beta_\gamma z} d\delta \tag{2.8}$$

$$T_{\gamma_2} = \frac{1}{2}\frac{P_0}{2\pi k_s}\int_0^\infty \delta J_0(\delta r) e^{-\frac{(\delta a)^2}{8}} \frac{1}{\beta_s}\left(\frac{1}{e^{\beta_s L}-e^{-\beta_s L}}\right) e^{\beta_\gamma (l+z)} d\delta \tag{2.9}$$

$$T_s = \frac{1}{2}\frac{P_0}{2\pi k_s}\int_0^\infty \delta J_0(\delta r) e^{-\frac{(\delta a)^2}{8}} \frac{1}{\beta_s}\left(\frac{e^{\beta_s z}+e^{-\beta_s z}e^{-2\beta_s l}}{1-e^{-2\beta_s L}}\right) d\delta \tag{2.10}$$

where $\beta_i^2 = \delta^2 + \left({}^{i\omega}/_{k_i}\right)^2$. Equations 2.8 through 2.10 have no analytical solutions, however through numerical simulation and experimentation several linear relations have been confirmed and have been successfully used in determining thermal diffusivity values(Salazar and Sanchez-Lavega 1994). The phase slope method discussed in the first chapter of this work is one of these relations and is of interest for this work.

It is important to note that to be able to obtain a correct value for the thermal diffusivity through the slope method, the experimenter must make sure to probe the RI gradient as close to the sample surface as possible. If the probing takes place too far from the sample surface the phase slope method will incur in an error that may become considerable at greater distances.

For this work, optically opaque solid samples have been chosen in both a filament and slab geometry for the PBD and filament geometry for the PS. The geometry of a filament poses a

greater analytical challenge. Nevertheless, Salazar et al. have analyzed the problem for an infinitely long filament of radius *b* immersed in a fluid, much in the same way as the previously analyzed slab (Salazar, Mendioroz et al. 2010). The filament is heated using linear illumination with a Gaussian distribution over the axis of the filament but uniform distribution perpendicular to the filament. The Gaussian line's $1/e^2$ parameter is given by a.

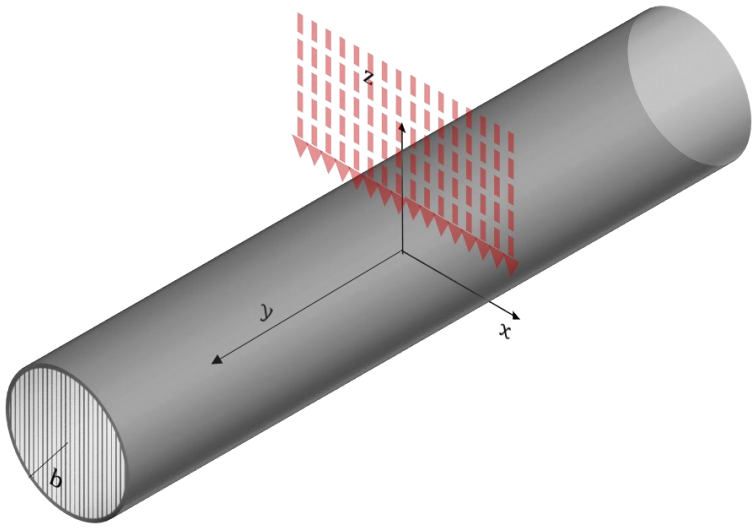

FIGURE 2-2 PROBLEM GEOMETRY FOR A THIN WIRE

The solution to the heat diffusion equation both for the filament and fluid under this geometry results in a highly oscillatory function that is difficult to evaluate numerically. However, when heat losses can be neglected, and the laser spot can be assumed to be tightly focused $a \to 0$, a simple approximation for the surface temperature of the filament can be found:

$$T_s(y) \approx \frac{P_0}{2\pi k_s b\sqrt{\frac{2\pi f}{\alpha_s}}} e^{\sqrt{\frac{\pi f}{\alpha_s}}|y|} e^{i\left(\sqrt{\frac{\pi f}{\alpha_s}}|y|-\frac{\pi}{4}\right)} \tag{2.11}$$

The phase slope method holds for the previous equation. While this is a solution to the filament surface temperature, it is not unreasonable to think that if the fluid's temperature field near the surface of the filament is probed the phase slope method could be used to determine the thermal diffusivity. In fact, *Barkyoumb et al* have demonstrated the use of beam deflection technique to obtain the thermal diffusivity of thin wires and have explored the heat diffusion to the surrounding media further (Barkyoumb and Land 1995).

Traditional detection Schemes

Different experimental schemes have been developed based on the samples being studied and other experimental conditions.

Collinear

Initially proposed in 1980 by *Fournier et al.* for the spectroscopic measurement of highly transparent samples (Fournier, Boccara et al. 1980), the method was extended for thermal characterization by *Salazar et al.*, where it was applied to the thermal characterization of transparent and semi-transparent samples (Salazar, Sánchez-Lavega et al. 1993).

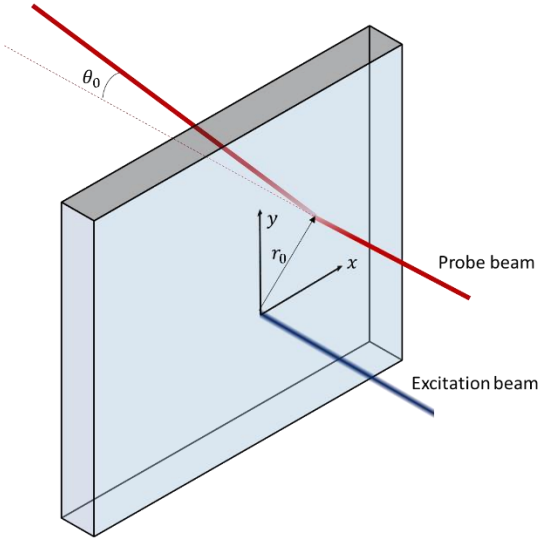

FIGURE 2-3 DEFLECTION OF A BEAM PARALLEL TO THE PUMP BEAM IN A SEMITRANSPARENT MEDIUM

In this variant parallel pump and probe beams are used. The sample must be transparent to the probe beam and absorb, at least partially, the pump beam. The probe beam is passed at a distance r_0 from the pump and its deflection is studied. The beam will be deflected by the RI gradients in the fluid layers on the back and front and by the sample itself. While this variant has demonstrated its usefulness, it is not in the interest of this work to explore it any further since semitransparent samples are outside of its scope. Further information on collinear beam deflection can be found elsewhere.

Bouncing (Surface reflection)

In this scheme, the probe beam bounces on the sample surface close to the zone being heated. The direction of the probe beam is inclined with respect to the sample surface by a small angle ϑ, usually a couple of degrees.

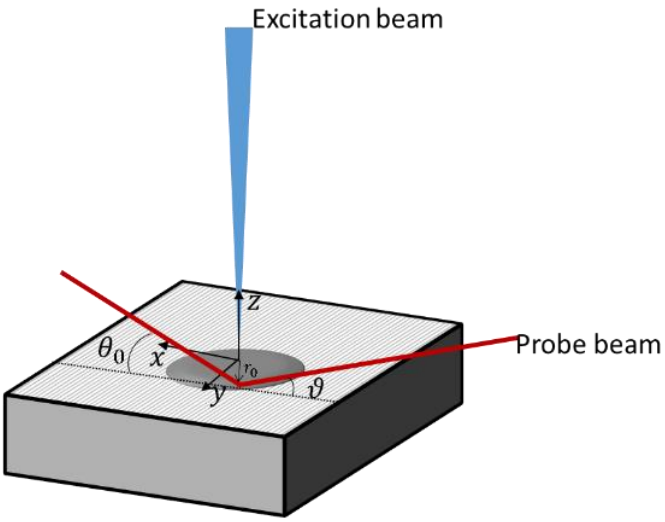

FIGURE 2-4 DEFLECTION OF A BEAM IN THE BOUNCING CONFIGURATION

The technique has the important advantage of always probing close to the surface but one important point of this scheme is that it cannot be applied to samples that do not reflect the probe properly (Bertolotti, Liakhou et al. 1998). For best results samples must have an almost specular reflection, this limits the number of samples and overcomplicates sample preparation. For this reason, this technique has been discarded for this work, while slabs can be polished to have the reflective properties required, this procedure would be impossible for filaments.

Orthogonal skimming

The orthogonal skimming scheme works well for optically opaque samples. The pump beam and probe beam are orthogonal and the probe beam should skim the surface of the sample being measured.

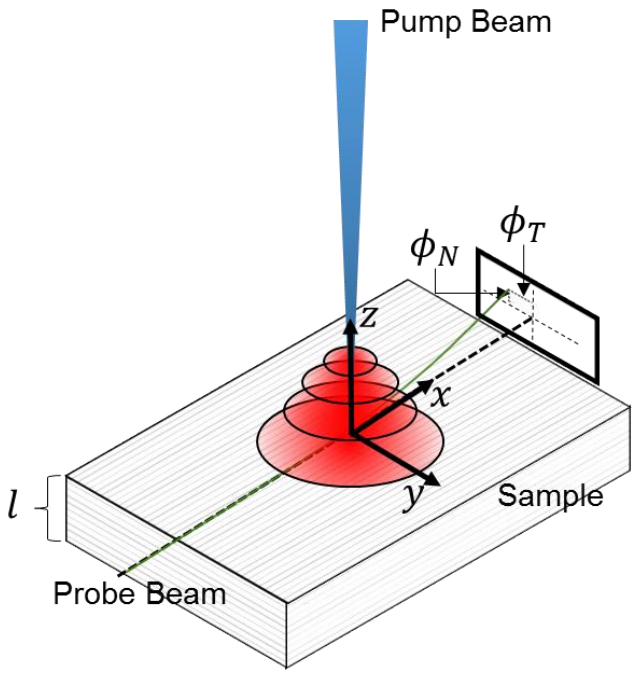

FIGURE 2-5 TYPICAL PHOTOTHERMAL BEAM DEFLECTION SURFACE SKIMMING EXPERIMENTAL CONFIGURATION

The main complications from orthogonal skimming are given by the need to probe the RI gradient as close to the sample as possible. This means that a regular surface that does not block the probe beam is needed as well as careful alignment. There limit to the proximity one may scan the sample will be related to the diameter of the probe beam. We have chosen to test this technique and to develop it further looking to simplify its experimental procedure mainly due to it being the most versatile of the experimental variants; it is compatible with different geometries and can be utilized with opaque samples. The next two sections of this chapter will further explain the developments done.

Advantages and Limitations

The mirage effect offers some advantages over other photothermal methods. It is a non-contact technique that can be done at ambient temperature and pressure. There is no need to introduce any physical probe that might affect the result. The technique may also be carried out in fluids other than air, this can work to the advantage of the experimental sensitivity since a fluid with a higher dn/dT can be utilized to amplify the signal.

In the case of opaque samples, contact with a surrounding fluid is necessary. This imposes some limitations on the method. As the thermal conductivities of the sample and fluid approach each other, the linear relations, e.g. the phase slope method, begin to waver. This imposes a limit on the ability to determine the thermal diffusivity accurately. That being said, it has been shown

by others that by considering the conduction of heat from the sample into the fluid as well as the losses by radiation and convection an accurate determination of the thermal diffusivity is possible by means of a multiparametric fitting.

Another important experimental disadvantage in the orthogonal skimming scheme was mentioned earlier in this text, i.e. the need for careful laser alignment. Switching a sample and measuring is not that simple since every new sample must be realigned so the probe beam comes as close to the sample surface as possible.

3. Multi-ray Photothermal Beam Deflection

This section explores an improvement made to the photothermal beam deflection technique in its orthogonal surface skimming variant. In other to use the phase slope method measurements at different distances from the heating source are needed. Here, a method is proposed where in a single measurement the beam deflection signal can be obtained at the different offsets simultaneously.

Introduction

As previously discussed, the modulated orthogonal surface skimming variant utilizes a probe laser beam for sensing and an orthogonally positioned laser pump beam as the heating source. The pump beam is focused into a small spot incident on the sample surface and is modulated to generate thermal waves. These will then propagate through the sample and will heat the surrounding media. Temperature variations in a medium will translate to refractive index variations. A refractive index inhomogeneity, as seen in the previous section, will produce a deflection on a light beam going through the medium (George, Vallabhan et al. 2002). The deflection of the light beam can then be sensed with a quadrant photodetector (QPD) or similar device usually coupled to a lock-in amplifier.

As mentioned earlier, one of the ways to determine thermal diffusivity, α, using thermal waves is through the study of their spatial behavior (Salazar, Sanchez-Lavega et al. 1989), in our case the phase slope method is of interest due to its simplicity. To utilize the phase slope method the offset between the probe beam and the pump beam must be varied. The experimenter must adjust this offset and take one measurement for each of the desired number of points capturing the phase and amplitude of the deflection at each point. This procedure can be lengthy.

Specific Objectives

- Improve on the measuring times by using multiple probe beams and determining the thermal diffusivity of a sample with only one measurement.
- Develop sensing and processing techniques that eliminate the need for highly specialized equipment, e.g. a Lock-in Amplifier.

Theoretical background

One of the prevalent ways to study the mirage effect is through beam deflection (BD), which has been successfully used by many to monitor the temperature gradient field close to a sample surface. The technique was found to be sensitive and to have a relatively simple set-up. It is based on the measurement of the deflection of a light beam with respect to time.

The beam propagation through a spatially inhomogeneous RI is given by (Marchand 1978):

$$\frac{d}{ds}\left(n_0\frac{d\vec{r_0}}{ds}\right) = \nabla n(\vec{r},t) \tag{2.12}$$

here $\boldsymbol{r_0}$ is the displacement suffered by the beam from its original trajectory in a perpendicular direction, n_0 is the uniform index of refraction and $\nabla n(\vec{r},t)$ is the gradient of the index of refraction and the light path is denoted by *s*. By integrating over this path, we get:

$$\frac{d\vec{r_0}}{ds} = \frac{1}{n_0}\int_s \nabla n(\vec{r},t)ds \tag{2.13}$$

Assuming the deflection will be small and considering equation 2.2 we may rewrite the preceding expression in terms of the temperature as:

$$\frac{d\vec{r_0}}{ds} = \theta(t) = \frac{1}{n_0}\frac{\partial n}{\partial T}\int_s \nabla T(\vec{r},t)ds \tag{2.14}$$

As previously explained, the temperature gradient will depend on the sample geometry and the thermal properties of the sample and surrounding fluid.

The temperature field created by the pump beam in the surrounding medium will follow the same distribution as the one seen on the previous section (equation 2.8), as long as the thermal conductivity of the medium (k_γ) is much smaller than that of the sample and there is no absorption of the pump beam by the medium. The probe beam is considered to be parallel to the surface. We may divide the deflection ϕ into two components, a transversal (ϕ_T) and a normal one (ϕ_N), which are related to the temperature by the following expressions (Salazar, Sanchez-Lavega et al. 1989):

$$\phi_T = -\frac{1}{n}\frac{dn}{dT}\frac{P_0}{2\pi k_s}e^{i\omega t}\int_0^\infty \delta\,\mathrm{sin}(\delta y)\,e^{-\frac{(\delta a)^2}{4}}\beta_s^{-1}\frac{1+e^{-2\beta_s l}}{1-e^{-2\beta_s l}}e^{-\beta_\gamma z}d\delta\,\hat{k} \tag{2.15}$$

$$\phi_N = -\frac{1}{n}\frac{dn}{dT}\frac{P_0}{2\pi k_s}e^{i\omega t}\int_0^\infty \beta_\gamma\,\mathrm{cos}(\delta y)\,e^{-\frac{(\delta a)^2}{4}}\beta_s^{-1}\frac{1+e^{-2\beta_s l}}{1-e^{-2\beta_s l}}e^{-\beta_\gamma z}d\delta\,\hat{\jmath} \tag{2.16}$$

where *n* is the diffraction index, P_0 is the exciting beam power and a its $\frac{1}{e^2}$ diameter, k_s is the thermal conductivity of the sample, sub-indexes γ and s represent the medium and the sample respectively and $\beta_i = \delta^2 + \frac{i\omega}{\alpha_i}$ $(i = \gamma, s)$ and l is the sample's thickness. The transversal deflection is of central interest for this work since it has been shown to hold for the phase slope method (Salazar and Sanchez-Lavega 1994).

Experimental set-up

If multiple beams are to be used a sensing technique must be implemented to process the information for the beams simultaneously. The solution that has been implemented involves using a digital video camera to capture a video of the beams projected on a screen. The camera

used for our experiments is a Logitech C920 webcam. This camera offers resolution of 1920x1080 pixels, 8-bit pixel sensitivity and a maximum frame rate of 20 fps at full frame. The recorded film is then post-processed to obtain the transverse component of the deflection. This is achieved by tracking the position of the beams on the screen and then using lock-in amplification to get the phase of the deflection.

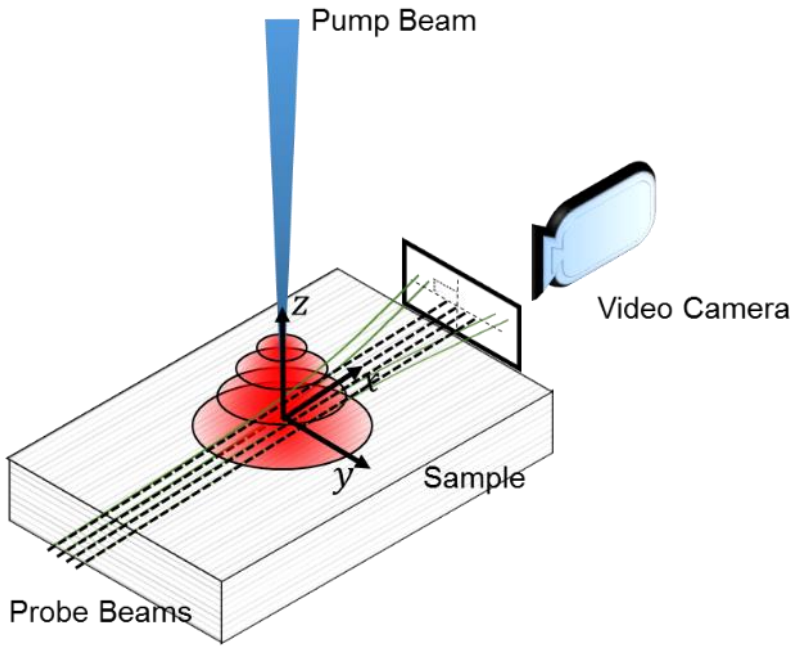

FIGURE 2-6. MULTIPLE BEAM TRAVERSING A RI GRADIENT

The multiple probe beams are generated using a diffraction grating and a 650-nm diode laser with tunable output power, the grating ($\sim 300\ lines/mm$) is carefully selected and positioned for each experiment to obtain as many beams as possible traveling close to the sample surface. A lens may be used to compensate for beam divergence. Other schemes may be used to generate the multiple probe beams, e.g. a wedge prism.

To intensify the deflection effect, the sample is submerged in a liquid with high a temperature coefficient of the refractive index, $\frac{dn}{dT}$, in our case acetonitrile. A spectrometric cuvette with a volume of $1\ cm^3$ is used as the measuring cell.

The beams are carefully aligned parallel to the sample surface. A 405-nm diode laser with tunable power output (maximum 1 W) is used as the pump beam. It is aligned to impinge on the sample surface perpendicularly and mounted on a micrometer precision positioner. The positioner allows for calibration of the distance between the probe beams. The pump beam is electronically on-off modulated utilizing the output of a function generator.

The beams are then projected onto a screen from which a video is recorded. A very small portion of the pump beam is deviated using a beam splitter and projected onto a corner of the

screen so that it can be used as a reference signal for post processing. Extreme care must be taken with this, if the deviated pump light is too intense it will pollute the video with synchronic noise that may be difficult to remove, a pinhole can help control this.

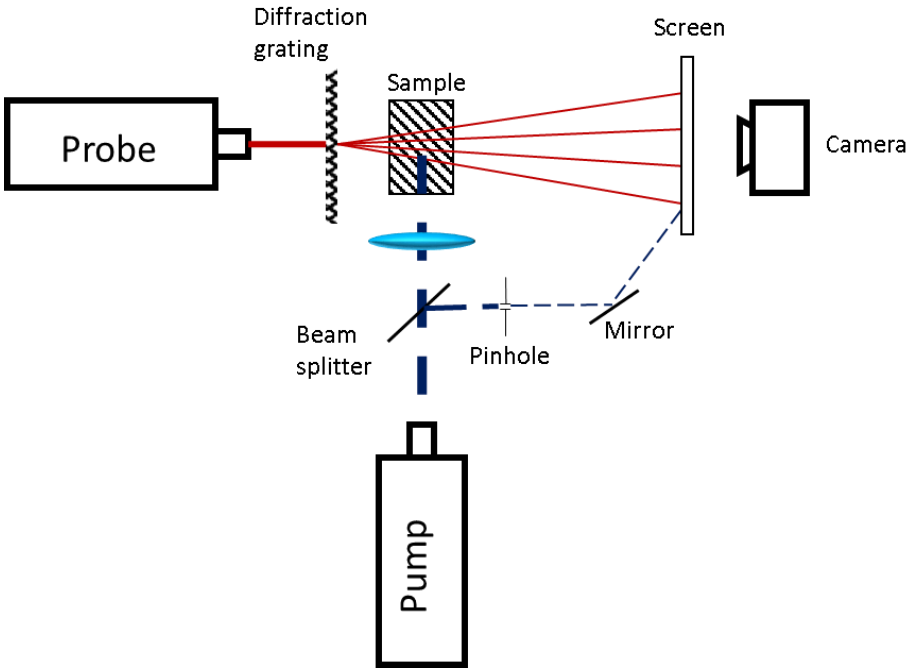

FIGURE 2-7. EXPERIMENTAL SET-UP SCHEMATIC

A measurement will consist of a video at a given frequency. The recording time will be the integration for the post-processing LIA. A single video yields the thermal diffusivity of the sample being measured, with no need of realigning, varying the probes position or the measurement frequency, while the set-up still requires careful alignment, measurement time is greatly improved under this configuration.

The output power of the pump beam is adjusted for each experiment depending on the sample absorption, care is taken so that the deflections seen on the screen are small. The output power of the probe beam must be adjusted so that the camera pixels don't saturate.

Data Processing

The position tracking of the beams is achieved by segmenting the video into as many sections as beams there are, with each segment containing only one beam for individual analysis. This process can be automated by analyzing the periodic variations in intensity through a Fourier transform of the image, peak localization among other methods. Some filtering and thresholding is needed to identify the beams properly. Figure 2-8 shows an example of such sectioning.

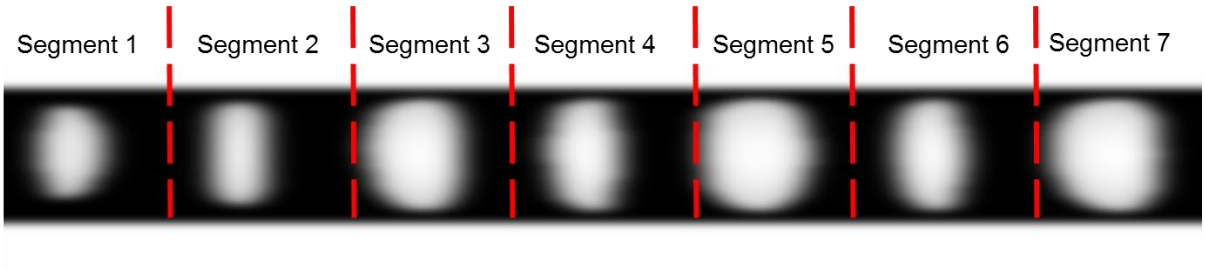

FIGURE 2-8 SECTIONING OF A MULTIPLE BEAM DEFLECTION VIDEO, IN THIS CASE THE SAMPLE IS A $CdTe$ FILM. NOT ALL SECTIONS ARE SHOWN. THIS IMAGE HAS BEEN DIGITALLY ENHANCED FOR VISUALIZATION PURPOSES

When the beam is deflected the lighting distribution in the section changes. If a vertical section midline is established and a comparison is made between the sum or weight of the values of the pixels to the right with those to the left of each frame in the video, then the beam transverse displacement can be easily obtained. This is pretty much the software implementation of a QPD, except that for sake of simplicity we are not processing the normal deflection, which could be obtained with the same process but by drawing a horizontal midline.

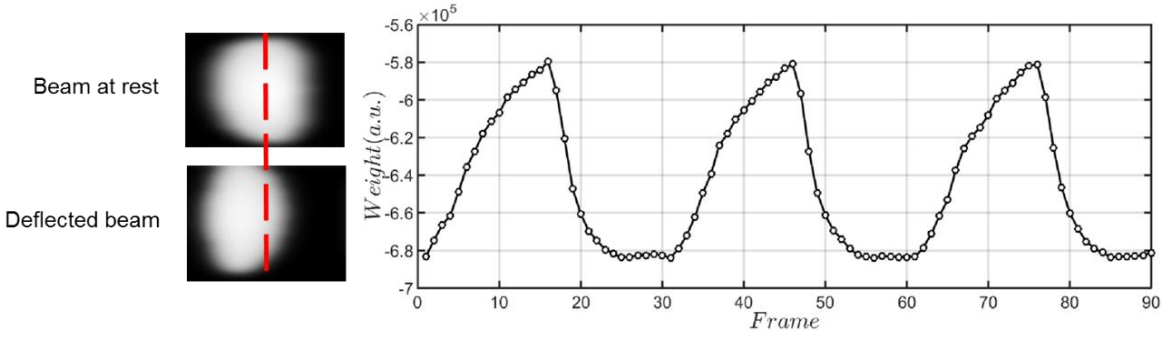

FIGURE 2-9 DEFLECTION OF THE BEAM IN SECTION 7 SEEN IN FIGURE 2-8, THE RED LINE SHOWS THE MIDDLE OF THE SECTION, THIS IS THE BOUNDARY FROM WHICH LEFT AND RIGHT PIXELS WILL BE WEIGHED AGAINST EACH OTHER. THE PLOT SHOWS THE EVOLUTION OF SAID WEIGHT WITH EACH FRAME, MODULATION FREQUENCY FOR THIS MEASUREMENT WAS 1 HZ. DOTS REPRESENT EXPERIMENTAL DATA WHILE THE SOLID LINE IS MERELY AN INTERPOLATION BETWEEN THEM.

Once the deflection data has been obtained, lock-in detection can be implemented. Lock-in detection requires a sharp reference signal for it to be effective. To perfectly sync this signal with our video, a small number of pixels in each image receive a minor fraction of the light from the pump beam obtained by means of a beam splitter. The sinusoidal reference signal is obtained by applying a Fourier transform to the mean temporal evolution of these pixels and extracting the first harmonic. While it would be in theory possible to simply obtain the Fourier transform of the deflection data and calculate the phase we have found that using lock-in amplification provides cleaner results.

The camera used is capable of recording RGB color video. This was used to our advantage; by using a pump beam with a wavelength in the blue portion of the spectrum (405 nm) and a red probe beam (650 nm) we can further reduce the noise that reflections from the pump beam might cause.

As discussed in the introductory chapter to this dissertation lock-in amplification involves mixing, i.e. multiplying, the experimental data with the reference signal and with an additional signal which has a 90° phase offset from this reference. The mixed signals are then low-passed filtered and two values are obtained. The in-phase value, *I*, results from the mixing with the original reference signal while the quadrature value, *Q*, results from the mixing with the 90° offset signal (Marín and Ivanov 2009, Cifuentes Castro 2014).

An important consideration is that the camera's speed limits the modulation frequency. The Nyquist sampling theorem tells us that the sampling rate of a band-limited signal must be at least twice as high in order to digitally reconstruct the signal properly, in our case, when working at full frame the maximum sampling frequency is 20 Hz, so modulation frequencies must be below 10 Hz (Smith 2003). A faster camera would allow for higher sampling frequencies.

Results and Discussion

Three samples with known thermal diffusivities were chosen for measurement. Figure 2-10 a) shows a typical experimental result, in this case a CdTe crystal. Figure 2-10 b) shows the result for two different steel types, i.e. D2 and AISI 1018. The slabs measured had a thickness off a few mm. For each measurement, an optimal measuring frequency is experimentally obtained. Although higher frequencies are desired, these also mean a reduction in the signal's amplitude so a compromise must be made.

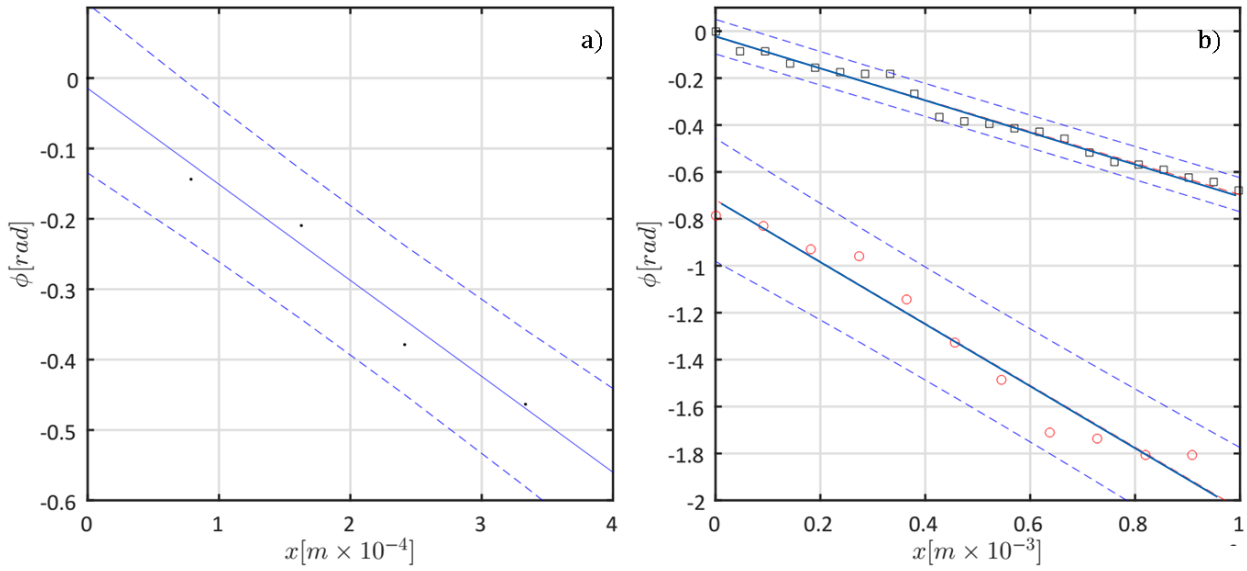

FIGURE 2-10 A) EXPERIMENTAL RESULT FOR A $CdTe$ SAMPLE, MODULATION FREQUENCY IS 4 HZ. THE DOTS SHOW EXPERIMENTAL DATA. B) EXPERIMENTAL RESULTS FOR TWO DIFFERENT STEEL TYPES, MODULATION FREQUENCY IS 2 HZ, SQUARES AISI108, CIRCLES D2. SOLID LINES REPRESENT THE BEST LINEAR FIT AND THE DASH LINES SHOW THE 95% CONFIDENCE INTERVAL FOR SAID FIT.

Table 2-1 shows the measured diffusivity values. The values obtained for the AISI 1018 steel and the cadmium telluride film are in good agreement with the reported literature value. A deviation exists from the D2 steel measured value and the reported value, this is likely due to normal variation between manufacturers since the AISI D2 standard. As for the high apparent error in the cadmium telluride measurement, this is due to a limited number of fitting points due to a relatively small sample (<1.5 mm).

TABLE 2-1 RESULTS

Sample	Measured Value	Literature Value
AISI 1018 low carbon steel	$(1.3 \pm 0.3)\times10^{-5}\ m^2/s$	$1.3\times10^{-5}\ m^2/s$(Automation Creations 2016)
D2 high carbon steel	$(3.9 \pm 0.6)\times10^{-6}\ m^2/s$	$5.6\times10^{-6}\ m^2/s$ (Automation Creations 2016)
CdTe	$(6.8 \pm 1.8)\times10^{-6}\ \mathrm{m}^2/s$	$7.2\times10^{-6}\ m^2/s$ (Alvarado, Zelaya-Angel et al. 1994)

Ongoing work

This work resulted in an internal collaboration with master student Eduardo Vargas. This has resulted in the measurement of filaments to experimentally corroborate that the slope method holds for good conductors. The following results stem from measurements taken by him under guidance of his thesis advisor, Ernesto Marín, and the author of this dissertation.

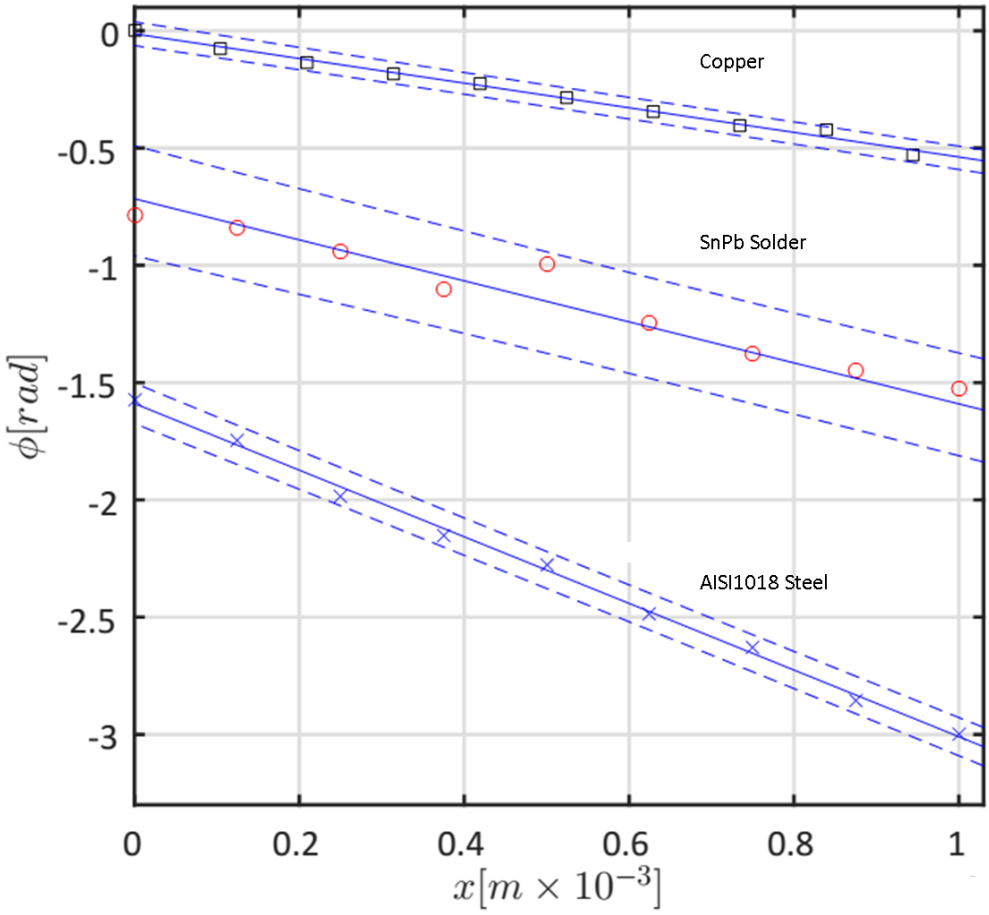

FIGURE 2-11 EXPERIMENTAL RESULTS FOR A MULTIBEAM DEFLECTION EXPERIMENT USING FILAMENTS OF COPPER (SQUARES), SNPB SOLDER (CIRCLES) AND AISI1018 STEEL (CROSSES). SOLID LINE INDICATES BEST LINEAR FIT, DOTTED LINE SHOWS 95% CONFIDENCE INTERVAL OF SAID FIT. MEASUREMENT FREQUENCY WAS OF 8.4 HZ.

TABLE 2-2 EXPERIMENTAL RESULTS FOR 3 DIFFERENT FILAMENTS. ERROR IS BASED IN THE 95% CONFIDENCE BOUND OF THE LINEAR FITTING

Material	$\alpha_s \left[\frac{m^2}{s}\right]$ measured	$\alpha_s \left[\frac{m^2}{s}\right]$ literature
Copper	$(1.0 \pm 0.1)\times10^{-4}$	1.1×10^{-4} (Touloukian, Powell et al. 1974)
SnPb	$(3.5 \pm 0.6)\times10^{-5}$	3.3×10^{-5} (Automation Creations 2016)
AISI1018	$(1.3 \pm 0.1)\times10^{-5}$	1.3×10^{-5}(Automation Creations 2016)

The method has been shown to obtain the thermal diffusivity of materials with a filament geometry in the range of $10^{-5}\ m^2/s$ to $10^{-4}\ m^2/s$. However, it has been experimentally observed that the measurement frequency must be higher than that of slabs to obtain an accurate reading. The number of points per experiment have also been increased due to an improved experimental configuration.

Conclusions

We have improved the photothermal beam deflection technique in its surface skimming variant by utilizing multiple beams and simultaneously sensing the refraction index changes at multiple points. The improvement utilizes digital signal and video processing techniques, replacing commonly utilized hardware, such as a QPD, with a digital video camera. Transversal deflection tracking was successfully implemented and amplified using a lock-in procedure. The method was validated by measuring three samples with known thermal diffusivities.

The method has been shown to be able to characterize both slab and filament samples. Care must be taken to utilize an appropriate measurement frequency, generally higher is better. This is attributed to having less disturbance by the surrounding media in the heat diffusion phenomena at higher frequencies.

4. Photothermal Shadowgraph

Here we present a novel application of the shadowgraph technique for obtaining the thermal diffusivity of an opaque solid sample inspired on the orthogonal skimming photothermal beam deflection technique. This new variant utilizes the shadow projected by the sample when put against a collimated light source. The sample is then heated periodically by another light beam, giving rise to thermal waves, which propagate across it and through its surroundings. Changes in the refraction index of the surrounding media due to the heating distort the shadow. This phenomenon is recorded and lock-in amplified in order to determine the sample´s thermal diffusivity.

Introduction

The shadowgraph method (Settles 2001) is an optical technique that allows us to visualize disturbances of the refractive index of a transparent medium. It utilizes an expanded collimated beam of light that crosses a field of refractive index inhomogeneity. Light passing through this medium will suffer deflections due to these disturbances, thus when this light is projected on to a screen a spatial modulation of the light intensity distribution, i.e. a shadow, is formed. Shadowgraphs have been used extensively in fluid mechanics and heat transfer research as an important visualization tool(Panigrahi and Muralidhar 2012).

In the area of photothermal techniques the study of the refractive index variations in a fluid surrounding a sample has been undertaken by the observation of the deflection of a narrow beam of light in a technique known as photothermal beam deflection (PBD) or mirage effect (Murphy and Aamodt 1980).

As previously discussed, PBD is a well-established technique in which a probe beam's course is altered by the change in the refraction index induced in the medium surrounding a sample undergoing a heating process. Although time resolved PBD techniques exist (Gensch and Viappiani 2003), this work is mainly interested in modulated PBD, and more specifically to the orthogonal beam surface skimming variant (Salazar, Sanchez-Lavega et al. 1991) which served as an inspiration for the experimental configuration that will be presented in this section.

Here, we are proposing and showing that the shadowgraph technique can be used successfully for measuring the thermal diffusivity of filaments in a manner like that of PBD orthogonal surface skimming variant. Shadowgraph offers a much faster measurement than PBD as the diffusivity of a sample can be obtained from a single measurement.

Specific Objectives

- Determine the thermal diffusivity of solid opaque samples using the mirage effect in conjunction with the shadowgraph technique and lock-in amplification.
- Develop and test a detection method that does not require a specialized camera with lock-in capabilities for measurement.

Theoretical Background

Let us assume that a set of parallel rays of light propagating in the z-direction enter a plane located at coordinate z_i and exit at a plane with coordinate z_e, with coordinate pairs x_i , y_i describing the entrance position of each ray of light (Fig. 1). Let L be the distance of the projection screen beyond the exit plane, n the refraction index of the transparent medium and sub-index "s" denote the coordinates on said screen. It is well-known that for a shadowgraph in which light rays are at normal incidence when entering the plane and undergo only infinitesimal deviations inside the inhomogeneous field but have a finite curvature will behave as follows:

$$x_s - x_i = L \int_{z_i}^{z_e} \frac{\partial(\log(n))}{\partial(x)} dz \tag{2.17}$$

$$y_s - y_i = L \int_{z_i}^{z_e} \frac{\partial(\log(n))}{\partial(y)} dz \tag{2.18}$$

If the infinitesimal displacement assumption can be extended to be valid in the region between the exit plane and the projection screen, the intensity I_s at point (x_s, y_s), which is the result of several beams moving from (x_i, y_i) and getting mapped onto (x_s, y_s) is given by:

$$I_s(x_s, y_s) = \sum_{(x_i, y_i)} \frac{I_0(x_i, y_i)}{\left|\frac{\partial(x_s, y_s)}{\partial(x_i, y_i)}\right|} \tag{2.19}$$

where I_0 is the intensity at the region of study. Moreover, the Jacobian $\frac{\partial(x_s, y_s)}{\partial(x_i, y_i)}$ can be further simplified as long as the beam deflections δ_x and δ_y are small (4).

$$\left|\frac{\partial(x_s, y_s)}{\partial(x_i, y_i)}\right| \approx 1 + \frac{\partial(x_s - x_i)}{\partial(x)} + \frac{\partial(y_s - y_i)}{\partial(y)} \tag{2.20}$$

Therefore, the governing equation for the shadowgraph under these assumptions and integrating for the dimension of the experimental apparatus (the length of the RI inhomogeneity), D, is:

$$\frac{I_0 - I_s}{I_s} = (L \times D) \nabla^2 \log(n(z, y)) \tag{2.21}$$

Further insight into the mathematical equations governing shadowgraphs can be found elsewhere. (Settles 2001) (Lewis 1985).

To mitigate the effects of multidimensional heat-flow through the sample, a thin filament geometry was proposed for this work. The filament is heated using a modulated light source. For the purposes of theoretical analysis, the light source is assumed to have a rectangular geometry with a Gaussian distribution in the z direction and its radius at $\frac{1}{e^2}$ given by b, and uniformly distributed in the x direction. The filament is assumed to be semi-infinite in the z direction.

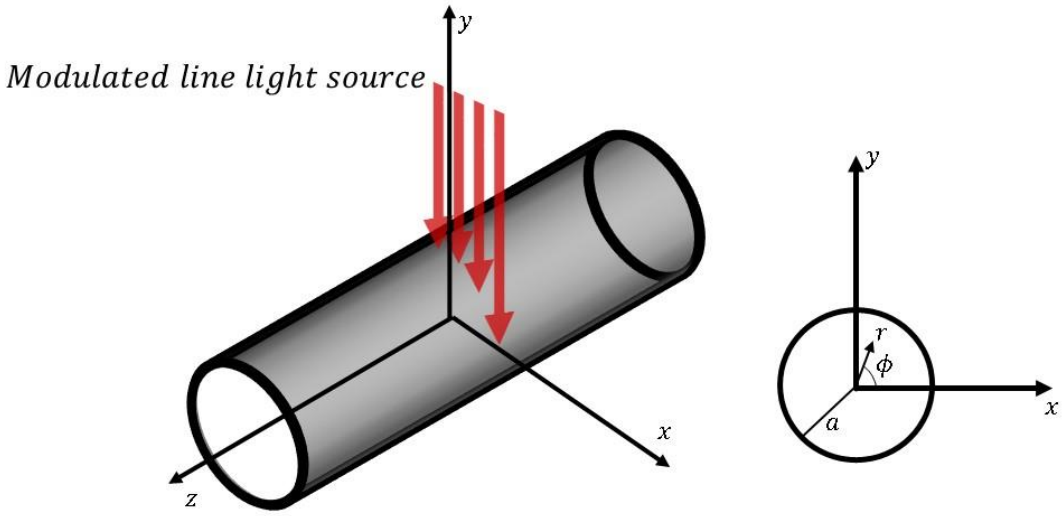

FIGURE 2-12. PROBLEM GEOMETRY SEEN IN CYLINDRICAL COORDINATES.

Filament surface temperature behavior has been reported to be highly dependent on the thermal characteristics of the surrounding medium (Mendioroz, Fuente-Dacal et al. 2009) so for the objectives of this work an adequate analysis that includes conductive heat losses to the medium is needed. The model developed by Salazar et al. suits this purpose. The oscillatory temperature distribution generated by an optically opaque filament in the fluid will be given by(Salazar, Mendioroz et al. 2010):

$$T_\gamma = \int_{-\infty}^{\infty} e^{i\lambda z}\left(\frac{P_0}{4\pi k_s \beta_s}\right)\left[\sum_{n=-\infty}^{\infty} \frac{(-i)^n \cos\left(\frac{n\pi}{2}\right)}{\pi(1-n)^2} e^{-\frac{\lambda^2 b^2}{8}} I_n(\beta_s a) K_n(\beta_\gamma r) e^{in\phi}}{K_n(\beta_\gamma) I_n'(\beta_s a) - G + H}\right] d\lambda \qquad (2.22)$$

$$G = \frac{k_\gamma \beta_\gamma}{k_s \beta_s} K_n'(\beta_\gamma a) I_n(\beta_s a)$$
$$H = \frac{h}{k_s \beta_s} K_n(\beta_\gamma a) I_n(\beta_s a)$$
$$\beta_i^2 = \frac{i\omega}{\alpha_i} + \lambda^2$$

where sub-indices γ and s stand for gas and sample, correspondingly, k is the thermal conductivity, α is the thermal diffusivity, a is the filaments radius, h is the convective and radiative heat loss coefficient and ω is the angular modulation frequency.

As mentioned earlier in this work, this temperature field, when analyzed at distances close to the object's surface and when the sample has a larger thermal diffusion length than the surrounding media ($y \ll \mu_\gamma \ll \mu_s$), displays an inverse proportionality between the sample's thermal diffusion length (10) and *m,* i.e. the phase slope method. Where *m* is defined as the slope between the phase lag (Φ) and the offset to the heat source. This relation is of great interest as it provides a straight forward method for determining the sample's thermal diffusivity.

$$-m_\Phi = \frac{1}{\mu_s} \tag{2.23}$$

Suppose that the change in the refraction index, Δn, is directly proportional to the change in temperature, ΔT, and related by the the temperature coefficient of the refractive index, $\frac{dn}{dT}$, so that the refraction index field follows the same distribution as the thermal field seen in equation 2.21 (Sell 1989). Under this assumption equations 2.21 and 2.22 can be used to synthetically approximate a shadowgraph for a semi-infinite slab ($\mu_s \ll l$), as will be shown further on this section. It is important to note that a fluid with a higher $\frac{dn}{dT}$ will contribute to signal magnitude, but will have no additional effect on the result.

Simulation

A numerical simulation was carried out to show that equation 2.23 holds when a shadowgraph is used to indirectly assess the temperature field and to further the understanding on the technique limits. The optically opaque sample filament is assumed to be submerged in acetonitrile, a solvent for which thermal and optical properties are well known (Terazima 1996), and which has a relatively high $\frac{dn}{dT}$. Three different modulation frequencies were chosen and a range of four different sample thermal diffusivities were utilized. Additional simulation parameters are shown in Table 2.2-3 (the $\frac{dn}{dT}$ value at the used wave-length was corroborated by measurements using a fiber optic refractive index spectrometer described elsewhere (Vaca-Oyola, Marín et al. 2016)).

Equation 2.21 allows us to obtain a simplified shadowgraph, however it does not allow us to account for the refractive index variation in the x direction. To work around this limitation, given that only a small light-path deviation is expected in a short distance, the average of the refractive index of the medium transversed by a light beam travelling in a straight path is used. The distance in x used for this average is in twice that of the thermal diffusion length of the medium, μ_γ.

To simplify the simulation of equation 2.22 a fixed thermal conductivity was used. The chosen value of $100\left[\frac{W}{mK}\right]$ is intended to represent the usual order of magnitude of thermal conductivity in metals. Note that this value is needed to simulate the influence of conductive heat losses to the medium, it is not the objective of this work to measure this parameter. Simulation parameters are shown below.

TABLE 2.2-3 SIMULATION PARAMETERS

Parameter	*Value*
α_γ	$1.075\times10^{-7}\left[\frac{m^2}{s}\right]$
k_γ	$0.2\left[\frac{W}{mK}\right]$
k_s	$100\left[\frac{W}{mK}\right]$
$\frac{dn_\gamma}{dT}$	$4.5\left[\frac{10^{-4}}{K}\right]$
n	1.3441
a	$100\ \mu m$
b	$100\ \mu m$
L	$0.01\ [m]$
D	$2\mu_\gamma$
h	$10\left[\frac{W}{m^2K}\right]$

Additionally, the simulation was programmed to output an amplitude and a phase image for a $100\ \mu m$ platinum filament ($k_s = 71.6\left[\frac{W}{mK}\right]$, $\alpha_s = 2.7\times10^{-5}$), one of the samples to be measured. Figure 2-13 shows the simulation output for a full $3\ mm \times 0.3\ mm$ shadowgraph as a colored contour plot. The phase has been corrected for quadrant changes.

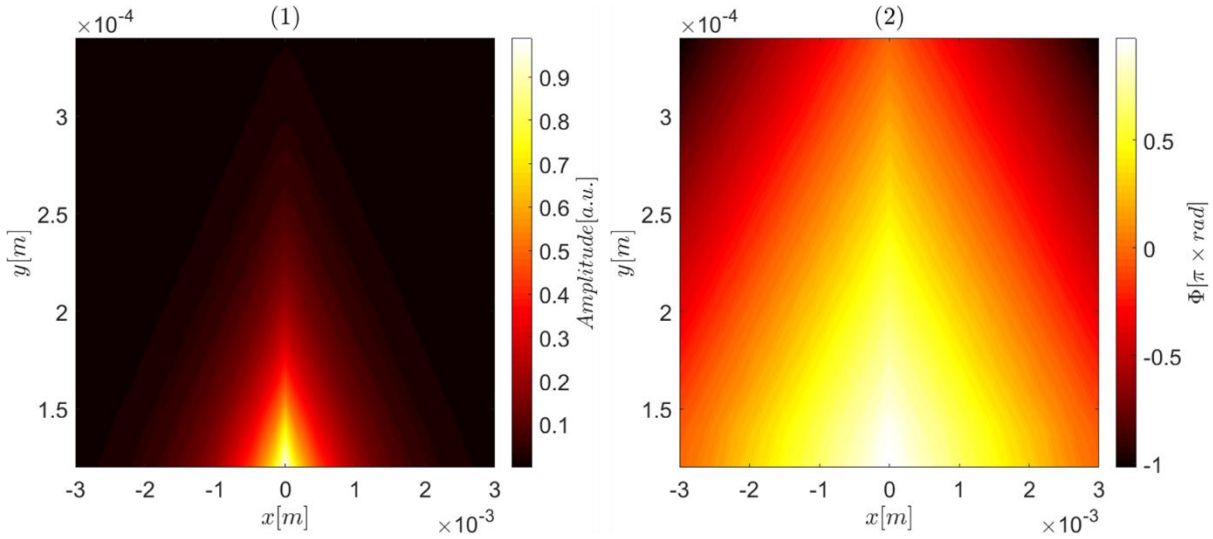

FIGURE 2-13 SIMULATION RESULTS FOR A $100\ \mu m$ PLATINUM FILAMENT ($k_s = 71.6\left[\frac{W}{mK}\right]$, $\alpha_s = 2.7\times10^{-5}$) AND $8\ Hz$ MODULATION FREQUENCY. (1) AMPLITUDE (2) PHASE

An important note on these numerical simulations is that equation 2.22 is a highly oscillatory function. This means that numerical approximation can be difficult under several circumstances. The simulations results are approximations to the actual behavior described by this equation. Numerical errors are to be expected, however care has been taken so that their effect is minimized.

Simulations for a range of thermal diffusivities and frequencies are shown in Figure 2-14. It is important to note that only the information given by the pixels closest to the sample surface has been plotted, in this case $20\mu m$ above the sample surface. It is from these data points that the slope referred to in equation 2.23 is obtained. The main objective is to estimate the sample's thermal diffusivity, $\hat{\alpha}_s$, from the slope and to obtain the error, ϵ, by comparing it to the actual value, α_s, used for the simulation. The linear fit considers the 10 points furthest from the center that behave linearly to avoid the influence of the nonlinear behavior seen near $x = 0$. Fitting results are shown in Table 2.2-4.

TABLE 2.2-4 SIMULATION RESULTS

$\alpha_s\left[\frac{m^2}{s}\right]$	$f\ [Hz]$	$m\ \left[\frac{rad}{m}\right]$	R^2	$\hat{\alpha}_s\left[\frac{m^2}{s}\right]$	ϵ [%]
1.00×10^{-8}	2	-7460.7	1.000	1.13×10^{-7}	1028.8
	4	-12323.4	0.999	8.27×10^{-8}	727.5
	8	-15224.1	1.000	1.08×10^{-7}	984.4
1.00×10^{-7}	2	-8197.3	0.999	9.35×10^{-8}	6.5
	4	-11109.7	1.000	1.02×10^{-7}	1.8
	8	-15627.4	1.000	1.03×10^{-7}	2.9
1.00×10^{-6}	2	-2504.7	1.000	1.00×10^{-6}	0.2
	4	-3563.9	1.000	9.89×10^{-7}	1.1

1.00×10^{-5}	8	-5004.9	1.000	1.00×10^{-6}	0.3
	2	-844.4	1.000	8.81×10^{-6}	11.9
	4	-1147.3	1.000	9.55×10^{-6}	4.5
	8	-1590.9	0.995	9.93×10^{-6}	0.7

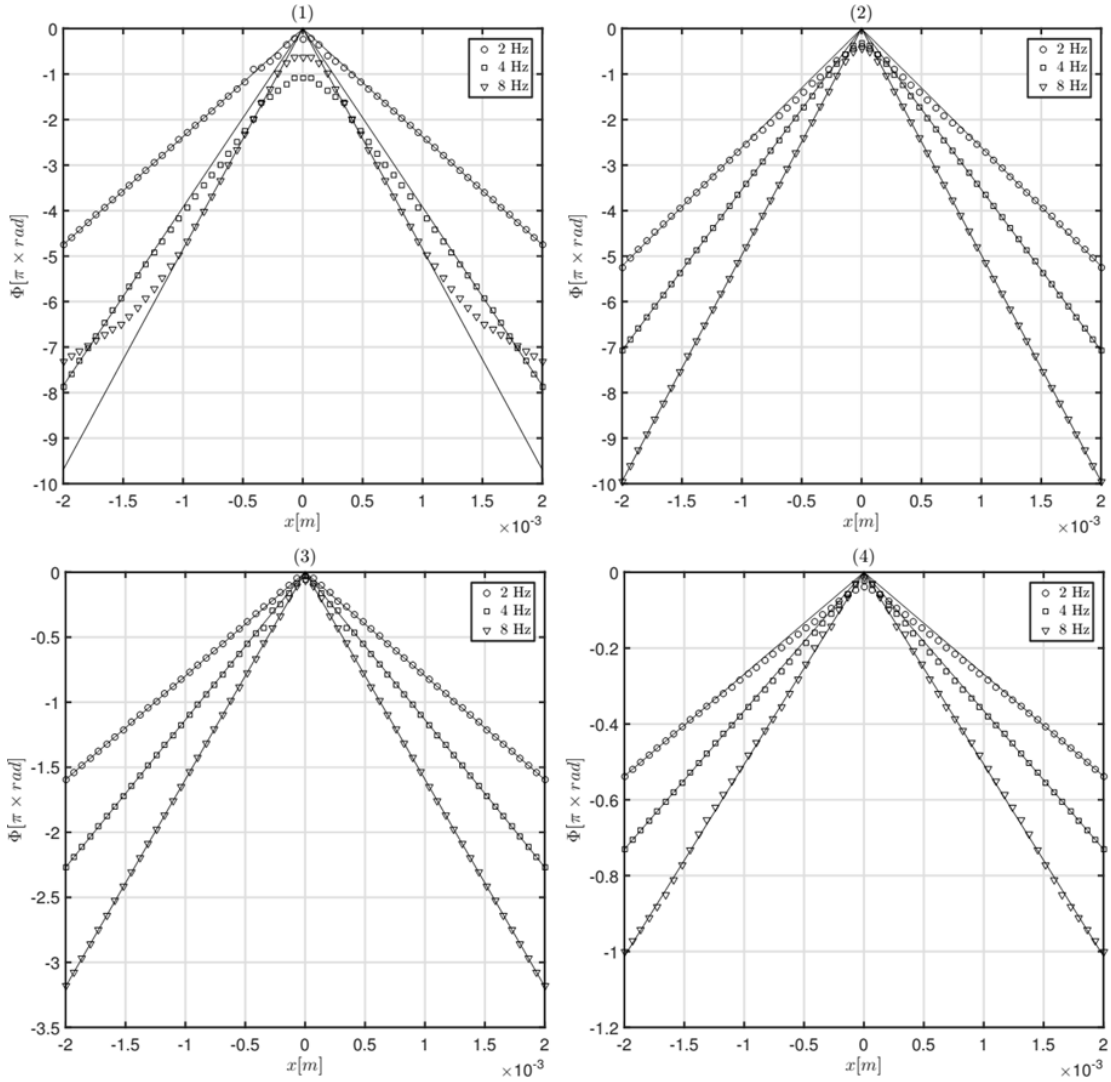

FIGURE 2-14 SIMULATION RESULTS AT Y=0 FOR DIFFERENT THERMAL DIFFUSIVITIES. (1) $\alpha_s = 1\times10^{-8}$, (2) $\alpha_s = 1\times10^{-7}$,(3) $\alpha_s = 1\times10^{-6}$ AND (4) $\alpha_s = 1\times10^{-5}$. MODULATION FREQUENCIES ARE SHOWN WITH DIFFERENT BULLETS WHILE THE SOLID LINES INDICATE THE BEST LINEAR FIT.

The simulation confirms that as long as $\mu_\gamma \ll \mu_s$ and heat losses by conduction convection and radiation can be disregarded, the slope obtained from the intensity change phase lag versus heat source offset will be governed by the thermal diffusivity of the sample. It is also important to note that with lower frequencies linearity occurs at a larger offset and a larger error is also to be expected. This effect is exacerbated due to the pump beam's dimensions and care should be taken when analyzing experimental data.

Experimental Procedure

The probe light source in our experimental array is obtained by widening and collimating a laser beam. This is opposite to a PBD experiment which requires a narrow probe beam. In our setup, the sample has been submerged in a medium with a high temperature coefficient of refractive index $\left(\frac{dn}{dT}\right)$, e.g. acetonitrile. By doing this, we maximize the changes of the refractive index making other effects, such as the sample's thermal expansion, smaller by comparison and therefore negligible.

A laser beam with a spot size as small as possible, focused using proper optics, and orthogonally positioned with respect to the probe light source is used to heat the sample periodically generating the thermal waves which will diffuse over the length of the sample. The laser used is a 445nm diode laser with tunable power output.

While our numerical simulations were done for slabs, the method should hold for rods and filaments as well, we have taken onto the task of showing this experimentally. The optically thick filament or rod sample is placed within a measuring cell, which has a maximum volume of 1 cm^3, and submerged in acetonitrile. The samples chosen for measurement have thermal diffusivities above $1\times10^{-5}\ \frac{m^2}{s}$, this is to guarantee that conduction to the media will be negligible when compared to conduction within the sample. The cell is placed directly in the trajectory of the expanded probe beam generating the shadow.

Said shadow can then be projected on a screen or directly at the sensing element. The camera used is a FLIR SC2500 working on the near infrared portion of the spectrum with a 320x256 pixel InGaAs sensor, a maximum frame rate of 340Hz at full frame and on-board lock-in detection capabilities. This camera offers 14-bit pixel sensitivity. The wavelength of the probe used was 790 nm.

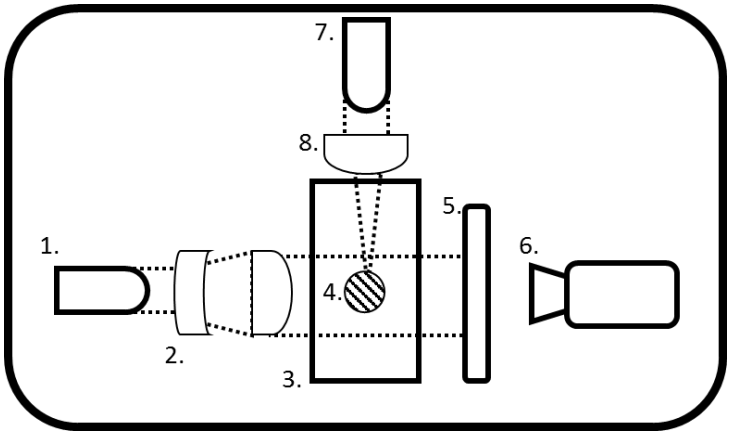

FIGURE 2-15 EXPERIMENTAL CONFIGURATION. (1) PROBE BEAM, (2) COLLIMATING LENSES, (3) CELL, (4) SAMPLE, (5) PROJECTION SCREEN, (6) CAMERA, (7) PUMP BEAM, (8) FOCUSING LENS.

The pixels closest to the sample's surface can be automatically identified using edge detection techniques. For this a reference image with the pump beam turned off is used. As confirmed by the simulation it is important for the pixels to be as close to the shadow's horizon as possible, otherwise the effects of heat diffusion through the surrounding liquid would become more prominent and would alter the results. With the adequate optical elements pixel resolutions equivalent to a few tens of microns at the sample's surface have been obtained.

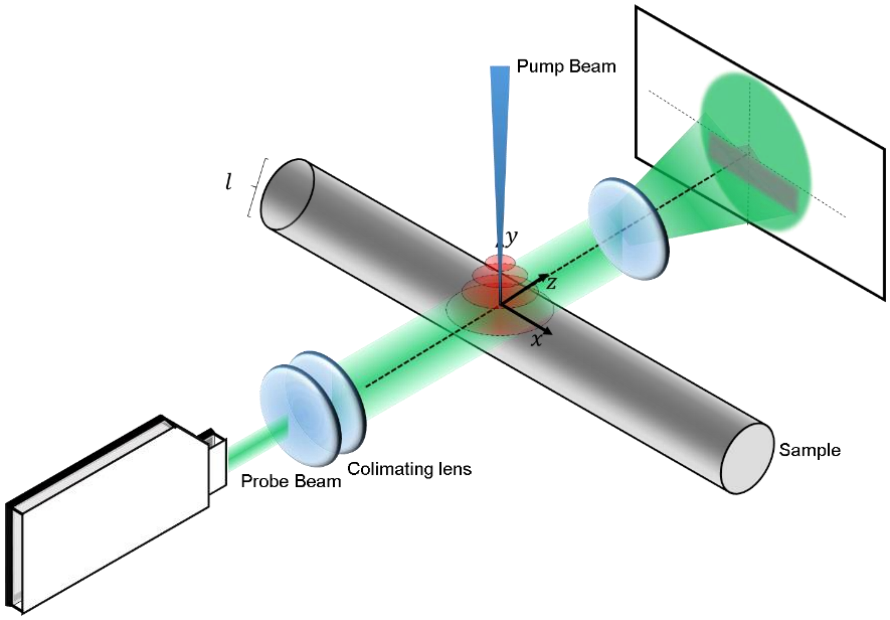

FIGURE 2-16 3D PERSPECTIVE OF THE PHOTOTHERMAL SHADOWGRAPH EXPERIMENTAL SETUP

Lock-in amplification is an important part of the information processing. In a lock-in amplifier (LIA) an amplitude modulated signal can be reconstructed in both phase and amplitude if a reference signal is known, even in extremely noisy environments (Marín and Ivanov 2009, Cifuentes and Marín 2015). Measurements taken with the SC2500 camera directly output two images, one for phase and another for amplitude.

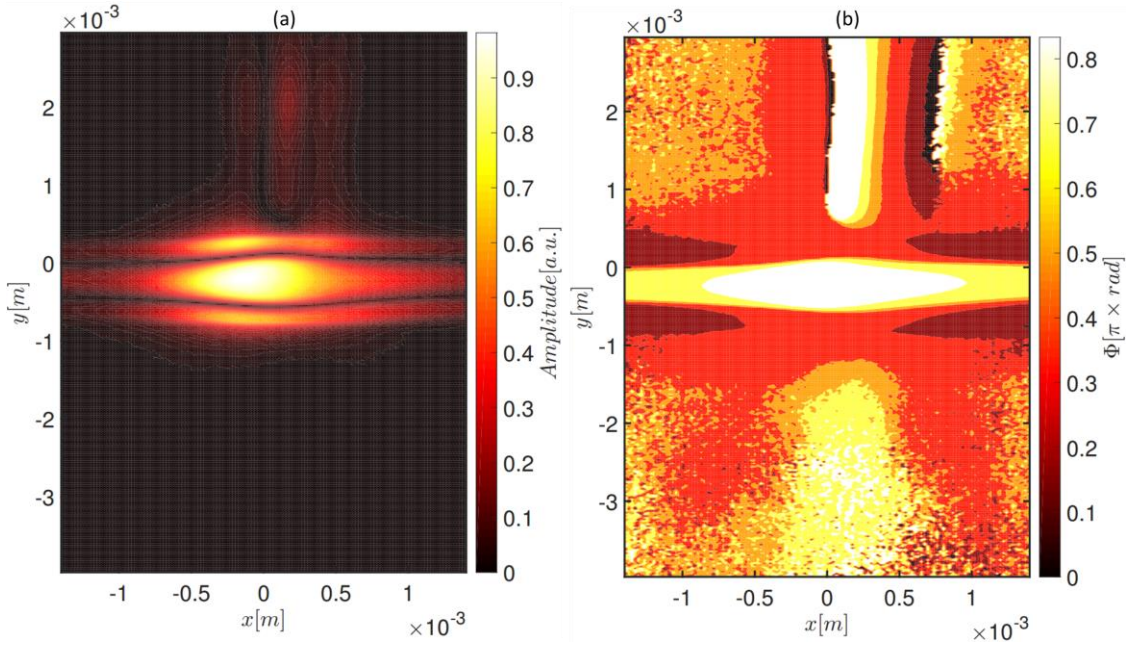

FIGURE 2-17 IMAGERY RESULTING FROM A LOCK-IN SHADOWGRAPH OF A PLATINUM FILAMENT USING MODULATION FREQUENCY OF 8 HZ OBTAINED WITH THE SC2500 CAMERA, (A) AMPLITUDE, (B) PHASE.

Figure 2-17 shows a typical experimental result. In this particular case, the sample generating the shadowgraph imagery is a platinum filament with diameter of 76.2 μm. The filament is placed horizontally. Note that in the images excitation laser absorption in the surrounding media is visible. However, the effect is small and is rapidly extinguished with distance introducing little to no distortion in the result. Figure 2-18 shows a zoom in of the phase image from the figure above so that the pixels closest to the filament can be appreciated more easily.

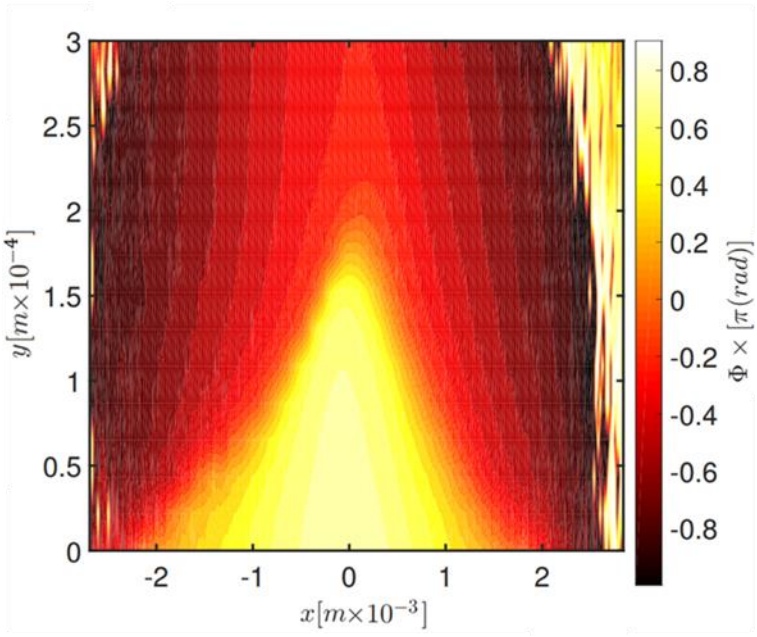

FIGURE 2-18 ZOOM IN OF THE PHASE IMAGE SHOWN IN FIGURE 2-17

Figure 2-19 shows the phase lag vs. offset curve for the pixel row closest to the platinum filament's surface. It is from this data that the thermal diffusivity is to be obtained. This process is repeated for each of the samples. Although Figure 2-19 shows both slopes only one slope is needed. Obtaining a single slope allows for the camera to cover a larger distance from the heat source.

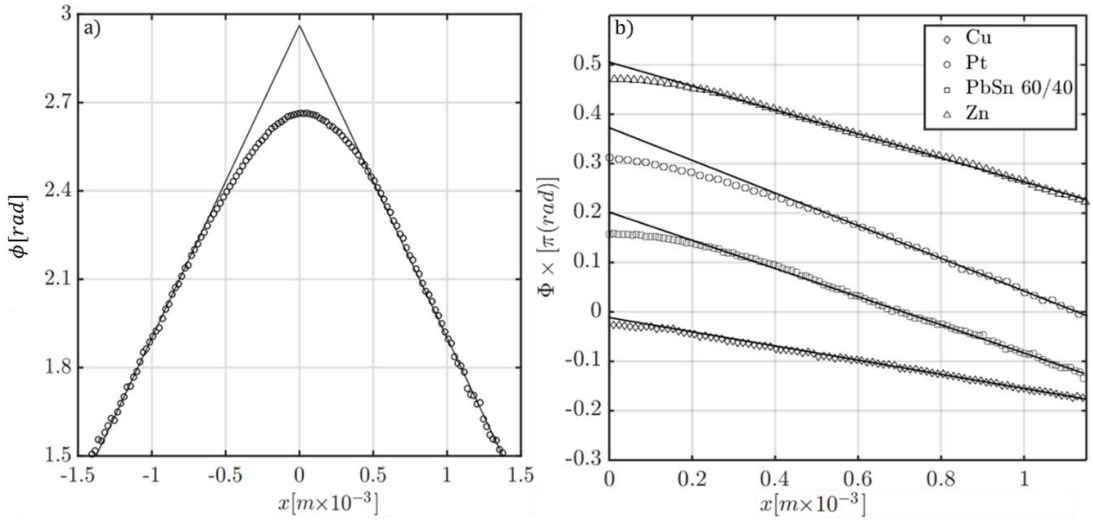

FIGURE 2-19. A) PHASE-LAG VS. HORIZONTAL OFFSET OBTAINED FROM THE PIXEL ROW CLOSEST TO THE PLATINUM FILAMENT'S SURFACE USING MODULATION FREQUENCY OF 8 HZ OBTAINED WITH THE SC2500 CAMERA. SOLID LINE SHOWS BEST LEAST SQUARES LINEAR FIT, BULLETS SHOW EXPERIMENTAL DATA. B)

PHASE LAG VS. HORIZONTAL OFFSET OF THE PIXEL CLOSEST TO THE SAMPLE'S SURFACE FOR CU, PT, PBSN (60/40) AND ZN SAMPLES, ONLY ONE SLOPE IS SHOWN.

While simulation shows that higher frequencies should be favored, signal strength drastically diminishes as frequency rises so a compromise must be reached. Although it is possible in some cases to reach frequencies in the order of tens of hertz, other samples must be measured using modulation of only a couple of hertz or the signal becomes too small to be measured reliably. Table 2-5 shows the results for four different samples and the value reported in different literature sources.

TABLE 2-5 RESULTS: THERMAL DIFFUSIVITY MEASURED BY THE PHOTOTHERMAL SHADOWGRAPH METHOD $f = 8Hz$

Material	$\alpha_s \left[\frac{m^2}{s}\right]$ measured by shadowgraph	$\alpha_s \left[\frac{m^2}{s}\right]$ literature
Copper	$(1.2 \pm 0.1) \times 10^{-4}$	1.1×10^{-4} (Touloukian, Powell et al. 1974)
Platinum	$(2.4 \pm 0.1) \times 10^{-5}$	2.52×10^{-5} (Touloukian, Powell et al. 1974)
Zinc	$(4.2 \pm 0.2) \times 10^{-5}$	4.16×10^{-5} (Touloukian, Powell et al. 1974)
PbSn Solder (40/60)	$(3.3 \pm 0.1) \times 10^{-5}$	3.34×10^{-5} (Automation Creations 2016)

A few measurement runs were also carried out using a CMOS Logitech C920 web-camera to show that the technique does not require highly specialized hardware. This camera offers resolution of 1920x1080 pixels, 8-bit pixel sensitivity and a maximum frame rate of 20 fps at full frame. The probe beam selected for this camera was a 445-nm diode laser.

Although the SC2500 camera has onboard lock-in capabilities, the C920 does not, so specialized self-referenced lock-in software was developed for this application. Basically, a video is recorded for several pump beam excitation cycles, the video is then post-processed. A small number of pixels are illuminated by light taken from the pump beam and used to obtain a crisp reference signal; in the case of the signal not being sinusoidal, e.g. a square pulse, its Fourier transform is computed and only the first harmonic is used. This signal is then used for the lock-in amplification procedure which is carried out pixel by pixel, frame by frame. The result is a phase image and an amplitude image just as with the SC2500.

Figure 2-20 shows the amplitude and phase imagery obtained for the same platinum measured in Figure 2-17 but using the C920 webcam. Since pixel sensitivity is reduced the measurement is noisier; however, pixel density is increased offering some compensation.

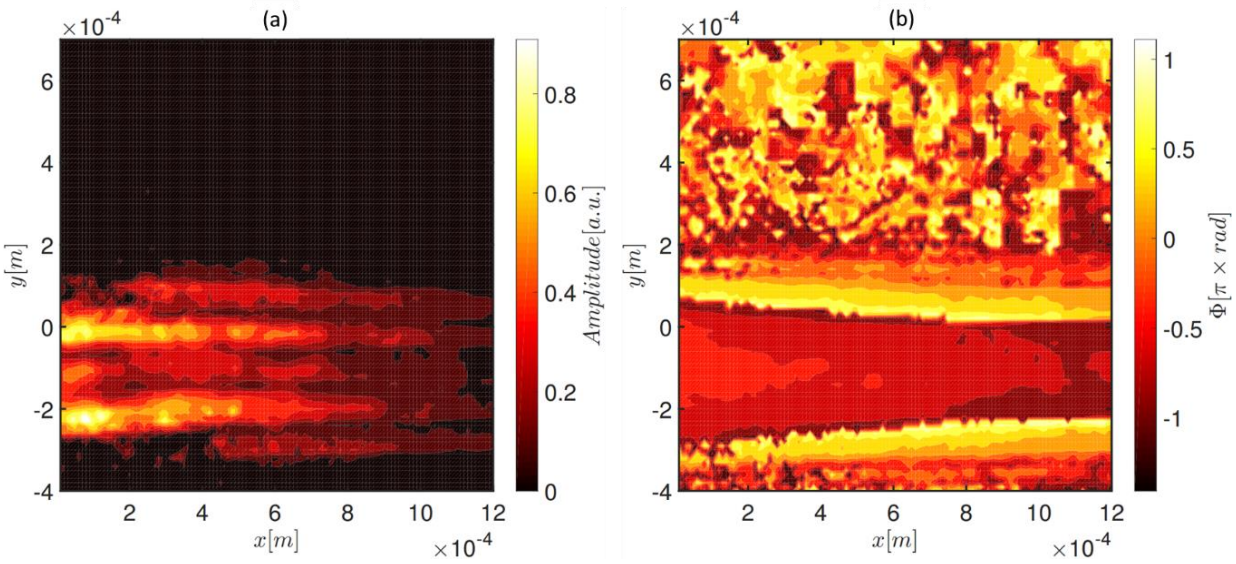

FIGURE 2-20 IMAGERY RESULTING FROM A LOCK-IN SHADOWGRAPH OF A PLATINUM FILAMENT USING MODULATION FREQUENCY OF 8 HZ OBTAINED WITH THE C920 CAMERA, (A) AMPLITUDE, (B) PHASE.

Figure 2-21 shows the phase lag vs. offset curve for the pixel row closest to the filament's surface. The diffusivity of platinum obtained from this data, $\alpha = (2.44 \pm 0.1)\times 10^{-5}\frac{m^2}{s}$, agrees with that obtained above and with the value reported in literature (Table 2-5). This shows that the technique can be implemented successfully using modest sensing equipment.

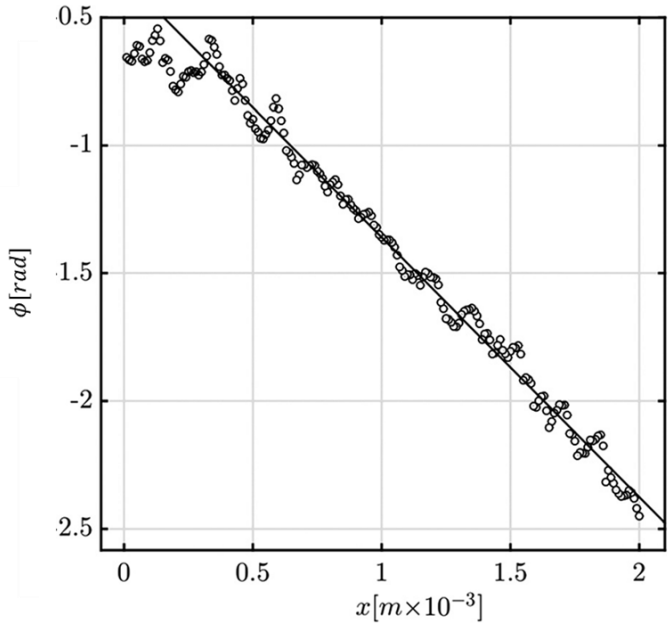

FIGURE 2-21 EXPERIMENTAL MEASUREMENT FOR THE PLATINUM FILAMENT. BULLETS SHOW EXPERIMENTAL DATA WHILE THE SOLID LINE SHOWS THE BEST LINEAR FIT.

Conclusions

The shadowgraph technique was successfully used to obtain the thermal diffusivity of different samples through the phase slope method. The technique was validated through numerical simulation and experimental results. Shadowgraphs had previously been used in the study of different phenomena but had not been, to the best of our knowledge, employed in quantitative detection schemes involving lock-in amplification for photothermal experiments. The experimental results obtained are in good agreement with the values found in literature, making the technique a promising alternative to currently established methods.

While the phase slope method was used for this experimental set-up, in principle the amplitude could also be used. However, it resulted in noisy measurements, probably due to optical imperfections, and was excluded from this work. This is an area for future work and further improvement. The technique could also be used to study other sample geometries and sample fluid interactions.

We have also shown that highly specialized hardware is not required for the technique to work, a simple webcam can be used as the sensing element. This makes the photothermal shadowgraph technique highly accessible.

5. References

Alvarado, J., et al. (1994). "Thermal properties of CdTe." Journal of Applied Physics **76**(11): 7217-7220.

Automation Creations, I. (2016, January 2, 2016). "60-40 Soft Solder (60 Sn-40Pb) - ASTM B 32 Grade Sn60." from http://www.matweb.com/.

Automation Creations, I. (2016, January 2, 2016). "AISI 1018 Steel, cold drawn." from http://www.matweb.com/.

Automation Creations, I. (2016, January 2, 2016). "Bohler-Uddeholm AISI D2 Cold Work Tool Steel." from http://www.matweb.com/.

Automation Creations, I. (2016, January 2, 2016). "Mateck Cadmium Telluride (CdTe)." from http://www.matweb.com/.

Barkyoumb, J. and D. Land (1995). "Thermal diffusivity measurement of thin wires using photothermal deflection." Journal of Applied Physics **78**(2): 905-912.

Bertolotti, M., et al. (1998). "Analysis of the photothermal deflection technique in the surface reflection scheme: Theory and experiment." J. Appl. Phys. **83**(2): 966.

Cifuentes, A. and E. Marín (2015). "Implementation of a field programmable gate array-based lock-in amplifier." Measurement **69**: 31-41.

Cifuentes Castro, Á. S. (2014). Implementación de un amplificador sincrónico digital (Lock-in) usando un dispositivo FPGA (Field Programmable Gate Array). CICATA. Mexico City, Instituto Politécnico Nacional. **Master**.

Fournier, D. and A. Boccara (1988). Photothermal investigation of solids: basic physical principles. Photoacoustic Investigations of Solids and Fluids. J. A. Sell. San Diego, CA, Academic Press**:** 35-79.

Fournier, D., et al. (1980). "Sensitive insitu trace-gas detection by photothermal deflection spectroscopy." Applied Physics Letters **37**(6): 519-521.

Gensch, T. and C. Viappiani (2003). "Time-resolved photothermal methods: accessing time-resolved thermodynamics of photoinduced processes in chemistry and biologyDedicated to Professor Silvia

Braslavsky, to mark her great contribution to photochemistry and photobiology particularly in the field of photothermal methods." Photochemical & Photobiological Sciences **2**(7): 699.

George, N. A., et al. (2002). "Photothermal deflection studies of GaAs epitaxial layers." Applied Optics **41**(24): 5179.

Lewis, R. (1985). "Quantitative shadow method for measuring a one dimensional refractive index distribution." Optical engineering **24**(6): 1093-1097.

Marchand, E. W. (1978). "Gradient Index Optics." Gradient Index Optics by Erich w. Marchand New York, NY: Academic Press, 1978.

Marín, E. and R. Ivanov (2009). "LIA in a Nut Shell: How can Trigonometry help to understand Lock-in Amplifier operation? ." Lat. Am. J. Phys. Educ. **3**(3): 3.

Mendioroz, A., et al. (2009). "Thermal diffusivity measurements of thin plates and filaments using lock-in thermography." Rev Sci Instrum **80**(7): 074904.

Murphy, J. C. and L. C. Aamodt (1980). "Photothermal spectroscopy using optical beam probing: Mirage effect." Journal of Applied Physics **51**(9): 4580.

Panigrahi, P. K. and K. Muralidhar (2012). Schlieren and shadowgraph methods in heat and mass transfer, Springer.

Salazar, A., et al. (2010). "Accurate measurements of the thermal diffusivity of thin filaments by lock-in thermography." Journal of Applied Physics **107**(4): 043508.

Salazar, A. and A. Sanchez-Lavega (1994). "Thermal diffusivity measurements using linear relations from photothermal wave experiments." Rev. Sci. Instrum. **65**(9): 2896.

Salazar, A., et al. (1989). "Theory of thermal diffusivity determination by the mirage technique in solids." J. Appl. Phys. **65**(11): 4150.

Salazar, A., et al. (1991). "Thermal diffusivity measurements in solids by the mirage technique: Experimental results." J. Appl. Phys. **69**(3): 1216.

Salazar, A., et al. (1993). "Thermal diffusivity measurements on solids using collinear mirage detection." Journal of Applied Physics **74**(3): 1539-1547.

Sell, J. A. (1989). Photothermal investigations of solids and fluids. San Diego, CA Academic Press, Inc.
.

Settles, G. S. (2001). Schlieren and Shadowgraph Techniques, Springer Berlin Heidelberg.

Smith, S. W. (2003). Digital signal processing: a practical guide for engineers and scientists, Newnes.

Terazima, M. (1996). "Refractive index change by photothermal effect with a constant density detected as temperature grating in various fluids." The Journal of Chemical Physics **104**(13): 4988.

Touloukian, Y. S., et al. (1974). Thermophysical Properties of Matter-The TPRC Data Series. Volume 10. Thermal Diffusivity, DTIC Document.

Vaca-Oyola, L., et al. (2016). "A liquids refractive index spectrometer." Sensors and Actuators B: Chemical.

3. Infrared thermal imaging based methods for thermal material characterization

Chapter 1 introduced the concept of thermal radiation, i.e. the electromagnetic radiation emitted by all bodies at a temperature above absolute zero. Later in that same chapter it was discussed how the wavelength and intensity of this radiation varies with temperature and how this leads to a family of PT techniques based on radiometry, i.e. measuring the radiative output of a body to determine and study its temperature.

This chapter utilizes a radiometric technique, namely IR thermography, to thermally characterize materials. Both time resolved and thermal wave techniques are used.

1. Introduction: IR Thermographic Cameras

Back in 1800 famous astronomer Sir William Herschel was working on an experiment where he used a prism to separate sun light into its spectral components (Herschel 1800). He placed thermometers at the different light colors and was interested in measuring the temperature rise. An additional thermometer was placed just next the red part of his projected spectra, where no color could be seen. The temperature on this thermometer began to rise, it became apparent that some sort of invisible part of the radiation spectra was transmitting heat to the thermometer, and so infrared radiation was discovered. Herschel was the first to fully comprehend that light and heat where in some way related (Herschel 1800).

A long time has passed since Herschel's experiment demonstrated IR radiation existed. Science has come to a greater understanding of the physical laws governing it. In chapter 1, Plank's law, Stefan-Boltzmann law and the Wien law of displacements were covered. These laws are very important for thermography since they are the principle that allows the formation of temperature images by measuring the radiative emission of a body.

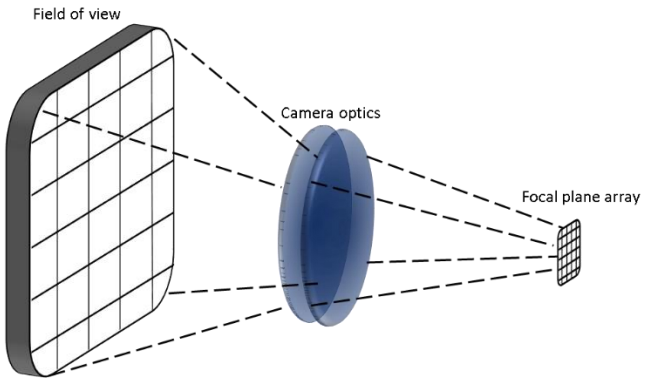

FIGURE 3-1 DEPICTION OF A FOCAL PLANE ARRAY IMAGING A FIELD OF VIEW. NO SCANNING IS NEEDED, THE WHOLE FIELD OF VIEW IS IMAGED AT ONCE

The modern implementation of thermography, as with many things, is digital. The images are formed in a similar fashion to other digital cameras, i.e., a set of lenses forms an image on a plane where an array of sensors is located. Each minute sensor reacts to the incident IR radiation and provides a voltage or current signal that is then digitized. This is achieved using a focal plane array (FPA), i.e. an image sensing device that consists of an array of EM radiation sensitive pixels. A FPA allows for an image of the desired field of view to be generated practically at the same time with the electronic reading of the sensor information being the limiting factor.

The image formed by an IR thermographic camera will be a representation of the intensity of emitted, transmitted and reflected radiation. This is an important thing to consider; experiments working with thermographic cameras must be able to limit or quantify the amount of reflected and transmitted radiation if anything useful is to be said about the emitted radiation.

$$I_{total} = I_{reflected} + I_{emitted} + I_{transmitted} \quad (3.1)$$

IR Camera Detectors

Detectors can be split into two broad categories: thermal and photonic. In this section, a brief review of the detector types is offered.

Thermal

These doctors work by producing a temperature difference in the detectors themselves through the absorption of IR radiation. The value measured will be directly related to a physical property within the detector that varies directly with temperature, some examples include: the pyroelectric detector, the bolometer thermistor and the thermopile among others. Some advantages are (Maldague 2012):

- Broad flat spectral response.
- No cooling required, however cooling can increase sensitivity.
- Reduced cost.
- No mechanical scanning.

Some disadvantages are:

- Some configurations require a chopping mechanism given that many sensor types are only sensitive to changes in radiation, e.g. pyroelectric target sensors. The chopper, be it mechanical or electronic, can induce image flickering which might require additional correction.
- Smaller range of observable temperature.
- Lower sensitivity and response time than photonic detectors.

Currently the most used thermal detectors are of the bolometric type where the temperature difference is inferred from the variation of the electrical resistance of the sensing element. Microbolometer arrays have been developed, these have allowed for a faster response time (between 30 and 60 Hz).

Photonic

In photonic detectors, the absorbed energy affects atomic states and free electrons within a semiconductor. When photons strike the sensing element, if they have enough energy, they can excite electrons and change their state. This process is only possible if the energy of each striking photon is larger than the energy gap needed for a change in quantum level.

The detectors can be of a photoconductor nature, where the resistivity of the semiconductor is affected (higher number of free electrons), or photovoltaic, where a voltage output is generated. Common materials used in photonic detectors include:

- Silicon (Si).
- Indium arsenide (InAs).
- Indium antimonide (InSb).
- Cadmium mercury telluride (HgCdTe or CMT).
- Quantum well infrared photodetector (QWIP).

CMT detectors can be operated as photoconductor or as photovoltaic devices and may be doped so that they may operate on a wide range of IR bands Operating temperatures range from 77K to 170K. Silicon detectors, usually used for sensing in the visible part of the spectrum, can be used for near infrared (NIR) sensor operating well up to around a wavelength of 1 μm.

InSb arrays can be operated as a photoconductor and photovoltaic as well, they are sensitive to radiation wavelength of around 3 μm to 5 μm. QWIP detectors are made up of alternating semiconductor layers with different energy gaps that give rise to quantum wells. A common material used is gallium arsenide layered with aluminum gallium arsenide. QWIP detectors can have their bandwidth tuned making them a promising development in many areas (Astarita and Carlomagno 2012, Maldague 2012).

Detector performance

Detection performance is related to the presence of noise and may limit the sensibility of the element. If the noise is high enough measurement may be made impossible, the noise of the detector depends on its temperature. The *noise equivalent power,* NEP (W), is the radiation input needed to give an output signal of the same magnitude as the noise.

While the NEP may be used to compare sensors performance a more useful tool is known as the normalized detectivity, D^*, which is defined as:

$$D^* = \frac{\sqrt{A_s \Delta f}}{NEP}\left(\frac{cm\sqrt{Hz}}{W}\right) \tag{3.2}$$

where A_s is the detector's surface area and Δf is the noise bandwidth. D^* is particularly useful for comparing different IR detectors since it measures the signal to noise ratio when one Watt of 1 Hz bandwidth radiation strikes on a 1 cm^2 detector(Gaussorgues 1994, Astarita and Carlomagno 2012). As an example, an InSb detector cooled at 77 K will have a detectability peak of $\sim 10^{11} cm\sqrt{Hz}/W$ at a wavelength of $\sim 5\mu m$ while a thermistor bolometer's is $\sim 20^8 cm\sqrt{Hz}/W$ with a practically wavelength independent response. The figure below shows the detectivity for different detectors.

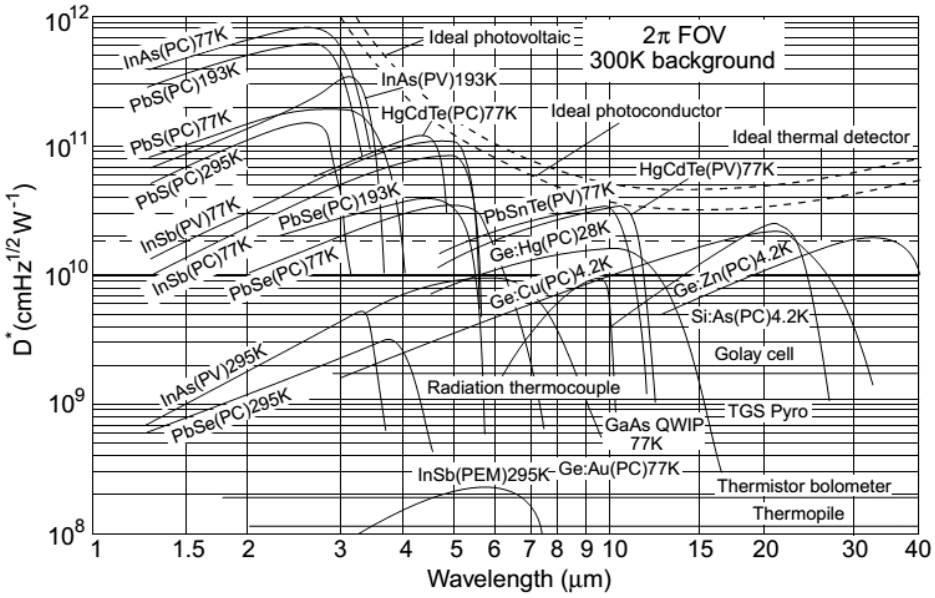

FIGURE 3-2. D^* FOR DIFFERENT DETECTORS(ROGALSKI 2003)

Cooling systems

Optimum performance of most IR detectors is only achievable at low, stable temperatures. Most of the time the cooling system and the detector will be integrated into the same device. Cooling methods include:

- Bulk.

- Thermoelectric.
- Stirling coolers.

Bulk cooling is carried out by using a Dewar flask filled with liquid nitrogen (LN), however, the requirement of constant replenishment of the LN has made this cooling method less common. The most used cooling method nowadays is Stirling cooling, miniaturized versions of the coolers have allowed for versatile devices to be created. More information on cooling systems can be found elsewhere (Gaussorgues 1994).

Sensor Resolution

In the context of thermographic sensors, we may speak of three resolution measures: spatial, thermal and temporal. The spatial resolution is the ability to resolve spatial differences in electromagnetic energy, this ability depends mostly on the size of the detecting elements (pixels). A smaller pixel size increases spatial resolution.

The temporal resolution of the system is related to the time response of the sensor. As previously mentioned, photonic sensors have faster response times than thermal sensor and can therefore achieve a higher temporal resolution.

Both spatial and temporal resolutions in IR imaging sensors are subject to the Nyquist-Shannon sampling theorem that states that the sampling frequency of the system, in this case temporal or spatial, should be at least twice the highest frequency of the sampled signal.

The thermal resolution of the sensors is best described by what is known as the noise equivalent temperature difference (NETD), it is a measure of the temperature of an object that generates a signal that is equal to the noise level (Breitenstein and Langenkamp 2003). The NETD gives us an idea of the smallest temperature difference detectable with a given sensor.

Atmospheric Windows

The atmosphere registers some intense IR radiation absorption in some wavelengths. This is important to consider in thermographic measurements, sensors working within the atmospheric absorption regions will not be very efficient. Most sensors are therefore designed to work in what are known as the *Atmospheric Windows*, these are regions in the IR spectrum that have a relatively good transmittance.

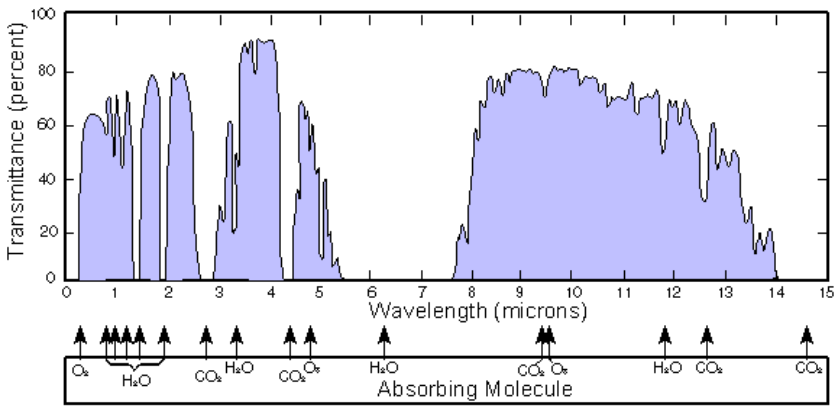

FIGURE 3-3 IR ATMOSPHERIC TRANSMITTANCE.

The regions are usually divided into the *Short*, *Mid* and *Long* infrared windows (SWIR, MWIR, LWIR) (Astarita and Carlomagno 2012):

- SIRW: 1 to 2.5 μm
- MIRW: 3 to 5.6 μm
- LIRW: 8 to 14 μm

Interest is mainly centered around the MWIR and LWIR given that in these wavelength regions a body at room temperature will radiate enough IR radiation to provide an accurate measurement (Rogalski 2003). SIRW detectors exist and are used for high temperature IR thermography or optical experimentation, as seen in the previous chapter.

Active and Passive Approaches

Thermographic setups may be categorized into two broad categories: passive and active. Passive thermography analyzes materials and structures which are naturally at a higher temperature than ambient. It is widely used in industrial environments to monitor production, maintenance, medicine, astronomy among others.

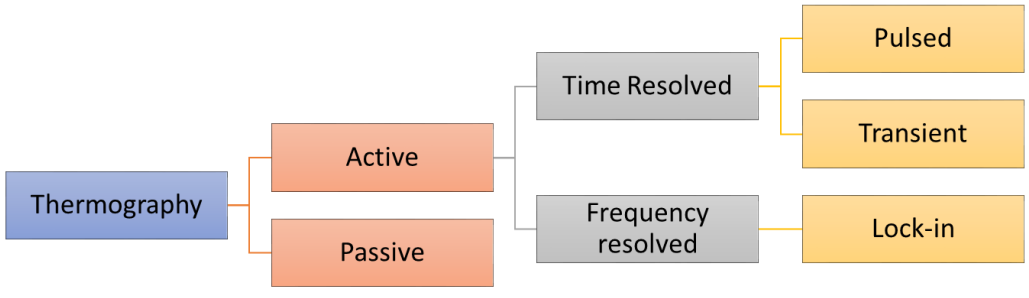

FIGURE 3-4 DIFFERENT THERMOGRAPHY DETECTION AND EXPERIMENTAL SCHEMES

In the active approach an external heat source must be used to excite the samples being investigated. This is the approach that is of interest in this work since it allows for the

investigation of photothermal techniques and the investigation of other heat diffusion phenomena. Different mechanisms exist for the generation of the external heat source, this work is interested in two. In this chapter heat generation via a light sourced will be used, both in a pulsed and frequency modulated scheme

Time Resolved

In the introductory chapter an overview of time resolved techniques for thermal characterization was given. These techniques, as mentioned earlier, rely on studying the temporal evolution of the temperature of a sample. Time resolved active IR thermography is the use of a thermographic camera to apply techniques such as flash or step-pulse excitation. The main advantage of these techniques is their speed, in some cases results can be obtained in a mater o seconds.

Pulsed Thermography

Pulsed thermography is one of the most popular techniques in IR thermography due to its quick measurements. A pulse with a duration of anywhere between the millisecond to second range is used to excite the specimen under study, the excitation time needed being a function of the material being studied, in general faster excitation times are needed for better conductors. The idea is that the heat pulse effectively behaves as an instant source of heat. The heating is usually brief enough to prevent any damage from heating (Maldague 2002).

Thermography has been successfully used in material thermal characterization in conjunction with the flash technique (Krapez, Spagnolo et al. 2004, Nagpure, Dinwiddie et al. 2010) as well as for defect detection and characterization (Sakagami and Kubo 2002, Sun 2006). The brief heating and in many instances cooling of the specimen is recorded on the IR camera for later processing.

The flash technique coupled with IR thermography is a subject of interest in this chapter. Further detail on the use of flash thermography for material thermal characterization will be given in the following sections.

Transient Thermography

Transient thermography refers to a set of experimental schemes where the heat source is applied to a sample that had previously been at thermal equilibrium with its environment. The pulse may be a long steady one, where the temperature rise on the sample is studied, or a single pulse of a given time, usually a square pulse, where both the temperature rise and temperature fall are of interest.

In step heating a stepped heat pulse, i.e. a long pulse, is applied to the specimen and the rise in temperature is monitored. The sample is continuously heated at low power. Variations of the surface temperature with respect to time are related to specimen parameters (thermal properties and defects).

Square wave heating has been used for thermal characterization and sizing of defects has also been shown utilizing transient heat sources (Saintey and Almond 1995, Ball and Almond 1998), an important application that has gained the interest of scientists and industry alike. The next chapter deals with the use of ultrasonic excitation to generate transient heat sources and will center on defect detection and geometrical quantification, more detail on this will be offered there.

Frequency Resolved

Frequency resolved techniques are those that study the evolution of the temperature on a sample in dependence of frequency related parameters. The study may involve the use of one or many frequencies and the analysis of the spatial behavior of the temperature. Thermal wave physics play an important role in these types of techniques (Maldague 2002) because they offer a framework so that results can be accurately analyzed.

Lock-in Thermography

Lock-in thermography studies the resulting oscillating temperature field in the stationary regime through lock-in amplification (see Chapter 1). In many applications, the photothermal effect is used to excite the sample but, as with time resolved techniques, different heat source generation techniques can be applied. A proper experimental apparatus will allow the experimenter to observe an amplitude image and a phase image of the resulting thermal wave on the sample under study.

The images obtained correspond to a mapping of the IR emission. An important feature of lock-in thermography is that the phase image is relatively independent of local optical surface features(Busse 1994), with thermal contrasts being the dominant parameter in generating the images.

In the case of photothermal lock-in thermography, different light sources may be used for the generation of the thermal waves. When flat illumination of a large surface is required modulable lamps are the usual choice, lasers can be used in both flat illumination and point illumination configurations.

The most important feature of Lock-in thermography is its ability to separate signal from noise. The noise amplitude, A_{noise}, in a digital lock-in measurement, as is the case for thermography, is given by (Breitenstein and Langenkamp 2003):

$$A_{noise} = \frac{2}{\sqrt{N}} NETD \qquad (3.3)$$

where N is the number of samples, i.e. frames, taken for a measurement. The NETD is the “noise equivalent temperature difference”. A value related to the NEP seen earlier, but evaluated for temperature instead of the radiative power. The NETD is calculated using the mean square of the deviation of different values measured for one pixel F_i, in *mK*, from its mean value $\bar{F}$ obtained in k successive measurements (Breitenstein and Langenkamp 2003).

$$NETD = \frac{1}{k}\sqrt{\sum_{i=1}^{k}(F_i - \bar{F})^2} \tag{3.4}$$

The NETD allows us to predict the average amplitude of the random noise level after a certain acquisition time at a given frame-rate. This is only valid for random white noise; other noise sources will not behave accordingly.

2. Simultaneous measurement of thermal diffusivity and effusivity of solids using the flash technique in the front-face configuration.

The front configuration flash technique was used at the photothermal laboratory in the UPV. A thermal interface created with a liquid backing allows for the simultaneous measurement of both thermal diffusivity and thermal diffusivity. This method is discussed in this chapter. The work done resulted in the publication of one article, this chapter is mainly based on said article.(Pech-May, Cifuentes et al. 2015)

Introduction

Thermal diffusivity (α) and thermal effusivity (ϵ) allow us to fully characterize the thermal transport properties of a material. (Marín 2007) Both are related to thermal conductivity (k) through the following relationship: $\epsilon = k/\sqrt{\alpha}$. The flash method is one of the most used techniques to measure thermal diffusivity. The traditional flash method involves heating an optically opaque plaque's front face using a short pulse and observing the temporal evolution of the temperature on the back face (Parker, Jenkins et al. 1961). In an alternative configuration, known as the front face variant (Balageas 1989), the temperature on the face being illuminated is observed. In this configuration only one of the faces needs to be available for measurement, this can be an advantage on many situation in which the back of the sample is inaccessible. The mathematical model for temperature T for the flash method, where L is the length of the plate, Q_0 is the χ is the fraction of the energy absorbed by the sample energy per unit area delivered by the pulse, is as follows:

$$T(0) = \frac{Q_0 \chi}{\epsilon} \frac{\sqrt{\alpha}}{L} \left[1 + 2 \sum_{n=1}^{\infty} e^{-\frac{n^2 \pi^2}{L^2} \alpha t} \right] \tag{3.5}$$

$$T(L) = \frac{Q_0 \chi}{\epsilon} \frac{\sqrt{\alpha}}{L} \left[1 + 2 \sum_{n=1}^{\infty} (-1)^n e^{-\frac{n^2 \pi^2}{L^2} \alpha t} \right] \tag{3.6}$$

Although both the effusivity and diffusivity appear in the model, the effusivity is correlated with the fraction of the energy absorbed by the plate making it difficult to determine accurately. This means that freestanding plates can only have their diffusivity measured.

By putting the rear surface in contact with a fluid backing the temperature on the front surface becomes sensitive to the thermal mismatch. This can be performed both in a modulated scheme (Depriester, Hus et al. 2005) or using time resolved techniques such as flash (Pech-May, Cifuentes et al. 2015). However, the modulated variant is time consuming since the frequency scan required must be performed twice, one with the sample backed by a fluid and one with the bare sample.

Objectives

- Utilize the thermal coupling of a fluid with a solid to determine the solid's thermal diffusivity and effusivity simultaneously by studying the temperature on the sample's front surface.
- Evaluate the technique with different backing fluids and sample materials to better understand its limitations.

Theory

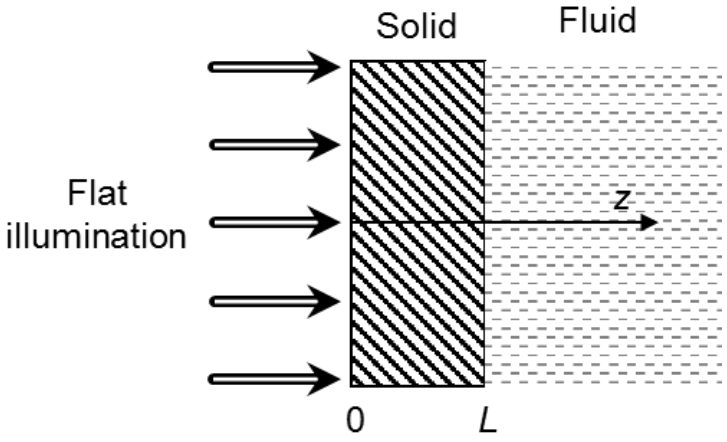

FIGURE 3-5 PROBLEM GEOMETRY

A two-layer model, where the solid slab is optically opaque and of thickness *L* and where the liquid backing is semi-infinite is considered (Figure 3-5). Let L be the sample thickness. The Laplace transform of the temperature rise, $\bar{T}$, is:

$$\bar{T}_s = Ae^{q_s z} + Be^{-q_s z} \tag{3.7}$$

$$\bar{T}_f = Ce^{-q_f (z-L)} \tag{3.8}$$

where $q = \sqrt{s/\alpha}$, s beign the Laplace variable. Subscripts s and f correspond to sample and fluid respectively. With the following boundary conditions, constants A, B and C may be found conditions (Pech-May, Cifuentes et al. 2015):

$$k_s \left.\frac{d\bar{T}_s}{dz}\right|_{z=0} = h\bar{T}_s(z=0) - \bar{I}_0\chi \tag{3.9}$$

$$\bar{T}_s(z=L) = \bar{T}_f(z=L) \tag{3.10}$$

$$k_s \left.\frac{d\bar{T}_s}{dz}\right|_{z=L} = k_f \left.\frac{d\bar{T}_f}{dz}\right|_{z=L} \tag{3.11}$$

The Laplace transform for the temperature rise at the plaque's surface:

$$\bar{T}_s(0) = \frac{\bar{P}_0 \chi}{\epsilon_s \sqrt{s}} \frac{\cosh q_s L + \frac{\epsilon_f}{\epsilon_s} \sinh q_s L}{\left(\frac{\epsilon_f}{\epsilon_s} + \frac{h}{\epsilon_s \sqrt{s}}\right) \cosh q_s L + \left(1 + \frac{h}{\epsilon_s \sqrt{s}} \frac{\epsilon_f}{\epsilon_s}\right) \sinh q_s L} \qquad (3.12)$$

$\bar{P}_o$ is the Laplace transform of the temporal shape of the light beam and *h* is the linear coefficient of heat transfer, which considers the combined effect of heat convection and radiation. In the ideal case of the pulse being a Dirac delta function the power distribution is $P_o(t) = Q_o \delta(t)$, with its Laplace transform being $\bar{P}_0 = Q_0$. In the case of a laser pulse following an exponential law of the form $P_o(t) = \frac{Q_o}{N} \frac{t^\alpha}{\tau^{1+\alpha}} e^{-t/\tau}$, with parameters ξ and τ depending on the laser used and N as a normalization constant such that the condition $\int P(t)dt = Q_o$ can be met, the Laplace transform is $\bar{P}_o = \frac{Q_o}{(1+s\tau)^{1+\xi}}$.

The inverse Laplace transform for equation 3.12 allows us to obtain the temporal evolution of the surface temperature after absorbing a laser pulse. No analytical solution can be given, however, the Stehfest algorithm allows for a numerical solution (Stehfest 1970, Abate and Whitt 2006) which can then be utilized for a multiparametric fitting.

For semi-infinite samples, the evolution of the *log-log* plot between the temperature and time will give a straight line with a slope of -0.5. For thinner plates, further analysis of the model shows that the backing interface effects are seen at the surface temperature at $t_1 = L^2/(\pi D_s)$. The interface effects when plotted show a displacement of the -0.5 slope curve. This displacement is related to the ratio of thermal effusivities between the sample and the backing. Air backing does not allow for the retrieval of the ratio of thermal effusivities since this displacement never comes, this is due to the large difference between the effusivity of air and that of the sample. Figure 3-6 shows the results of said simulation as published in our recent article. (Pech-May, Cifuentes et al. 2015)

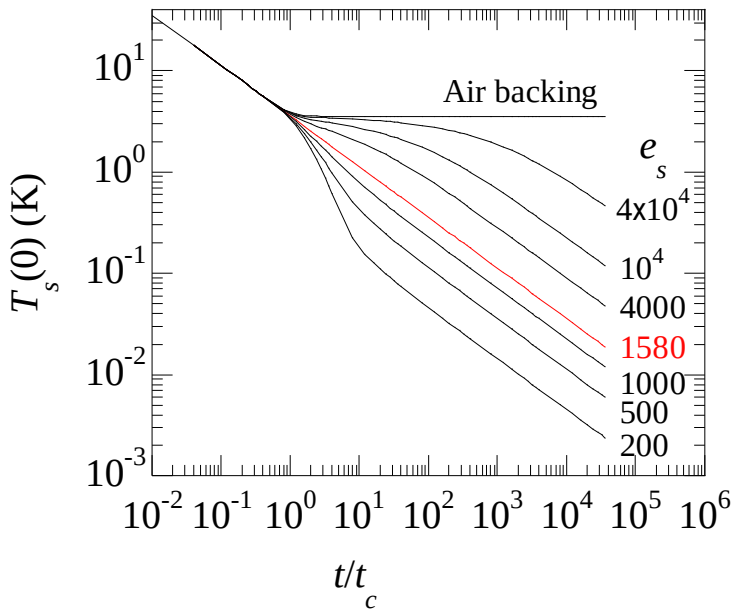

FIGURE 3-6 (PECH-MAY, CIFUENTES ET AL. 2015) SIMULATION OF THE SURFACE TEMPERATURE EVOLUTION AS A FUNCTION OF DIMENSIONLESS TIME FOR AN OPAQUE SLAB ON TOP OF WATER ($\epsilon = 1580\ Ws^{0.5}\ m^{-2}K^{-1}$) AFTER RECEIVING A BRIEF LASER PULSE ($\frac{Q_0\chi}{e_s} = 1$). IDEAL CONDITIONS ARE CONSIDERED: H =τ= 0. DIFFERENT VALUES OF THE SOLID EFFUSIVITY ARE EVALUATED. A SIMULATION FOR AIR BACKING (ϵ = 5.5 $Ws^{0.5}M^{-2}K^{-1}$) IS ALSO PLOTTED FOR COMPARISON. (PECH-MAY, CIFUENTES ET AL. 2015)

Experimental Setup

The sample to be measured is normally coated with a thin graphite layer a few microns thick. It is than attached to a fluid container box where it acts as part of a wall. A Nd:Glass laser, manufactured by Quantel, working at a wavelength of 1,053 nm and with a "flat-top" spatial profile was used as the lighting source. The pulsed laser can deliver up to 25 joules per pulse with the pulse length being $< 600\ \mu s$. The beam is redirected to the sample surface using a golden coated mirror and is passed through a holographic diffuser to guarantee homogeneous illumination.

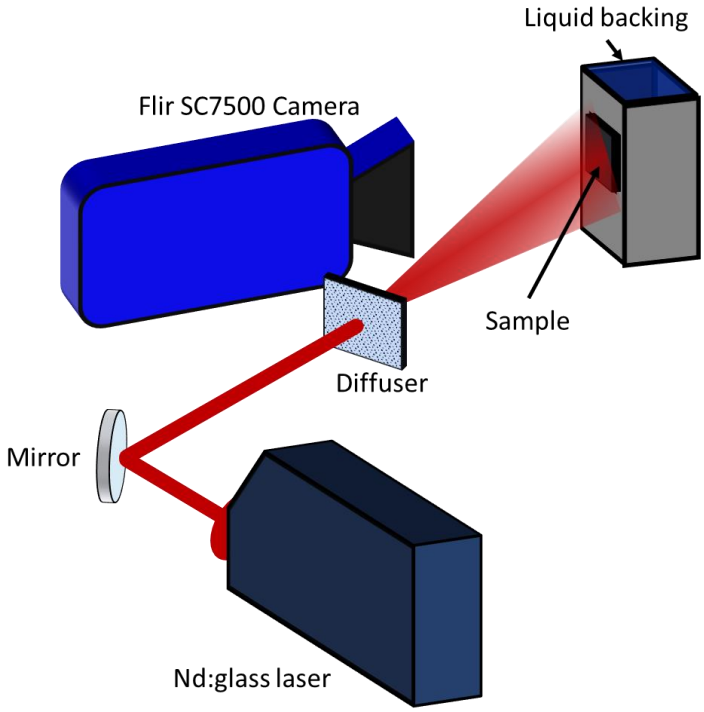

FIGURE 3-7 FRONT FACE FLASH EXPERIMENTAL SET-UP

IR radiation is emitted by the sample and captured by a FLIR SC7500 IR camera with an InSb FPA Stirling cooled FPA sensor. The frame rates used for capture vary between 1 to 3.5 kHz. The IR camera can visualize the entire surface of the sample, instead of using a single pixel the average temporal evolution of thousands of pixels within the sample is obtained. This allows the noise level for the measurement to be substantially lowered, reaching levels of 3 to 5 mK when the noise floor for a single pixel is 20 mK.

Sample thickness must be carefully selected so that timing is right to obtain the thermal properties; if a plate that is too thick the effect of the interface between the liquid and the sample will be visible after a long time, this translates into a lower temperature at the time of measurement and it might be lost in the noise. If the plate is too thin, the interface's effect will occur at a very short time, making accurate measurements complicated due to hardware limitations (camera frame rate and laser pulse duration). In our experimental setup ten samples with known thermal properties were measured and their sample thickness was selected so that the effects of the thermal interface are observed at approximately 0.1 s.

Results and Discussion

Figure 3-8 shows the experimental results for measurements with four different samples, two metallic and two polymeric. The metallic samples were measured using a water backing while

with the polymeric ones both water and ethanol were used. Continuous lines show the best fit to the theory while dots show the experimental measurement.

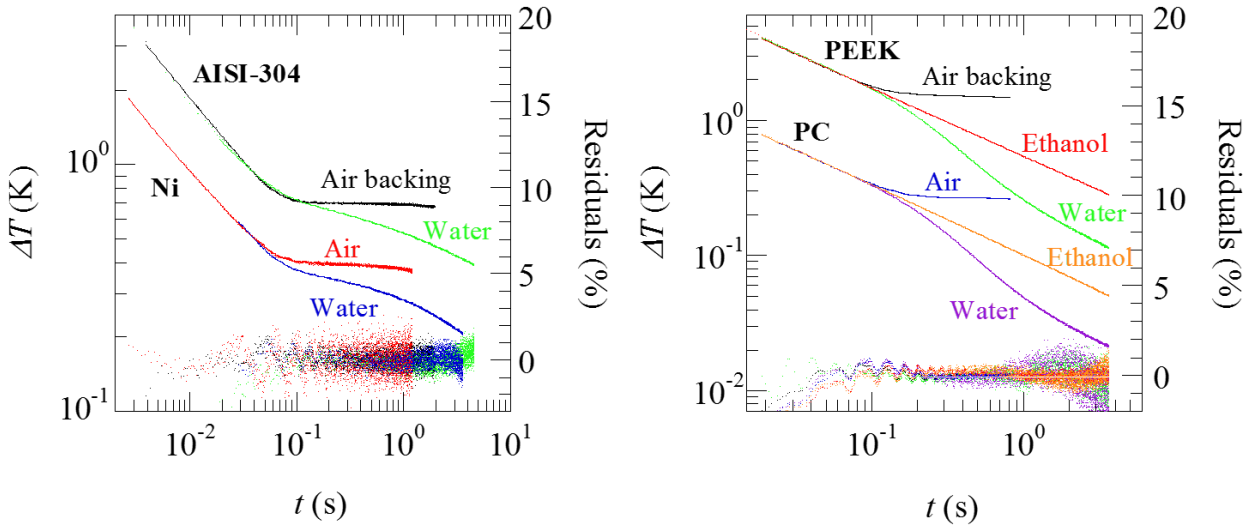

FIGURE 3-8 (PECH-MAY, CIFUENTES ET AL. 2015) TEMPERATURE RISE ABOVE THE AMBIENT AS A FUNCTION OF TIME AFTER THE HEATING PULSE FOR DIFFERENT MATERIALS. DOTS ARE THE EXPERIMENTAL DATA AND CONTINUOUS LINES THE FITTING TO THE THEORY. TEMPERATURE DATA FOR NI AND PC ARE SHIFTED. (A) METALLIC SAMPLES. (B) POLYMERS. POLYMERIC SAMPLES WERE MEASURED WITH THREE BACKINGS: AIR, WATER AND ETHANOL, WHEREAS METALLIC SAMPLES WITH AIR AND WATER BACKINGS. RESIDUALS ARE ALSO PLOTTED TO VISUALIZE THE QUALITY OF THE FITS.

Table 3-1 shows us the results for the measured samples. Thermal diffusivity can be accurately measured in all cases, however the recovery of thermal effusivity is more complicated. For samples with a thermal effusivity close to that of the backing the result is in good agreement with the reported literature, however samples having an effusivity three times larger than the backing begin to differ significantly. This can be understood through sensitivity analysis and simulation (Pech-May, Cifuentes et al. 2015), where it can be seen that the sensitivity to the effusivity of the sample arrives at longer times as the effusivity mismatch is increased (i.e. $e_s \gg e_b$), making the measurement unreliable as the temperature of the surface has cooled down to noise levels.

TABLE 3-1 RESULTS (PECH-MAY, CIFUENTES ET AL. 2015)

Material	L (mm)	α_s Air backing (mm^2s^{-1})	α_s Water backing (mm^2s^{-1})	α_s Literature[a] (mm^2s^{-1})	ϵ_s Water backing ($Ws^{0.5}m^{-2}K^{-1}$)	ϵ_s Literature[a] ($Ws^{0.5}m^{-2}K^{-1}$)
Cu	3.248	107	120	117	9100	37140
Ni	2.065	21	21	23.0	12000	18910
Zn	3.116	42	44	41.8	9800	17942

Alumina	1.035	8.4	8.6	7.6-10.3	8600	9430-10900
AISI-304	0.897	3.8	4.1	3.95	6800	7498
Pb	2.176	23	24	24.1	6800	7190
Bi	1.040	6.0	6.1	6.55	3000	3050
Glassy carbon	1.088	6.6	6.6	6.2	2300	2530
PEEK	0.259	0.17	0.18	0.145	640	655
PC	0.261	0.14	0.15	0.13-0.15	550	523-563

Conclusions

The flash method in its front face variant was experimentally shown to be capable of retrieving both thermal diffusivity and effusivity if a fluid backing is used. The limitations of the method have also been explored. It was observed that when fluid backing effusivity is three times less than sample effusivity sensitivity to this last variable is lost with our measuring capabilities. This drawback could be overcome by using a liquid metal alloy backing, e.g. a gallium indium tin alloy, so that the effusivity mismatch is within measuring range.

This method offers a fast-non-destructive way to fully thermally characterize a given sample given that the proper experimental conditions can be met.

3. Study of the Thermal Properties of Polyester Composites Loaded with Oriented Carbon Nanofibers using the Front-Face Flash Method

A set of polyester-resin-based samples synthesized by a team at the Department of Applied Physics at CINVESTAV Mérida were studied to determine their thermal properties. These samples were loaded with carbon nanofibers (CNF) decorated with magnetite nanoparticles (m-CNF). Nanofiber volumetric concentration ranged from 0 to 3.25%. The fibers are found in oriented and non-oriented configurations. The orientation is achieved by submitting the samples to a constant magnetic field during synthesis.

The thermal properties of the samples were determined using the front-face flash method. This work has been published and the information shown herein is heavily based on said publication (Pech-May, Vales-Pinzón et al. 2016).

Introduction

The improvement of the thermal conductivity of polyester composites is a subject of great interest in multiple areas, e.g. aerospace industry. It has been reported that a CNF filler content of 2% in weight can enhance thermal conductivity up to 115% of the original value(Huang, Liu et al. 2005). Alignment of the CNFs tends to prove difficult via magnetic fields due to the low magnetic momentum of the CNF. For this reason nanoparticles of iron were attached to the fibers (*m-CNF*) and this lowered the magnetic field intensity requisites for the field intensity (Pech-May, Vales-Pinzón et al. 2016). Orientation of the filler in the polymeric matrix has a strong influence in the effective thermal properties of the composite. For this reason, two sets of samples were synthesized, one with aligned m-CNFs and another without alignment.

To measure the thermal diffusivity (α) and effusivity (ϵ) of the samples the flash technique in its front faced configuration was used. As previously seen, flash is a non-contact non-destructive technique which allows the study of the thermal properties without altering the samples. As explained in the previous section and in Chapter 1, in this method the sample's surface is heated by a short luminous pulse and the surface's temperature is recorded.

Objectives

- Use the front face flash technique to study the variation in thermal diffusivity and conductivity in polymer samples loaded with aligned and non-aligned m-CNFs

Theoretical Background

The front-face flash model was explored in the previous section. The same model seen in the previous section applies, however, in this case air would be the backing material. Instead of determining the thermal effusivity (ϵ) by using a fluid backing its value is to be obtained by the relative variations seen between samples of different *m-CNF* concentration and orientation against their matrix. This provides us with further simplification given that air's thermal effusivity is much smaller than that of most materials.

$$\bar{T}(s) = \frac{Q}{\epsilon} \frac{\sqrt{s} + h' \tanh\left(x\sqrt{s}\right)}{2h'\sqrt{s} + (s + h'^2)\tanh\left(x\sqrt{s}\right)'} \tag{3.13}$$

where s is the Laplace variable, α the thermal diffusivity, $x = L/\sqrt{\alpha}$ and $h' = \frac{h}{\epsilon}$. h is the heat transfer coefficient which considers the heat losses from both surfaces to the surroundings due to convective and radiation effects.

Q is the Laplace transform of the temporal shape of the light pulse. In the case of a "step" shaped pulse lasting τ seconds $Q = \frac{P_0(1-e^{-s\tau})}{s}$, where P_0 represents the power per unit area of said pulse. The inverse Laplace transform of the equation above can be obtained numerically through the Stehfest algorithm (Stehfest 1970).

Figure 3-9 shows a numerical simulation result from our published work (Pech-May, Vales-Pinzón et al. 2016). On the left side, we can see the model's behavior for two samples with the same thermal effusivity but different diffusivity. On the right, we have the opposite case in which the diffusivity is equal but the effusivity has changed. These plots illustrate how the two parameters that are to be determined affect the result, while variations on the thermal diffusivity become apparent on the behavior at the end of the plot (when the heat reaches the backside) the variation in thermal effusivity creates an offset between the two plots.

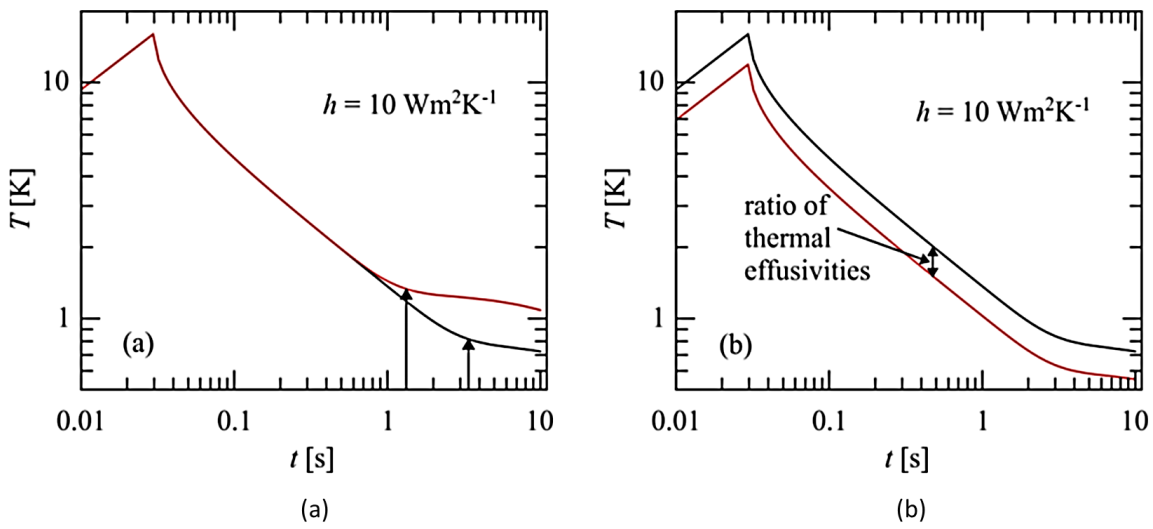

FIGURE 3-9 (PECH-MAY, VALES-PINZÓN ET AL. 2016) NUMERICAL SIMULATION RESULTS OF THE TEMPORAL TEMPERATURE EVOLUTION ON THE FRONT FACE OF A SAMPLE UTILIZING A $30\ ms$ LIGHT PULSE HERE $h = 10\frac{W}{m^2K}$, $L = 1.0\ mm$ AND $P_0 = 5\ W/cm^2$ (a) TWO MATERIALS WITH THE SAME THERMAL EFFUSIVITY $e = 580\frac{W\sqrt{s}}{m^2K}$ BUT DIFFERENT DIFFUSIVITY, $D_{black} = 0.11\ mm^2/s$ AND $D_{red} = 0.28\ mm^2/s$. (B) TWO MATERIALS WITH THE SAME THERMAL DIFFUSIVITY $D = 0.11\ mm^2/s$ BUT DIFFERENT THERMAL EFFUSIVITY, $e_{black} = 580\frac{W\sqrt{s}}{m^2K}$ AND $e_{red} = 780\frac{W\sqrt{s}}{m^2K}$.

Experimental Setup

Since no backing other than air is being used for this experiment we must be able to assure that each individual sample receives the same amount of power so that that the relative change in thermal effusivity can be measured. Once the relative thermal effusivity is obtained we can use the effusivity of the polymer resin matrix to calculate the absolute values for the rest of the samples. This means that procedure requires that the measuring conditions, especially laser power output, remain the same between measurements. To guarantee this a highly stable continuous wave 808-nm flat-top diode laser with adjustable power was used as the lighting source.

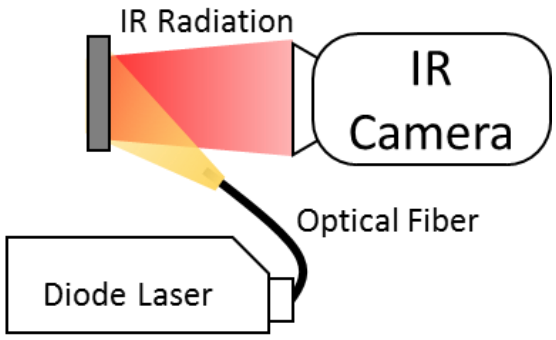

FIGURE 3-10 EXPERIMENTAL SETUP

Each sample is carefully placed on the same platform for measurement, where they are expected to receive the same power output from the laser. To assure that optical absorption across the samples remains constant as well a thin layer of graphite paint is applied.

The recording device for this experiment was a FLIR SC7500 IR camera. Images were taking using a frame rate of 200 Hz. For each measurement over 7200 pixels were averaged from the thermograms recorded by the camera effectively drawing the noise level under 5 mK.

Results and Discussion

Figure 3-11 shows a typical experimental result, here the temperature evolution and best fit to the model from a measurement of the polyester resin matrix, a 3.25 *m-CNF* non-aligned sample and a 3.25% *m-CNF* aligned sample are shown. The multi-parametric model fitting was done using the Levenberg–Marquardt algorithm, commonly used for non-linear least squares problems. The effects of adding *m-CNF* and the effects of their alignment become apparent even before analyzing or fitting the data.

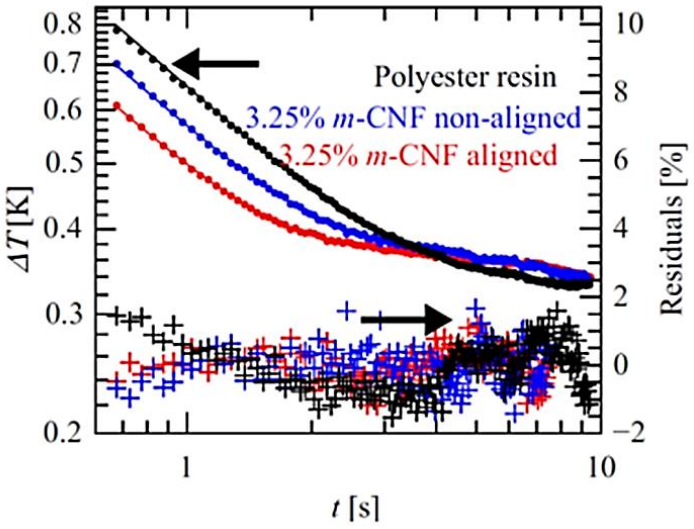

FIGURE 3-11 TYPICAL EXPERIMENTAL RESULT FOR THREE DIFFERENT MATERIALS. SOLID BULLETS SHOW EXPERIMENTAL DATA, SOLID LINES SHOW BEST FIT TO THE MODEL AND "+" SHOW THE RESIDUALS OF SAID FIT.

Figure 3-12 shows the diffusivity (a) and effusivity (b) measurements vs. the *m-CNF* concentration per weight. Although the error bars might overlap at lower concentrations, the effect of the fiber orientation becomes obvious as the concentration increases.

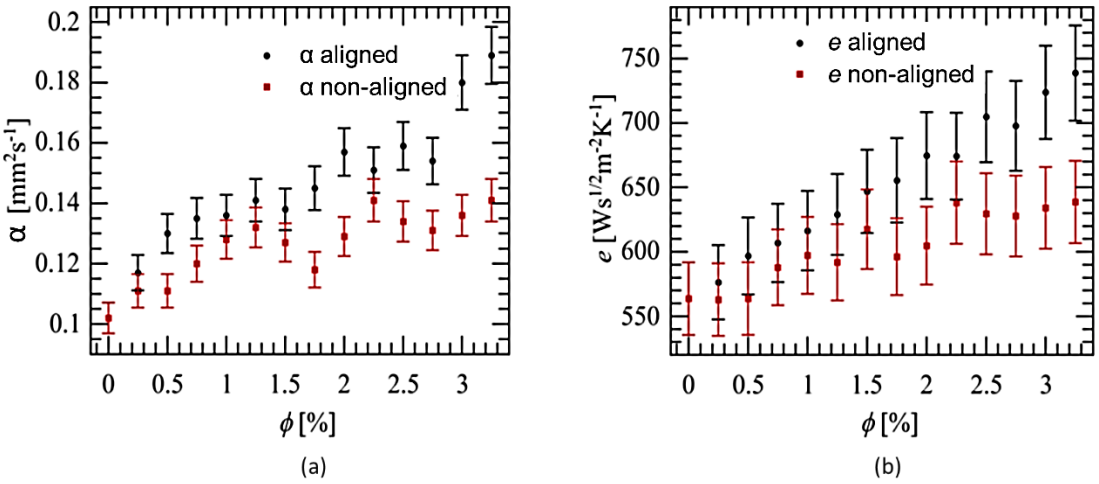

FIGURE 3-12 (PECH-MAY, VALES-PINZÓN ET AL. 2016) THERMAL DIFFUSIVITY (A) AND EFFUSIVITY (B) MEASUREMENTS IN DEPENDENCE OF THE M-CNF CONCENTRATION PER WEIGHT.

From the thermal effusivity and diffusivity the thermal conductivity, *k*, can be obtained ($k = e\sqrt{D}$). Figure 3-13 shows thermal conductivity as a function of *m-CNF* concentration. Note that while the non-aligned samples' conductivity seems to stall after a concentration of 1.5% aligned samples' conductivity continues to increase in what would almost appear a linear manner.

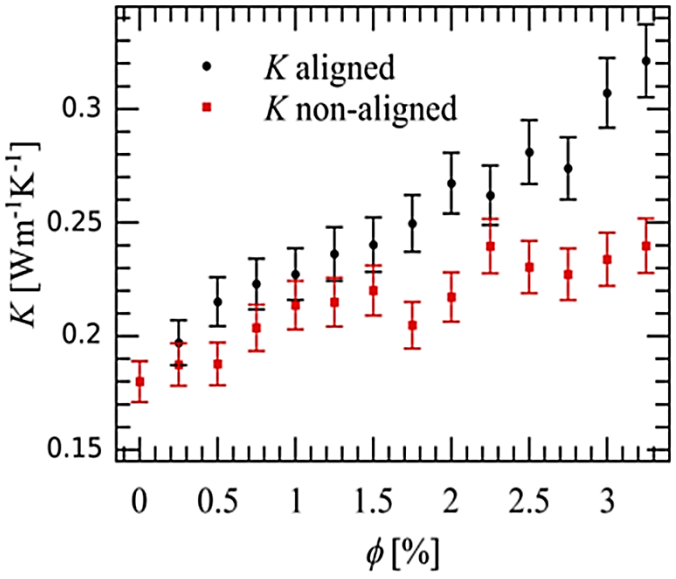

FIGURE 3-13 (PECH-MAY, VALES-PINZÓN ET AL. 2016)THERMAL CONDUCTIVITY (K) AS A FUNCTION OF M-CNF CONCENTRATION PER WEIGHT

Conclusion

This work has shown that the flash technique in its front face configuration can be used to measure both thermal effusivity and diffusivity albeit effusivity requires a more stringent

experimental procedure to achieve good results, this might not always be possible with all sample types, however it offers a good system of comparison on a set of similar samples which have a controlled and small variation in their composition.

We have also observed the importance of the effect of alignment and concentration of the m-CNF in thermal conductivity, effusivity and diffusivity. A more thorough analysis of this dependence can be found in our published work. (Pech-May, Vales-Pinzón et al. 2016)

4. Simultaneous measurements of the thermal diffusivity and conductivity of thermal insulators using lock-in IR thermography

Introduction

The knowledge of the thermal diffusivity (α) and thermal conductivity (k) allows for the full characterization of the thermal transport properties of a material (Salazar 2003, Marín 2007). Steady-state methods have traditionally been used to measure thermal conductivity while dynamic or transient methods are particularly sensitive to the coupling of α and k.

Lock-in IR thermography is a dynamic characterization method that consists in illuminating the sample with an intensity modulated light beam and recording the oscillating component of the temperature rise, i.e. the thermal waves, using an IR camera.

Using a tightly focused laser beam on the sample and recording the thermal wave phase or amplitude as a function of the radial distance to the laser spot the thermal diffusivity can be recovered by the slope method (see Chapter 1).

Salazar et al. have recently shown that conduction of thermal energy to the surrounding air modifies the temperature in the solid voiding the slope method. This effect was shown to be especially significant in the case of thin plates, thermal insulators and for low modulation frequencies (Salazar, Mendioroz et al. 2009). A workaround for this effect is to evacuate the surrounding air using a vacuum chamber (Mendioroz, Fuente-Dacal et al. 2009).

Obtaining the thermal conductivity through IR thermography is a more challenging task, when conduction to the gas is ignored, as in most simplified models, the conductivity appears coupled to the laser power absorbed by the sample (Jackson, Amer et al. 1981):

$$T_{max} \propto \frac{\eta P_0}{k} \tag{3.14}$$

where P_0 is the laser power and η is the fraction that is absorbed by the sample. The problem lies in determining η accurately, any light dispersion or scattering from the surface will introduce a significant uncertainty.

In the previous two sections, we discussed methods for measuring the thermal effusivity of a range of materials. These methods involved a backing fluid in contact with the material being measured. Following this idea, here the effect on the sample temperature of the thermal conduction to the air is used to obtain both α and k simultaneously. Using air holds several advantages for materials whose structure may be altered due to the presence of a fluid or the evacuation of air in a vacuum chamber, e.g. porous insulators or fibrous media.

Techniques to measure α and k simultaneously do exist, e.g. the commercially available Hot Disk method. This technique is a transient plane source method for the simultaneous measurement of thermal conductivity and diffusivity (He 2005). It measures the through thickness thermal transport properties. This contact method, however, has recently raised some doubts when applied to good thermal insulators (Coquard, Coment et al. 2013).

Objectives

- Develop and test a non-contact technique capable of determining the thermal diffusivity of thermal insulators.
- The technique should be able to determine the in-plane thermal transport properties, a measurement of interest given that it is seldom measured in other techniques capable of working with thermal insulators.

Theory

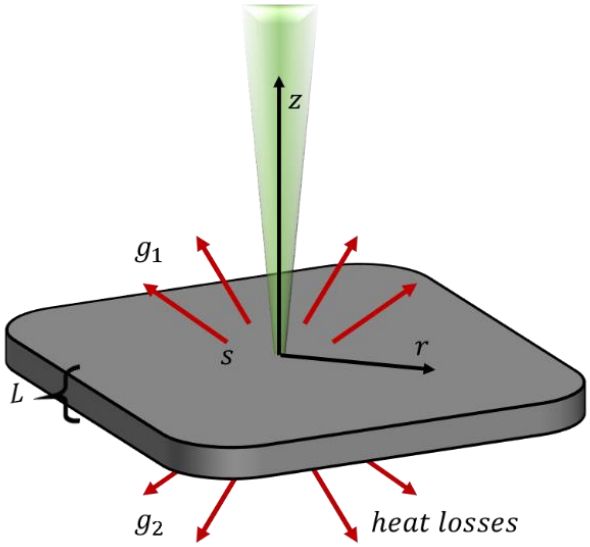

FIGURE 3-14 PROBLEM GEOMETRY

Let us consider an opaque and infinite slab of thickness *L*, illuminated by a focused laser beam of power P_o with a Gaussian profile of radius *a* (at $1/e^2$) and modulated at a frequency f ($\omega = 2\pi f$). The sample is surrounded by air. The geometry of the problem is shown in Figure 3-14. In what follows subscripts *s*, g_1 and g_2 stand for sample, gas at the illuminated surface and gas at the rear surface, respectively. Due to the cylindrical symmetry, the oscillating component of the temperature in each medium can be written in the Hankel space as:

$$T_{g1}(r,z) = \int_0^\infty \delta J_0(\delta r) A e^{-\beta_g z}\, d\delta \qquad (3.15)$$

$$T_s(r,z) = \int_0^\infty \delta J_0(\delta r)[Be^{\beta_s z} + Ce^{-\beta_s z}]\, d\delta \tag{3.16}$$

$$T_{g2}(r,z) = \int_0^\infty \delta J_0(\delta r) E e^{-\beta_g (z+L)}\, d\delta \tag{3.17}$$

where J_0 is the Bessel function of the zero order and $\beta_i^2 = \delta^2 + {}^{i\omega}/_{\alpha_i}$, $i = g, s$. *A, B, C* and *E* are obtained from the boundary conditions:

$$T_{g1}(z=0) = T_s(z=0) \tag{3.18}$$

$$T_{g2}(z=-L) = T_s(z=-L) \tag{3.19}$$

$$-k_s \left.\frac{\partial T_s}{\partial z}\right|_{z=0} = -k_g \left.\frac{\partial T_{g1}}{\partial z}\right|_{z=0} + hT_s|_{z=0} - \frac{\eta P_0}{2\pi}\int_0^\infty \delta J_0(\delta r) e^{\frac{(-\delta a)^2}{8}} d\delta \tag{3.20}$$

$$-k_s \left.\frac{\partial T_s}{\partial z}\right|_{z=-L} = -k_g \left.\frac{\partial T_{g2}}{\partial z}\right|_{z=-L} + hT_s|_{z=0} \tag{3.21}$$

where *h* is the combined radiation and convection heat transfer coefficient, for which we assume the same value at both surfaces. As the surface temperature rise is small the heat rate dissipated from the surfaces can be regarded as a linear function of the temperature. The last term in equation 3.20 is the Hankel transform of the heating power distribution of a Gaussian laser beam $\eta(P_o / \pi a^2)e^{-2r^2/a^2}$, where η is the fraction of the laser power absorbed by the sample.

By substituting equations 3.15 through 3.17 in equations 3.18 through 3.21 the four constants can be determined and the temperature for the sample is:

$$T_s(r,z) = \frac{\eta P_0}{4\pi}\int_0^\infty \delta J_0(\delta r) e^{\frac{(-\delta a)^2}{8}} \frac{\xi_1 e^{\beta_s(L+z)} + \xi_2 e^{-\beta_s(L+z)}}{\xi_1^2 e^{\beta_s L} - \xi_2^2 e^{-\beta_s L}} d\delta \tag{3.22}$$

$$\xi_1 = k_s\beta_s + k_g\beta_g + h \tag{3.23}$$

$$\xi_2 = k_s\beta_s - k_g\beta_g - h \tag{3.24}$$

A quick analysis for good thermal conductors can be done by assuming that $k_s \gg k_g$ and avoiding very low modulation frequencies ($f > 1Hz$) so that $k_s\beta_s \gg k_g\beta_g$ and $h \ll k_s\beta_s$. Equation 3.22 reduces to:

$$T_s(r,z) \approx \frac{\eta P_0}{4\pi k_s}\int_0^\infty \frac{\delta J_0(\delta r) e^{\frac{(-\delta a)^2}{8}}}{\beta_s} \frac{e^{\beta_s(L+z)} + e^{-\beta_s(L+z)}}{e^{\beta_s L} - e^{-\beta_s L}}\, d\delta \tag{3.25}$$

where it can be clearly seen that the thermal conductivity of the sample is now only correlated to the light power absorbed by the sample, as previously mentioned, and a precise measurement is hindered. The thermal diffusivity remains easily obtainable.

Now, for poor thermal conductors, the radial temperature will depend on both k_s and α_s and both parameters can be obtained using a multiparametric fitting of either the front or rear surface temperature.

Simulations

Numerical simulations were performed using equation 3.22 using as fixed parameters a = 0.2 mm, $f = 10\,mHz$, $h = 15\,{}^{W}/_{m^2K}$, $K_g = 0.025\,{}^{W}/_{mK}$ and $\alpha_g = 21\,{}^{mm^2}/_{s}$, the room thermal properties of air (Cengel 2003). Figure 3-15 shows the radial behavior of the natural logarithm of the front surface ($z = 0$) temperature amplitude multiplied by r, $Ln(r|T|)$, and the phase, Ψ, for a thermally very thick sample ($e^{-\beta_s L} \approx 0$).

Simulations performed for good thermal conductors are shown in Figure 3-15a. Black lines correspond to K = 20 $Wm^{-1}K^{-1}$ and D = 20 mm^2/s, red lines to K = 10 $Wm^{-1}K^{-1}$ and D = 20 mm^2/s, blue lines to K = 20 $Wm^{-1}K^{-1}$ and D = 10 mm^2/s and green lines to K = 10 $Wm^{-1}K^{-1}$ and D = 10 mm^2/s. As can be observed, for a given couple (k, α), both $Ln(r|T|)$ and Ψ are parallel straight lines whose slopes are related to the thermal diffusivity of the sample through the expression: $m_\Psi = m_{\ln r|T|} = -\sqrt{\frac{\pi f}{\alpha}}$. Note that changes in k do not modify the slopes of the straight lines in amplitude and phase; they produce a mere vertical shift in $Ln(r|T|)$, due to the correlation between ηP_o and k.

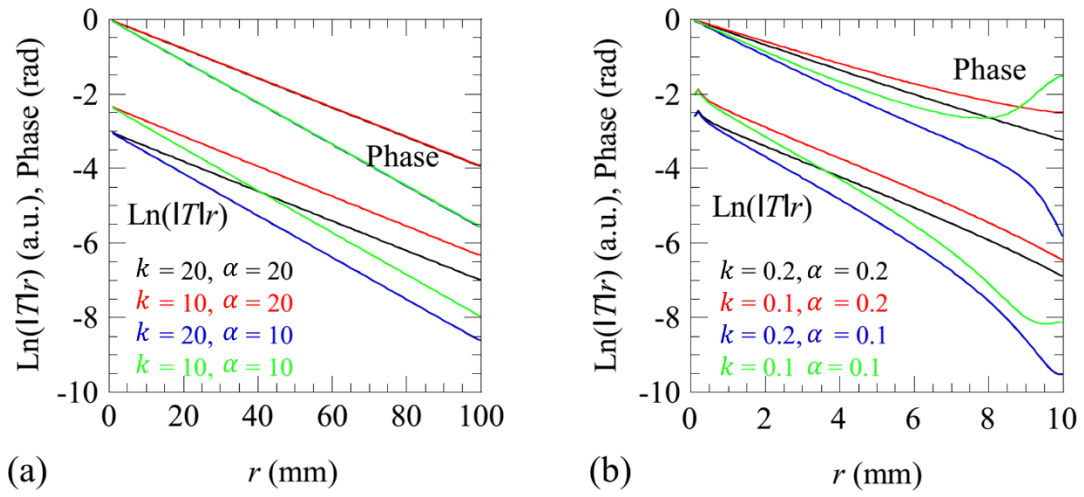

FIGURE 3-15 NUMERICAL SIMULATIONS OF THE FRONT SURFACE TEMPERATURE ($Ln(r|T|)$ AND Ψ) OF A THERMALLY VERY THICK SAMPLE USING THE FOLLOWING FIXED PARAMETERS A = 0.2 MM, F = 0.01 HZ, H = 15 $WM^{-2}K^{-1}$, K_G = 0.025 $WM^{-1}K^{-1}$ AND α_g = 12 MM^2/S. (A) GOOD THERMAL CONDUCTORS AND (B)

THERMAL INSULATORS. THE UNITS OF THERMAL CONDUCTIVITY AND DIFFUSIVITY OF THE SAMPLE ARE $Wm^{-1}K^{-1}$ AND mm^2/s RESPECTIVELY.

Figure 3-15b shows the simulation results for poor thermal conductors, here k and α are 100 times smaller with respect to those seen in Figure 3-15a. It can be easily seen that the linearity previously seen is no more. Furthermore, the curves change with both α and k, not just α, this is indicative of a sensitivity to both parameters.

Now, if the in-plane thermal transport properties are to be determined, the sample should be thermally thin. The same simulation but for a sample with a 2 mm thickness was carried out. Figure 3-16 shows the simulation results for the back surface of the sample.

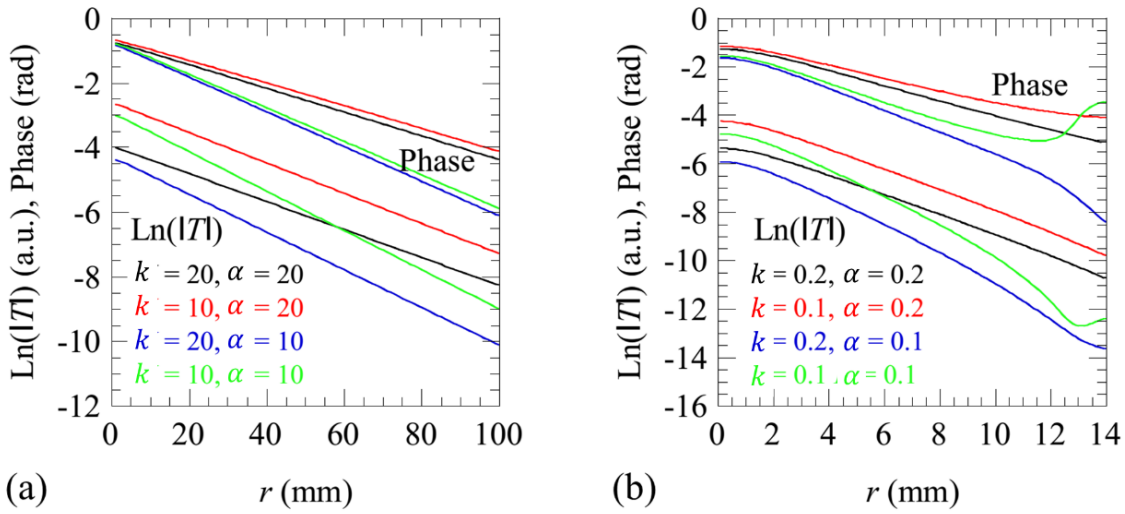

FIGURE 3-16 THE SAME AS IN FIG. 2 BUT FOR THE REAR SURFACE TEMPERATURE ($Ln(r|T|)$ AND Ψ) OF A 2 MM THICK SLAB.

The differences between the curves for thermal insulators are larger, i.e. Figure 3-16, this denotes an increase in sensitivity. Note that for the simulations of the rear surface temperature we have plotted $Ln(|T|)$ instead of $Ln(r|T|)$ since the former will be used in the experimental data fittings.

Sensitivity Analysis

The reduced sensitivity of a measurable variable M to a given thermal property x can be defined as(Ozisik, Orlande et al. 2002):

$$S^M(x) = x\frac{\partial M}{\partial x} \tag{3.26}$$

Where $M = \ln(|T|r)$, $\ln(|T|)$ or phase (Ψ), and $x = \alpha$ or k

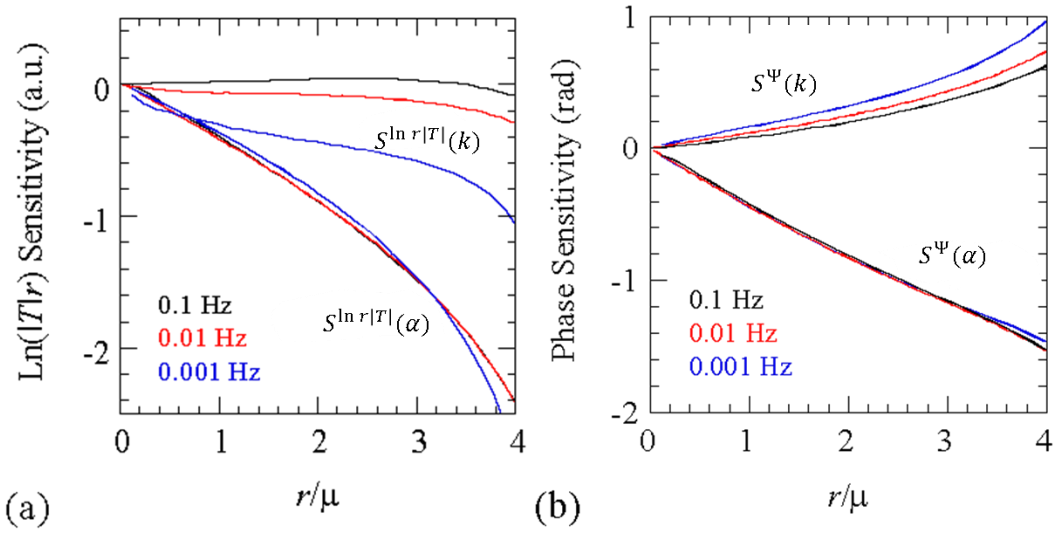

FIGURE 3-17 NORMALIZED RADIAL DEPENDENCE OF THE FRONT SURFACE SENSITIVITY OF $ln(|T|r)$ AND Ψ TO k AND α FOR A THERMALLY VERY THICK INSULATOR: k = 0.2 $\frac{W}{mK}$ AND α = 0.2 $\frac{mm^2}{s}$. THE FOLLOWING PARAMETERS HAVE BEEN USED IN THE SIMULATIONS: $a = 0.2\,mm, h = 15\frac{W}{m^2K}, k_g = 0.025\frac{W}{mK}$ AND $\alpha_g = 21\frac{mm^2}{s}$. THREE MODULATION FREQUENCIES ARE ANALYZED.

Here we present some sensitivity simulations that have been performed by keeping fixed the following parameters: a = 0.2 mm, h = 15 $Wm^{-2}K^{-1}$, k_g = 0.025 $Wm^{-1}K^{-1}$ and α_g = 21 mm^2/s. First, we consider a thermally very thick insulator: k = 0.2 $Wm^{-1}K^{-1}$ and α = 0.2 mm^2/s. Figure 3-17 shows the front surface sensitivity of normalized ln(|*T*|*r*) and Ψ to k and α. Three low frequencies are analyzed: 1, 10 and 100 mHz. For a proper comparison, the radial distance is normalized to the thermal diffusion length $\mu = \sqrt{D/(\pi f)}$. As can be observed, the sensitivity to the thermal diffusivity does not depend on the frequency. The sensitivity to the thermal conductivity, instead, increases as the frequency decreases. On the other hand, both sensitivities increase with the normalized distance to the laser spot, r/μ. It is worth noting that the sensitivities of ln(|*T*|*r*) to k and α for a given frequency are slightly correlated (see Figure 3-17a). The same happens with the phase of the signal (see Figure 3-17b). However, the correlation factors are different for ln(|*T*|*r*) and for Ψ (in fact, the former is positive while the later is negative). This result indicates that α and k are uncorrelated provided that both Ln(|*T*|*r*) and Ψ and fitted simultaneously.

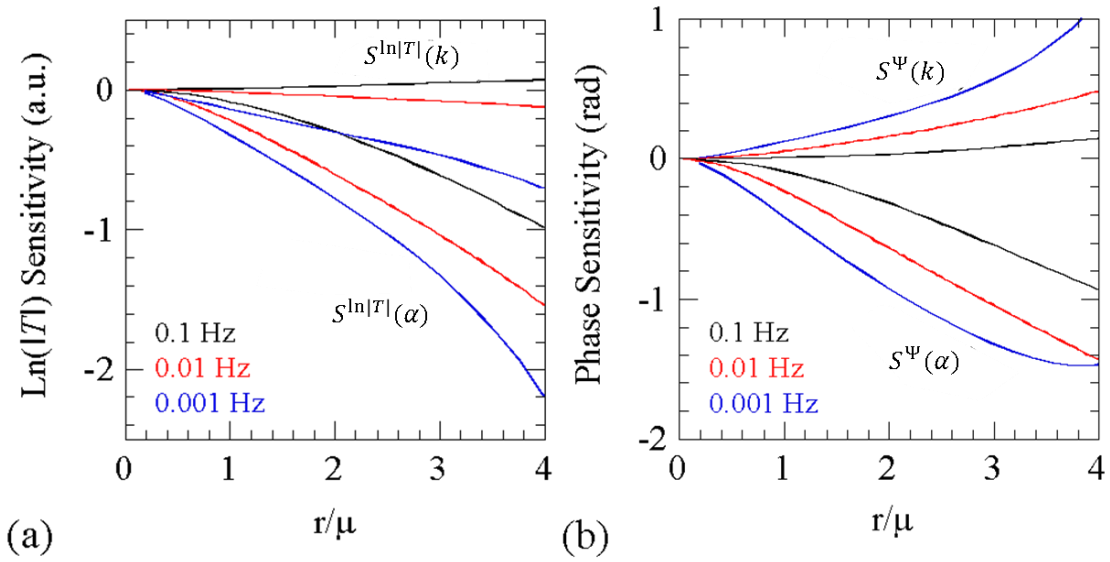

FIGURE 3-18 THE SAME AS IN FIGURE 3-17 FOR THE REAR SURFACE TEMPERATURE ($ln(|T|)$ AND Ψ) OF A 2 MM THICK SLAB.

Then, we consider the rear surface temperature of a 2 mm thick slab made of the same thermal insulator as before. Figure 3-21 shows the sensitivity of ln(|*T*|) and Ψ to *k* and α. Although the sensitivity behavior shown in Figure 3-18 and Figure 3-17 is quite similar, some differences deserve comment. On the one hand, the sensitivity to α of the rear surface temperature of a slab does depend on the modulation frequency. Moreover, the influence of the frequency on the sensitivity to k is more remarkable than in the case of a thermally very thick slab. Considering these results together with the fact that it is experimentally more convenient to record the rear surface temperature than the front one, we decided to perform experiments on the back surface of thin slabs.

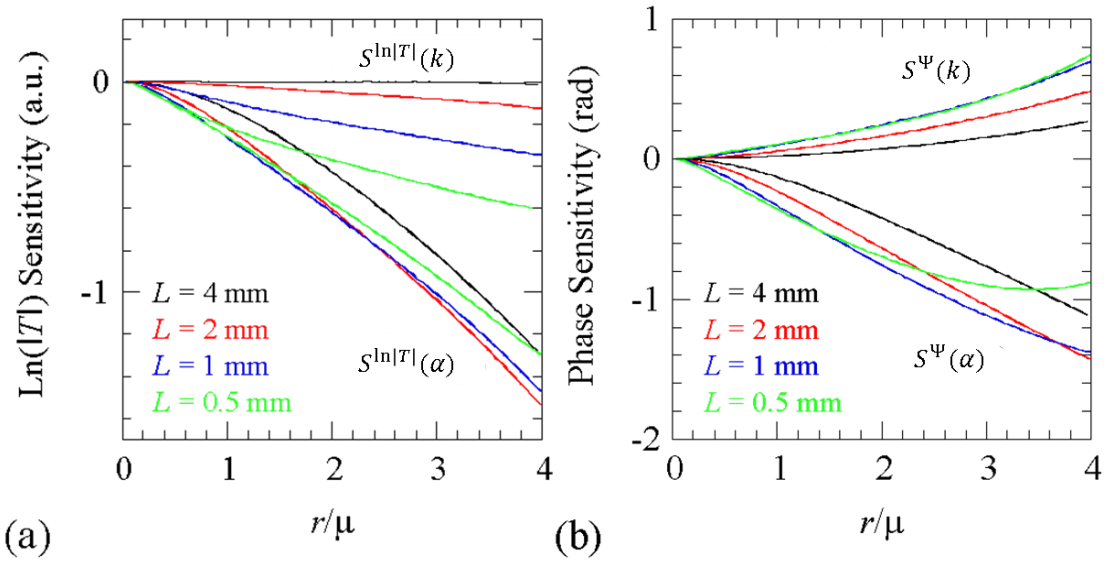

FIGURE 3-19 THE SAME AS IN FIG. 5 BUT KEEPING THE FREQUENCY FIXED AT F = 0.01 HZ. FOUR SAMPLE THICKNESSES ARE ANALYZED.

In Figure 3-22 we show the influence of the sample thickness on the sensitivity to k and α. Calculations are performed for the same thermal insulator as in previous figures, but keeping the modulation frequency fixed at $f = 10\ mHz$. Four thicknesses are analyzed, covering the range from larger and shorter than the thermal diffusion length at this frequency ($\mu = 2.52\ mm$). As can be observed, the sensitivity to *D* barely changes with the sample thickness, provided it is shorter than the thermal diffusion length. The sensitivity to *K*, instead, increases for thinner samples, especially for the natural logarithm of the temperature amplitude, until the maximum sensitivity is obtained for $L \approx \mu/5$. For thinner samples the sensitivity decreases.

Experimental Setup

A continuous wave laser (532 nm), whose intensity is modulated by an acousto-optic modulator, is directed to the sample surface by means of a mirror. The laser beam is focused onto the sample surface using a 15-cm focal length lens. The laser power is changed (50 mW - 200 mW) for each material to obtain a similar temperature rise at the center of the laser spot of about 10K.

An IR video camera (FLIR, model SC7500) with an InSb detector, operating in the 3-5 μm spectral range, records the sample surface temperature. A 50 mm Ge lens used at its minimum working distance provides a spatial resolution of 150 μm, i.e. each pixel measures the average temperature over a square of 150 μm side. The sample is placed horizontally to have a homogeneous temperature distribution at the surface due to a homogeneous convective heat transfer. Figure 3-20 depicts the setup used.

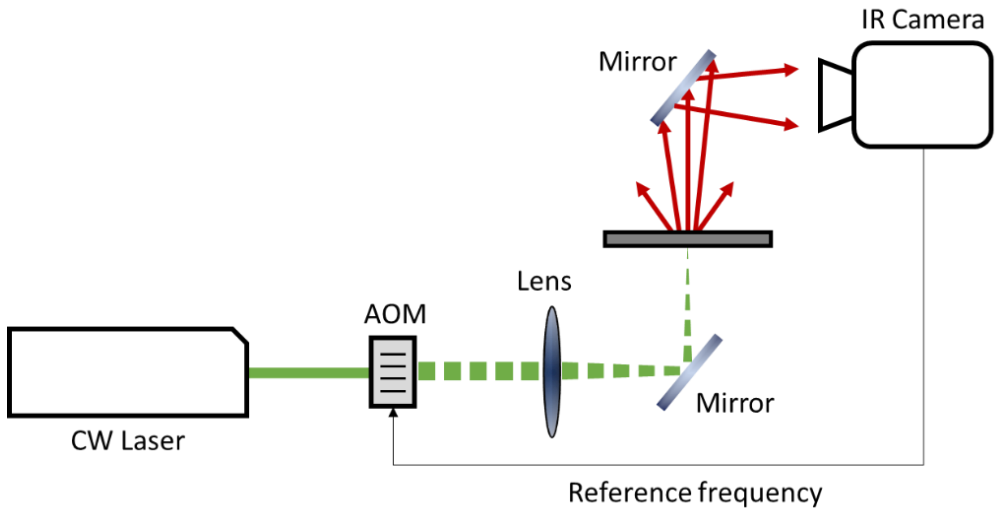

FIGURE 3-20 EXPERIMENTAL SET-UP

The lock-in measurement will have an average noise in dependence of the number of acquired images, as seen in equation 3.3. The NETD for the Flir SC7500 camera being used has been estimated at 20 mK. The camera is set-up to work at a frame rate of 300 fps. Depending on the modulation frequency, images are collected anywhere from 5 to 10 minutes. This sets the noise in the data at approximately 0.1 mK.

The materials selected for this study are semitransparent to the excitation wavelength, some of them exhibiting a high degree of light scattering. To avoid overcomplicating the model a small aluminum foil target ($< 1mm^2$) was adhered to the surface being heated by the laser. The laser beam is focused onto this target guaranteeing superficial absorption and optical opaqueness. Furthermore, many of the materials are also semitransparent to the infrared detector wavelength. A thin black paint layer of a few micrometers in thickness was sprayed onto the sample's camera facing surface. Although the paint layer is very thin when compared to the thickness of the materials being measured, we have used a sharp blade to produce small rips in the paint layer to hinder heat diffusion through it.

Results

Three calibration samples where used: Polycarbonate (PC), Polyether-ether-ketone (PEEK) and Polymethyl-methacrylate (PMMA). Figure 3-21 shows the radial behavior of the back-surface temperature (Ln(|T|) and Ψ) of a 0.51 mm thick PEEK sheet at four modulation frequencies. Dots are the experimental data and the continuous lines are the best fittings to equation 3.22. The temperature amplitude values are normalized to the value at *r* = 0 to avoid introducing an unknown parameter: the dependence on the absorbed laser power.

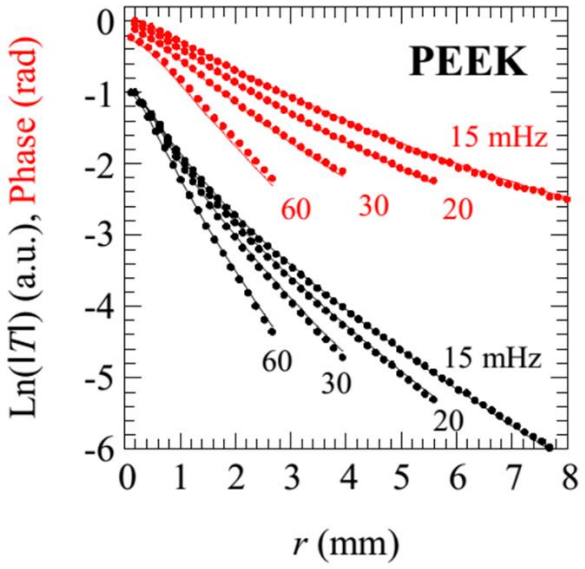

FIGURE 3-21 RADIAL DEPENDENCE OF THE REAR SURFACE TEMPERATURE (AMPLITUDE AND PHASE) OF A 0.51 MM THICK PEEK SLAB. DOTS ARE THE EXPERIMENTAL DATA AND THE CONTINUOUS LINES ARE THE FITTINGS TO EQ. (3). FOUR MODULATION FREQUENCIES HAVE BEEN FITTED SIMULTANEOUSLY TO OBTAIN ACCURATE VALUES OF THE THERMAL PARAMETERS

Note that four frequencies have been fitted simultaneously to obtain more reliable values. The retrieved values of k and α for PEEK, together with the values for the other two mentioned polymers, are given in Table 3-2. They agree very well with the accepted values of these polymers (Goodfellow 2016), conforming the validity of the method for homogeneous thermal insulators.

TABLE 3-2 ROOM TEMPERATURE THERMAL DIFFUSIVITY AND CONDUCTIVITY OF THE THERMAL INSULATORS STUDIED IN THIS WORK. THE UNCERTAINTY IS 5% FOR α AND 10% FOR k.

Material	L (mm)	$\alpha\ (mm^2/s)$	$\alpha\ (mm^2/s)$ Literature	$k\ (W/mK)$	$k\ (W/mK)$ Literature
PEEK [a]	0.51	0.18	0.18	0.25	0.25
PC [a]	1.08	0.14	0.13-0.15	0.21	0.19-0.22
PMMA [a]	1.40	0.10	0.10-0.11	0.16	0.17-0.19
Copy paper[b]	0.10	0.15	0.145	0.16	0.08-0.18
Watercolour paper	1.75	0.27	-	0.052	-
XPS blue[c]	4.0	0.51	-	0.040	0.032-0.040
XPS pink[c]	4.1	0.45	-	0.036	0.032-0.040
XPS yellow[c]	3.9	0.38	-	0.035	0.032-0.040

[a] (Goodfellow 2016), [b](Niskanen and Simula 1999), [c](Domínguez-Muñoz, Anderson et al. 2010)

Finally, with the aim of testing the method on very poor thermal conductors we measured the thermal transport properties of extruded polystyrene foam (XPS), which consists of closed cells and offers improved surface roughness, higher stiffness and reduced thermal conductivity. Its density range is about 28–50 kg/m^3 and the thermal conductivity varies between 0.032 and 0.040 Wm^{-1}K^{-1} (Domínguez-Muñoz, Anderson et al. 2010, Coquard, Coment et al. 2013). We tested 3 samples from different manufacturers. They differ on the pore size and we named them according to their colour: blue (pore size 50±20 μm), pink (pore size 125±40 μm) and yellow (pore size 300±100 μm).

In Figure 3-22b we show the back-surface temperature of the pink sample as a function of the radial distance to the laser spot for three modulation frequencies. As before, dots are the experimental data and the continuous lines are the simultaneous fittings to equation 3.22. The retrieved values of *K* and *D* for the three XPS samples we have dealt with are given in Table 3-2. As can be seen, the thermal conductivity values agree with the literature data and they approach the air value due to their very low density. Regarding the thermal diffusivity, we have not found reference values, but it is enhanced with respect to homogeneous PS (0.08-0.10 mm^2/s) due to the presence of a huge volume fraction of air, which is a good thermal diffuser.

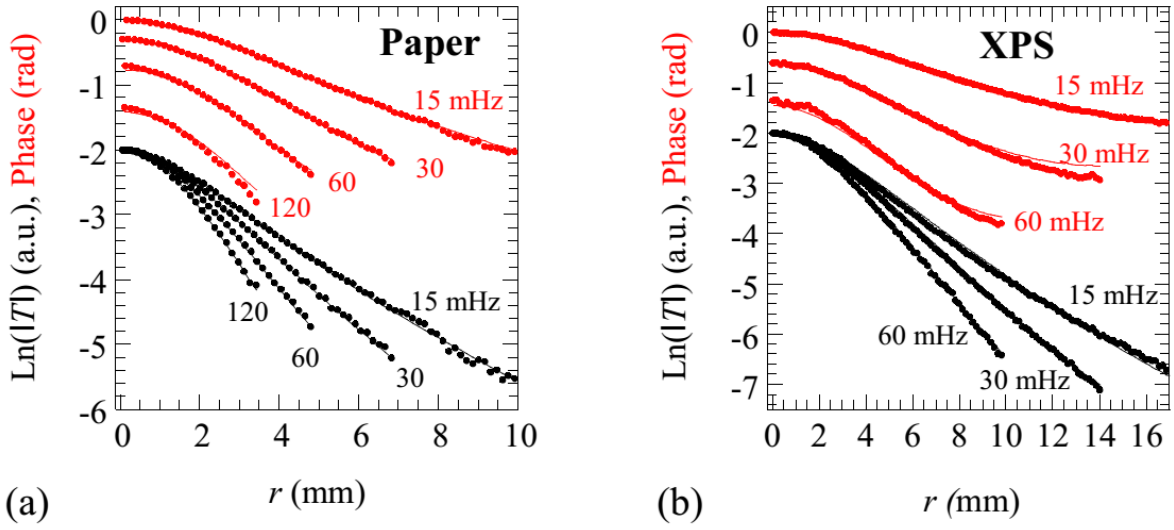

FIGURE 3-22 THE SAME AS IN FIGURE 3-21 BUT FOR: (A) WATERCOLOR PAPER SHEET AND (B) EXTRUDED POLYSTYRENE (XPS), THE PINK SAMPLE.

As can be seen, the thermal conductivity values agree with the literature data and they approach the air value due to their very low density. Regarding the thermal diffusivity, we have not found reference values, but it is enhanced with respect to homogeneous PS (0.08-0.10 mm^2/s) due to the presence of a huge volume fraction of air, which is a good thermal diffuser. For statistical purposes, we have repeated each measurement three times. The α and k values given in Table 3-2 are the mean values while the standard deviation is 5% for *D* and 10% for *K*.

Conclusions

In this work, we propose a method to measure simultaneously the in-plane thermal conductivity and diffusivity of poor thermal conductors. The method is based on illuminating the sample by a modulated and focused laser beam and recording the surface temperature by an infrared video camera. It has been demonstrated that the surface temperature of a bad thermal conductor is greatly affected by heat conduction to the surrounding air. Accordingly, the surface temperature depends on the ratio between the thermal conductivity of the air and the thermal conductivity of the sample. As the thermal conductivity of the air is known, the thermal conductivity of the sample can be obtained. It has been shown that the accuracy of the method increases for poor thermal conductors and using low modulation frequencies. Experiments performed on calibrated thermal insulators have demonstrated the ability of the method to retrieve k and α simultaneously. Our aim is to extend this method to characterize the thermal transport properties of free standing thin films and filaments, for which the influence of heat conduction to the air is much higher than for bulk samples. In this way, the method could be applied even to good thermal conductors.

5. References

Abate, J. and W. Whitt (2006). "A unified framework for numerically inverting Laplace transforms." INFORMS Journal on Computing **18**(4): 408-421.

Astarita, T. and G. M. Carlomagno (2012). Infrared thermography for thermo-fluid-dynamics, Springer Science & Business Media.

Balageas, D. L. (1989). "Thermal diffusivity measurement by pulsed methods." High Temperatures and High Pressures **21**: 85-96.

Ball, R. J. and D. P. Almond (1998). "The detection and measurement of impact damage in thick carbon fibre reinforced laminates by transient thermography." NDT & e International **31**(3): 165-173.

Breitenstein, O. and M. Langenkamp (2003). Lock-in thermography: basics and use for functional diagnostics of electronic components, Springer Science & Business Media.

Busse, G. (1994). "Nondestructive evaluation of polymer materials." NDT & e International **27**(5): 253-262.

Cengel, Y. A. (2003). "Heat transfer: a practical approach." MacGraw Hill, New York.

Coquard, R., et al. (2013). "Analysis of the hot-disk technique applied to low-density insulating materials." International Journal of Thermal Sciences **65**: 242-253.

Depriester, M., et al. (2005). "New methodology for thermal parameter measurements in solids using photothermal radiometry." Review of Scientific Instruments **76**(7): 074902.

Domínguez-Muñoz, F., et al. (2010). "Uncertainty in the thermal conductivity of insulation materials." Energy and Buildings **42**(11): 2159-2168.

Gaussorgues, G. (1994). Infrared Thermography, Springer Science+Business Media.

Goodfellow, C. (2016). from http://www.goodfellow.com.

He, Y. (2005). "Rapid thermal conductivity measurement with a hot disk sensor: Part 1. Theoretical considerations." Thermochimica Acta **436**(1): 122-129.

Herschel, W. (1800). "Experiments on the refrangibility of the invisible rays of the sun. by william herschel, ll. dfrs." Philosophical Transactions of the Royal Society of London: 284-292.

Herschel, W. (1800). "Experiments on the Solar, and on the Terrestrial Rays that Occasion Heat; With a Comparative View of the Laws to Which Light and Heat, or Rather the Rays Which Occasion Them, are Subject, in Order to Determine Whether they are the Same, or Different. Part II. By William Herschel, LL. DFRS." Philosophical Transactions of the Royal Society of London **90**: 437-538.

Huang, H., et al. (2005). "Aligned carbon nanotube composite films for thermal management." Advanced materials **17**(13): 1652-1656.

Jackson, W. B., et al. (1981). "Photothermal deflection spectroscopy and detection." Appl. Opt. **20**(8): 1333.

Krapez, J.-C., et al. (2004). "Measurement of in-plane diffusivity in non-homogeneous slabs by applying flash thermography." International Journal of Thermal Sciences **43**(10): 967-977.

Maldague, X. P. (2002). "Introduction to NDT by active infrared thermography." Materials Evaluation **60**(9): 1060-1073.

Maldague, X. P. (2012). Nondestructive evaluation of materials by infrared thermography, Springer Science & Business Media.

Marín, E. (2007). "The role of thermal properties in periodic time-varying phenomena." European Journal of Physics **28**(3): 429-445.

Mendioroz, A., et al. (2009). "Thermal diffusivity measurements of thin plates and filaments using lock-in thermography." Rev Sci Instrum **80**(7): 074904.

Nagpure, S. C., et al. (2010). "Thermal diffusivity study of aged Li-ion batteries using flash method." Journal of power sources **195**(3): 872-876.

Niskanen, K. and S. Simula (1999). "Thermal diffusivity of paper." Nordic Pulp & Paper Research Journal **14**(3): 236-242.

Ozisik, M., et al. (2002). "Inverse heat transfer: fundamentals and applications." Applied Mechanics Reviews **55**: B18.

Parker, W. J., et al. (1961). "Flash Method of Determining Thermal Diffusivity, Heat Capacity, and Thermal Conductivity." J. Appl. Phys. **32**(9): 1679.

Pech-May, N. W., et al. (2015). "Simultaneous measurement of thermal diffusivity and effusivity of solids using the flash technique in the front-face configuration." Measurement Science and Technology **26**(8): 085017.

Pech-May, N. W., et al. (2016). "Study of the thermal properties of polyester composites loaded with oriented carbon nanofibers using the front-face flash method." Polymer Testing.

Rogalski, A. (2003). "Infrared detectors: status and trends." Progress in quantum electronics **27**(2): 59-210.

Saintey, M. and D. P. Almond (1995). "Defect sizing by transient thermography. II. A numerical treatment." Journal of Physics D: Applied Physics **28**(12): 2539.

Sakagami, T. and S. Kubo (2002). "Applications of pulse heating thermography and lock-in thermography to quantitative nondestructive evaluations." Infrared Physics & Technology **43**(3): 211-218.

Salazar, A. (2003). "On thermal diffusivity." European Journal of Physics **24**(4): 351.

Salazar, A., et al. (2009). "The strong influence of heat losses on the accurate measurement of thermal diffusivity using lock-in thermography." Applied Physics Letters **95**(12): 121905.

Stehfest, H. (1970). "Algorithm 368: Numerical inversion of Laplace transforms [D5]." Communications of the ACM **13**(1): 47-49.

Sun, J. (2006). "Analysis of pulsed thermography methods for defect depth prediction." Journal of Heat Transfer **128**(4): 329-338.

4. Burst Ultrasound Excited Thermography

The thermography techniques explored in the previous chapter dealt with material thermal characterization through optical excitation. As previously mentioned, another important application of thermography is the detection and sizing of defects in samples. Detection of defects through the study of thermal diffusion has been around for several decades now [], but many of the detection techniques required a scanning of the thermal response of a given surface at various points to visualize any obstacles in the diffusion of heat. Thermography eliminates the need of a scan, this has furthered raised the interest in thermal techniques for defect characterization. This final chapter will further explore the uses of thermography in defect detection and show the results of a sub-superficial defect detection experiment carried out during this doctoral work.

1. Introduction

Infrared thermography (IRT) has proven itself to be an important nondestructive technique capable of detecting shallow subsurface defects. A major variant of IRT involves exciting the sample using light, through the photothermal effect, to detect possible defects, such as delaminations and cracks (Castanedo, Avdelidis et al. 2011, Maldague 2012).

Different variants have been developed, some result advantageous for certain types of defects that others do not. For example, homogeneous illumination of a whole surface easily allows for the detection of shallow defects parallel to the sample surface, if the defect is perpendicular to the surface hardly any effect will be perceived on the sample surface temperature. Figure 4-1 depicts such a case, in Figure 4-1a we see a defect parallel to the surface, the defect acts as a large thermal barrier, impeding the diffusion of heat and clearly altering the temperature on both surfaces. If we analyze this in terms of thermal waves, we would see interference on the surface being heated due to thermal wave reflection on the parallel defect. And on the back surface we would see a clear effect on both phase and amplitude due to the thermal impedance created by the flaw.

In Figure 4-1b a defect of the same size but perpendicular to the surface is shown, here the defect hardly interacts with the diffusion process allowing most of the incoming energy to pass. Some minute differences might become visible, but would be unlikely to allow for an accurate profiling.

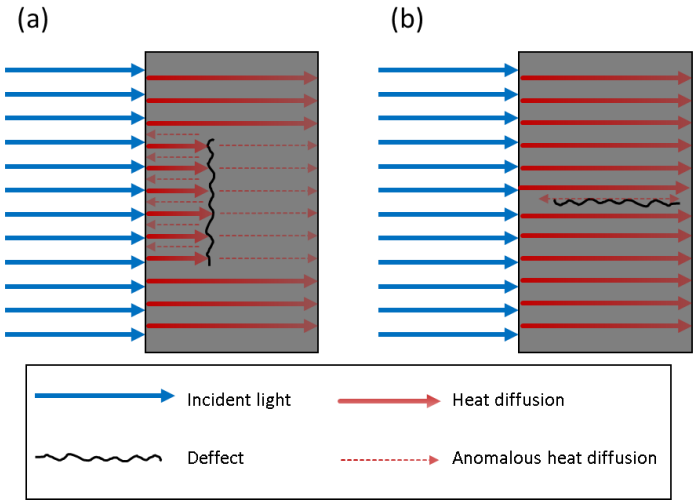

FIGURE 4-1 (A) DEFECT PARALLEL TO THE SURFACE (B) DEFECT PERPENDICULAR TO THE SURFACE UNDER FLAT SURFACE ILLUMINATION

To overcome this, when the defect is vertical to the surface heat flow should be lateral with respect to the defect making homogeneous illumination ineffective. Instead a focused beam of light must be used to establish lateral flow(Wang, Kuo et al. 1990, Schlichting, Ziegler et al. 2011). The defect or crack will behave as a thermal resistance and should become apparent by asymmetries in the temperature distribution of the object. A scan with the laser may be needed to detect the defect since the range of detection will depend on the thermal diffusion length.

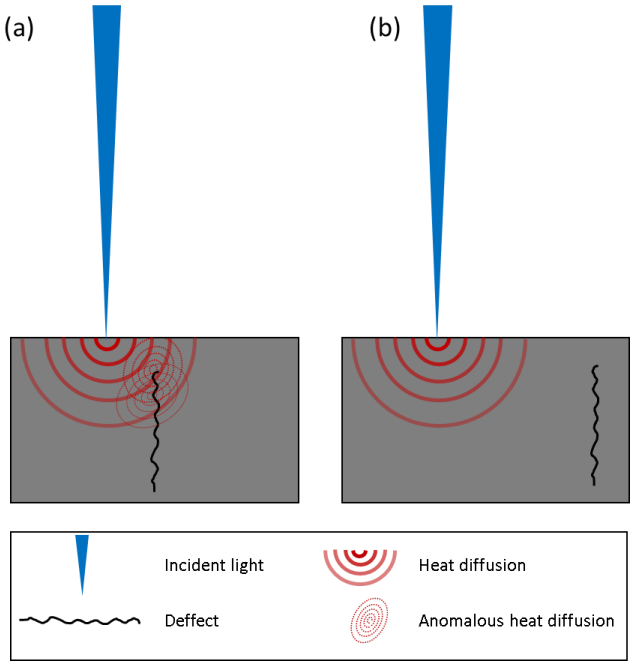

FIGURE 4-2 DEFECT UNDER POINT ILLUMINATION, NOTE THAT IF THE DEFECT IS NOT WITHIN THE HEAT DIFFUSION AREA OF THE POINT SOURCE SCANNING MAY BE NEEDED

These optical techniques are well suited for cracks that offer a strong thermal barrier, however contact defects, also known as kissing cracks present a greater challenge. In a contact defect, no large gap or discontinuity is formed within the specimen this leads to a good thermal contact in that makes defect detection and sizing difficult. Vibrothermography, i.e. ultrasound excited thermography, offers an alternative very well suited to detect weak thermal barrier defects.

Vibrothermography involves the probing of the internal integrity and uniformity of a sample by observing, through a thermographic camera, the heat pattern produced by the energy dissipation that occurs when a vibrational excitation is applied (Reifsnider, Henneke et al. 1980). This technique requires the sample to be subjected to mechanical vibrations, usually through ultrasound. The defect converts mechanical energy, i.e. vibrations, into thermal energy through several phenomena, the most important one in the case of contact defects being friction between the two surfaces in contact. Friction results from the fact that the two surfaces will not move in unison when the sound propagates through the object(Han 2007). Its ability to detect cracks in numerous materials has been shown (Favro, Han et al. 2000, A, X et al. 2004, P, A et al. 2008).

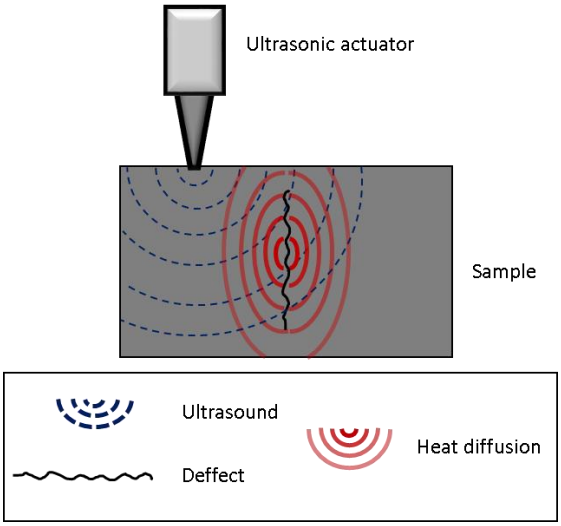

FIGURE 4-3 SCHEMATIC DEPICTING VIBROTHERMOGRAPHY, HERE THE DEFECT BECOMES THE HEAT SOURCE ALLOWING FOR THE DETECTION OF KISSING CRACKS AND DEFECTS WITH GOOD THERMAL CONTACT

It is not only possible to detect defects, one may also geometrically characterize a crack using the surface temperature data from a vibrothermography test. The ability to do so using lock-in amplification has been shown. (Celorrio, Mendioroz et al. 2013, Mendioroz, Castelo et al. 2013)

However, lock-in vibrothermography has a major drawback. Data acquisition is slow, taking about 40 minutes per sample, making the method impractical for many applications. Time resolved techniques are renowned for their short acquisition times and can be applied to

vibrothermography. A step function or ultrasound burst can be used to excite the sample and produce the necessary data for crack characterization. Burst typically last between 50 ms to a few tens of seconds, with the total acquisition time being less than one minute

In this chapter, we present quantitative characterizations of rectangular vertical and half-penny (semicircular) cracks from burst vibrothermography data. A mathematical model for inverting surface temperature data from cracks with a given geometry has been developed. To show the experimental validity of this model burst vibrothermography experiments using calibrated samples were performed. The experimental data fittings confirm that it is possible to characterize a crack using different burst times and makes way for further development of time resolved vibrothermography techniques to characterize contact defects.

2. Theory and Mathematical Model

Let us assume that a vertical rectangular contact defect generates a homogeneous heat flux, I, during an ultrasound burst with a constant intensity lasting a time interval τ. We can start our modeling by considering an instantaneous point-like heat source located at $\vec{r}\,'$ which delivers energy *Q* at time *t'* in an infinite medium with thermal diffusivity α. The temperature at any point $\vec{r}$ of the material at t>t' is given by (Carslaw and Jaeger 1959):

$$T(\vec{r},t) = \frac{Q}{8\rho c[\pi\alpha(t-t')]^{3/2}} e^{-\frac{|\vec{r}-\vec{r}'|^2}{4\alpha(t-t')}} \tag{4.1}$$

We can than account for the time duration of the pulse by considering that the heat source delivers a constant power during a time interval [0,τ], where τ represents the burst duration. The temperature at any point will be given by (Li, Almond et al. 2011):

$$T(\vec{r},t) = \begin{cases} \dfrac{P}{4\pi k|\vec{r}-\vec{r}'|} Erfc\left[\dfrac{|\vec{r}-\vec{r}'|}{\sqrt{4\alpha t}}\right] & 0 \le t \le \tau \\ \dfrac{P}{4\pi k|\vec{r}-\vec{r}_0|}\left(Erfc\left[\dfrac{|\vec{r}-\vec{r}'|}{\sqrt{4\alpha t}}\right] - Erfc\left[\dfrac{|\vec{r}-\vec{r}'|}{\sqrt{4\alpha(t-\tau)}}\right]\right) & t > \tau \end{cases} \tag{4.2}$$

Now we may consider the effect of the spatial dimension of the heat source. In the case of a vertical rectangular heat source contained in a plane at *x=0* which has a width *w*, a height *h* and is buried at a distance *d* below the sample surface (Figure 4-4).

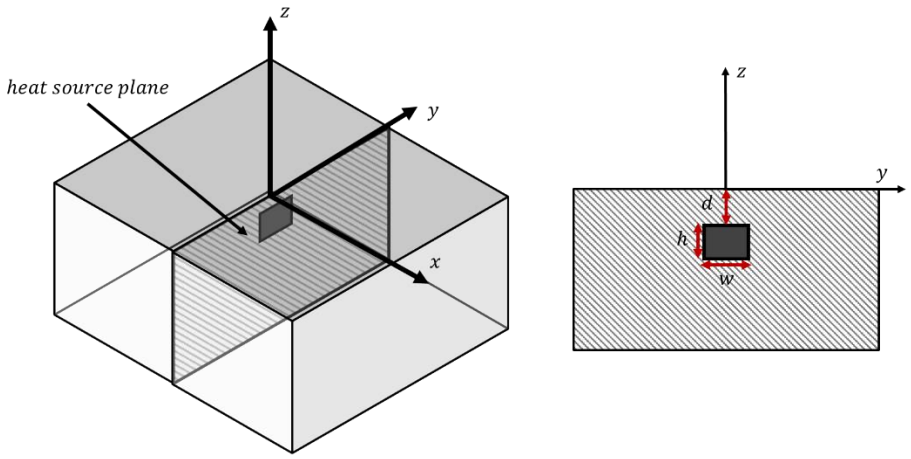

FIGURE 4-4 PROBLEM GEOMETRY FOR A RECTANGULAR HEAT SOURCE

The temperature at any point in the sample surface will be given by:

$$T(x,y,0,t) = \begin{cases} \dfrac{I}{2\pi k}\displaystyle\int_{-h-d}^{-d}\int_{-w/2}^{w/2} \frac{Erfc\left[\dfrac{\sqrt{x^2+(y-y')^2+z'^2}}{\sqrt{4\alpha t}}\right]}{\sqrt{x^2+(y-y')^2+z'^2}}dy'dz' & 0 \le t \le \tau \\ \dfrac{I}{2\pi k}\displaystyle\int_{-h-d}^{-d}\int_{-w/2}^{w/2} \frac{Erfc\left[\dfrac{\sqrt{x^2+(y-y')^2+z'^2}}{\sqrt{4\alpha t}}\right]}{\sqrt{x^2+(y-y')^2+z'^2}}dy'dz' - & \\ \displaystyle\int_{-h-d}^{-d}\int_{-w/2}^{w/2} \frac{Erfc\left[\dfrac{\sqrt{x^2+(y-y')^2+z'^2}}{\sqrt{4\alpha (t-\tau)}}\right]}{\sqrt{x^2+(y-y')^2+z'^2}}dy'dz' & t > \tau \end{cases} \quad (4.3)$$

We are also assuming that the sample is optically opaque in the infrared portion of the spectrum and given that the proposed method of detection is infrared thermography, only the surface temperature would be experimentally accessible ($z=0$).

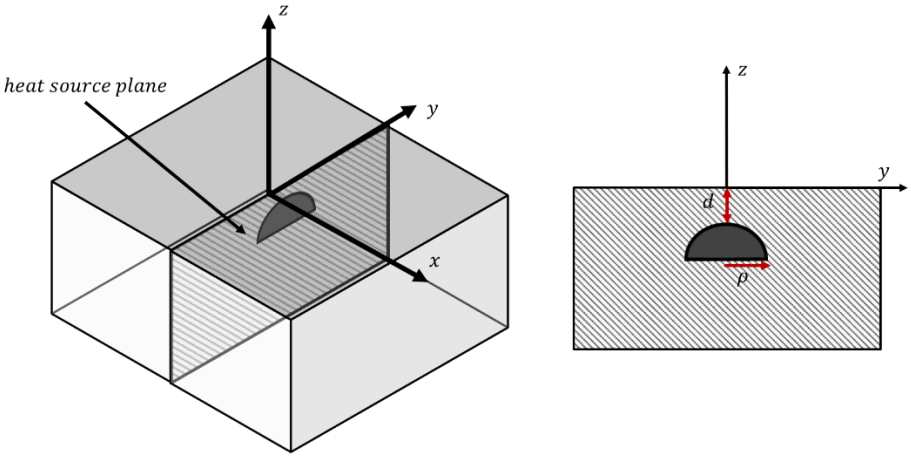

FIGURE 4-5 PROBLEM GEOMETRY FOR A HALF-PENNY OR SEMICIRCULAR HEAT SOURCE

In the case of a half-circle geometry of radius ρ , as the one shown in Figure 4-5, equation 4.2 may be integrated as follows:

$$T(r,x,t) = \begin{cases} \dfrac{I}{2\pi k}\displaystyle\int_0^{\pi}\int_o^{\rho} \frac{r' Erfc\left[\dfrac{\sqrt{r^2+r'^2-2(r'r\cos(\theta-\theta'))+x^2}}{\sqrt{4\alpha t}}\right]}{\sqrt{r^2+r'^2-2(r'r\cos(\theta-\theta'))+x^2}} dr'd\theta' & 0 \le t \le \tau \\ \dfrac{I}{2\pi k}\displaystyle\int_0^{\pi}\int_o^{\rho} \frac{r' Erfc\left[\dfrac{\sqrt{r^2+r'^2-2(r'r\cos(\theta-\theta'))+x^2}}{\sqrt{4\alpha t}}\right]}{\sqrt{r^2+r'^2-2(r'r\cos(\theta-\theta'))+x^2}} dr'd\theta' & \\ \quad\displaystyle\int_0^{\pi}\int_0^{\rho} \frac{r' Erfc\left[\dfrac{\sqrt{r^2+r'^2-2(r'r\cos(\theta-\theta'))+x^2}}{\sqrt{4\alpha (t-\tau)}}\right]}{\sqrt{r^2+r'^2-2(r'r\cos(\theta-\theta'))+x^2}} dr'd\theta' & t > \tau \end{cases} \quad (4.4)$$

Simulations

Different simulation settings were carried out to better grasp the effects of changing one parameter or the order as preparation for the experimental tests. Fitting the model from the synthetic data was also tested. In general, the fitting algorithms work better when the logarithm of the spatial temperature information is used. All simulations were carried out using a thermal diffusivity value of $3.9\times10^{-6}\ m^2/s$, which is the thermal diffusivity of the steel piece that is later used in the experimental procedure.

Model Simulations

The first simulation shown in this work is depicted in Figure 4-6 where the temporal temperature evolution at the geometric center of the surface is shown. In this case, the simulation is for a square defect, $w = 1\ mm, h = 1mm$, buried at a depth of $3\ mm$. Burst times going from 1s to 3s are shown. The temperature is normalized against the temperature reached at the burst time τ. We can see here that, as the burst duration is increased, the maximum temperature rached approaches the temperature at τ.

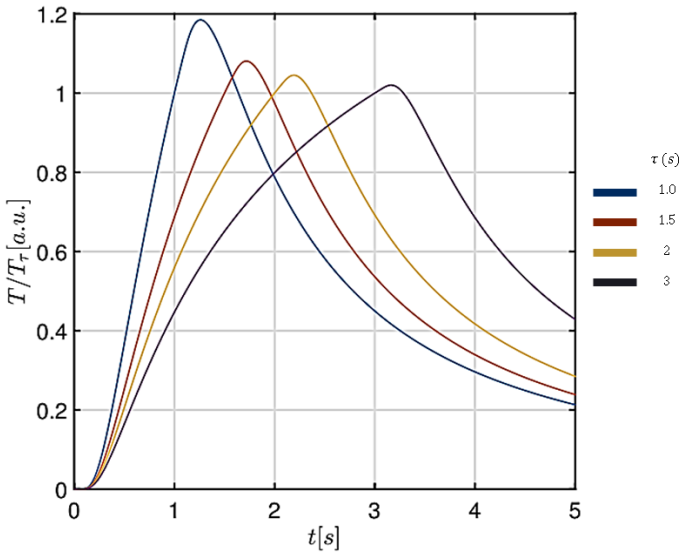

FIGURE 4-6 SIMULATION OF THE TEMPORAL TEMPERATURE EVOLUTION FOR A SQUARE DEFECT ($w = 1mm, h = 1mm, d = 3mm$), FOUR DIFFERENT BURST TIMES ARE SHOWN. TEMPERATURE HAS BEEN NORMALIZED AGAINST THE TEMPERATURE AT τ

Figure 4-7 shows the results of a simulation carried out with a burst duration, τ, of 1 second. The results are normalized against the maximum temperature reached at τ . In Figure 4-7a, the depth of the defect is varied while in Figure 4-7b the width of the defect is varied. Row 1 shows the temporal temperature evolution at the center, i.e. $(x, y, t) = (0,0, t)$. Row 2 shows the spatial temperature evolution of the *y-axis* at the end of the burst, $(x, y, t) = (0, y, \tau)$ and row 3 shows the spatial temperature evolution of the *x-axis* at the end of the burst, $(x, y, t) = (x, 0, \tau)$.

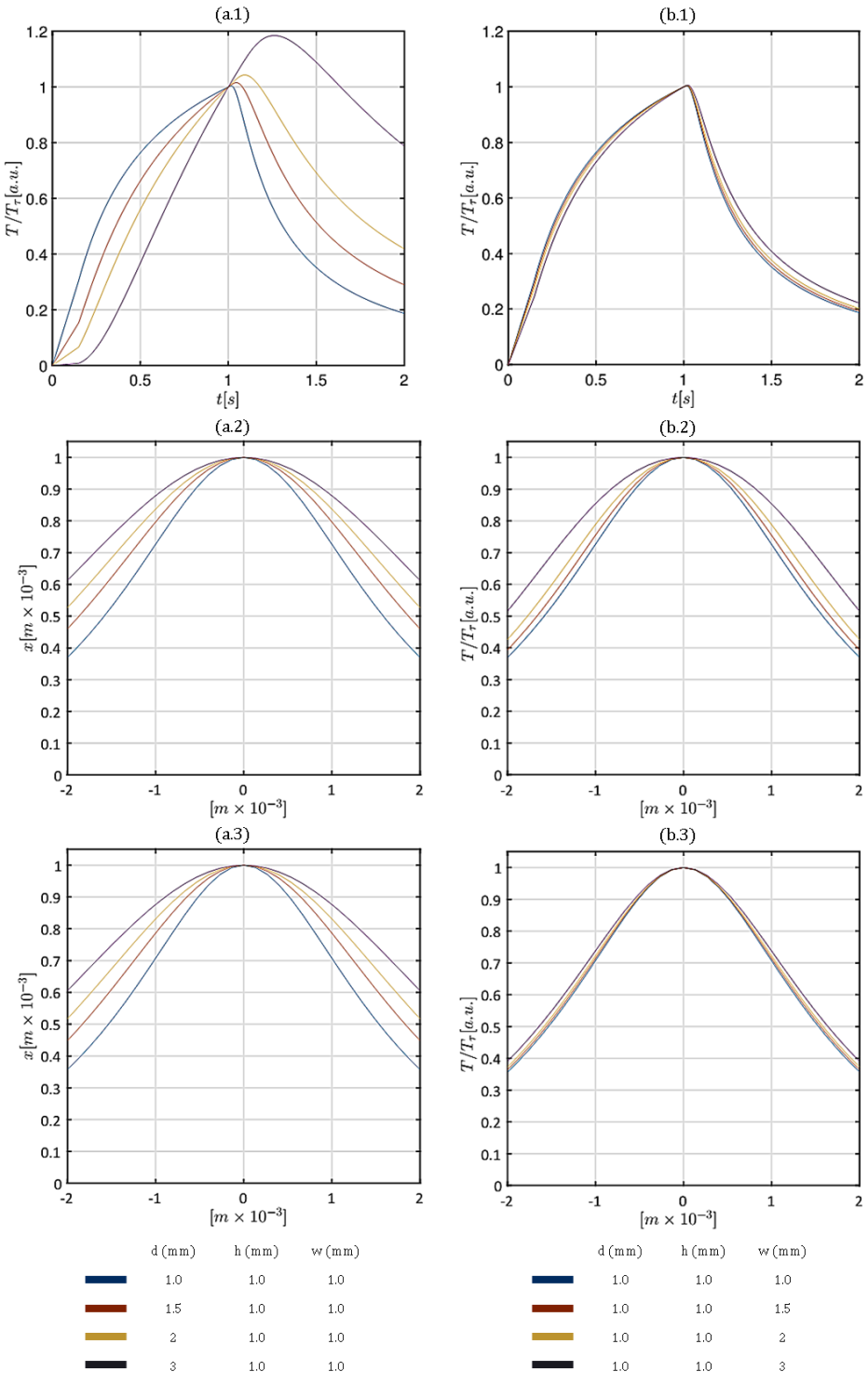

FIGURE 4-7 SIMULATION RESULTS, TEMPERATURE HAS BEEN NORMALIZED AGAINST TEMPERATURE AT τ. ROW 1 SHOWS THE TEMPORAL TEMPERATURE EVOLUTION AT THE CENTER, I.E. $(x, y, t) = (0, 0, t)$. ROW 2 SHOWS THE SPATIAL TEMPERATURE EVOLUTION OF THE Y-AXIS AT THE END OF THE BURST, $(x, y, t) = (0, y, \tau)$ AND ROW 3 SHOWS THE SPATIAL TEMPERATURE EVOLUTION OF THE X-AXIS AT THE END OF THE BURST, $(x, y, t) = (x, 0, \tau)$. $\tau = 1s$ IN ALL CASES

This simulation shows some important behavioral characteristics of the model. When a defect is buried deeper, the time it takes for the heat to diffuse to the surface is increased so that the overall temperature maximum is reached much after τ. Figure 4-7b shows how the spatial distribution is affected by a wider heat source, the widening affects the distribution on the y-$axis$ more profoundly.

This data shows us that deeper defects will require a larger acquisition time while the detection of wider defects will demand suitable spatial data.

Noise Simulations

To test the fitting algorithm, synthetic data with added random noise was generating to simulate a real-world scenario. The simulations were carried out using different signal amplitude vs. noise amplitude ratios (i.e. $\eta = 1 - A_{noise}/A_{signal}$) to test the effect on the ability of the algorithms to extract the geometry of the heat-source. Figure 4-8 depicts one of those simulations. A square $1\times1\ mm$ defect buried at $1\ mm$ depth is simulated, then the η is varied from 1, i.e. no noise, to 0.9. The data is then fed to the fitting algorithm.

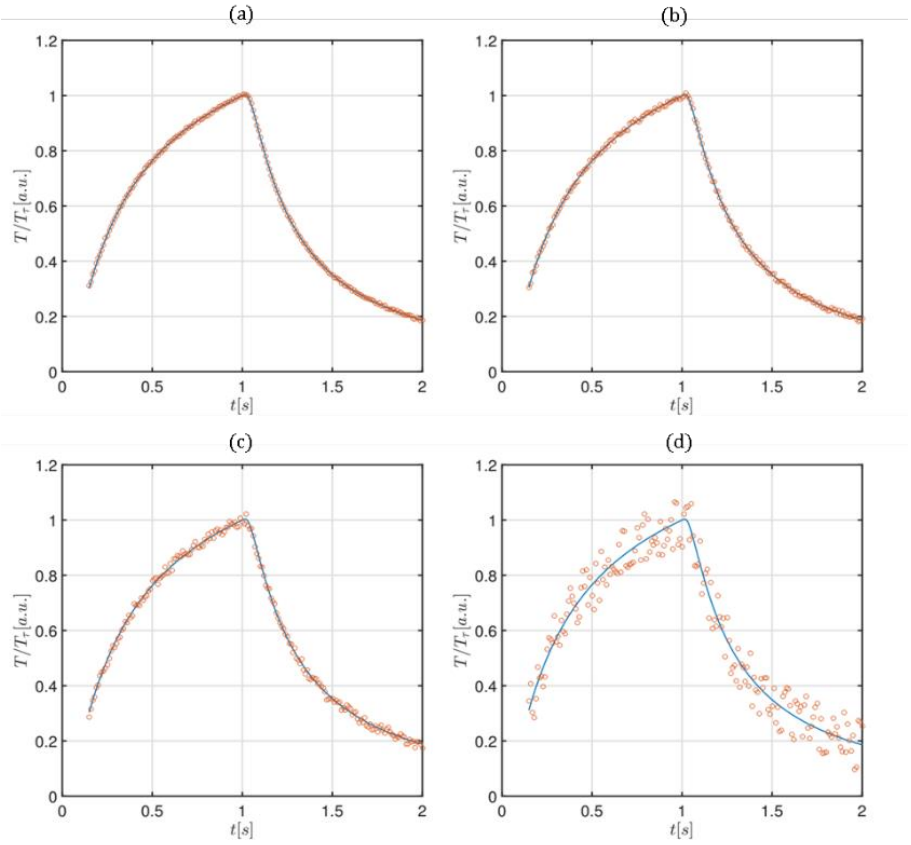

FIGURE 4-8 FITTING (CONTINUOUS BLUE LINE) OF SIMULATED DATA (RED CIRCLES) OF A $1\times1\ mm$ DEFECT AT A DEPTH OF $1\ mm$, RANDOM NOISE HAS BEEN ADDED TO THE DATA. $a)\ \eta = 0.99\ b)\ \eta = 0.98\ c)\ \eta = 0.95\ d)\ \eta = 0.90$. ONLY TEMPORAL DATA IS SHOWN.

Table 4-1 shows the algorithm reconstruction results. The fitting algorithm is relatively unaffected by low noise levels, as the noise increases larger errors arise, as is to be expected. Note that when the η is at 0.90, i.e. the power of the noise is 10% that of the signal, the data is visibly noisy (see Figure 4-8d), yet a good estimate can be obtained. This simulation consisted of around 200 data points.

TABLE 4-1 NOISE SIMULATION RESULTS

η	$d\ mm$	$h\ mm$	$w\ mm$
1	1.00	1.00	1.00
0.99	1.00	0.98	0.99
0.98	0.98	1.03	1.01
0.95	0.98	1.07	1.03
0.90	0.93	1.14	1.10

The simulations for $\eta = 0.90$, 0.95 and 0.98 were repeated with a different random noise profile, this results in variations from fitting to fitting. The variations of 16 such repetitions were studied for the different parameters to better understand the level of uncertainty that random noise introduces into the fitting process, again each simulation fitted approximately 200 points. These η values were selected since these would be in the range of the expected noise in an experimental procedure considering a temperature rise of 1 or 2 K. The following tables summarize the results:

TABLE 4-2 MEAN VALUES FOR 16 SIMULATION REPETITIONS WITH DIFFERENT RANDOM NOISE PROFILES FOR SQUARE DEFECT (SEE FIGURE 4-4) ($w = 1\ mm, h = 1mm$) AT A DEPTH OF $1\ mm$, PARENTHESIS SHOWS THE 95% CONFIDENCE INTERVAL.

η	$\bar{d}\ mm$	$\bar{h}\ mm$	$\bar{w}\ mm$
0.98	0.99 (0.01)	1.01 (0.06)	1.00 (0.04)
0.95	0.98 (0.05)	1.07 (0.16)	1.00 (0.09)
0.90	0.96 (0.06)	1.13 (0.18)	1.01 (0.11)

TABLE 4-3 STANDARD DEVIATION FOR THE SAME SIMULATIONS AS TABLE 4-2

η	$\sigma_d\ mm$	$\sigma_h\ mm$	$\sigma_w\ mm$
0.98	0.02	0.06	0.04
0.95	0.08	0.26	0.15
0.90	0.09	0.28	0.17

The simulation shows how the uncertainty in the fitting clearly increases with the intensity of the random noise. This confirms the importance of having a good SNR during measurements, non-the less, weak signals can offer a good estimate of the position of a defect within a piece.

A good η is not always experimentally obtainable due to many factors, e.g. defect depth or size. Note that the least affected parameter is the defect depth while the most affected is the height.

This procedure was repeated simulating a deeper defect, $w = 1mm, h = 1mm, d = 3mm$. The defect was noticeably more difficult to fit while the η 0.98 simulation had no major issue, η 0.95 failed to converge on approximately 40% of the times while the η 0.90 simulation failed to converge on over 50% of the times. Still, when they did converge, the results give a good estimate of the defect's size and position. The following table summarizes the results.

TABLE 4-4 MEAN VALUES FOR SIMULATION REPETITIONS WITH DIFFERENT RANDOM NOISE PROFILES FOR A SQUARE DEFECT (SEE FIGURE 4-4) ($w = 1\ mm, h = 1mm$) AT A DEPTH OF $3\ mm$, PARENTHESIS SHOWS THE 95% CONFIDENCE INTERVAL. 16 SIMULATIONS WERE EXECUTED PER η LEVEL, HOWEVER, HIGHER η RESULTS IN NON-CONVERGENCE IN SOME CASES, THESE HAVE BEEN INTENTIONALLY LEFT OUT.

η	$\bar{d}\ mm$	$\bar{h}\ mm$	$\bar{w}\ mm$	N
0.98	2.99 (0.05)	1.02 (0.13)	1.05 (0.07)	16
0.95	2.94 (0.1)	1.16 (0.26)	0.93 (0.19)	10
0.90	2.95 (0.11)	1.11 (0.28)	0.99 (0.23)	7

TABLE 4-5 STANDARD DEVIATION FOR THE SAME SIMULATIONS AS TABLE 4-4

η	$\sigma_d\ mm$	$\sigma_h\ mm$	$\sigma_w\ mm$
0.98	0.08	0.20	0.11
0.95	0.16	0.41	0.29
0.90	0.17	0.44	0.37

Note that once again the parameter that is obtained with higher accuracy is the depth. This second round of simulations confirms what can already be suspected through common sense, a deeper defect will be harder to size.

Similar simulations where carried out for a semicircular geometry. The general behavior is similar; however, convergence is faster given that only two fitting parameters are needed, i.e. the radius ρ and the depth. Results or a $1\ mm$ depth semicircular defect of radius $\rho = 1\ mm$ are shown below:

TABLE 4-6 MEAN VALUES FOR 16 SIMULATION REPETITIONS WITH DIFFERENT RANDOM NOISE PROFILES FOR A SEMICIRCULAR DEFECT OF $1\ mm$ RADIUS AND $1\ mm$ DEPTH (SEE FIGURE 4-5), PARENTHESIS SHOWS THE 95% CONFIDENCE INTERVAL.

η	$\bar{\rho}\ mm$	$\bar{d}\ mm$
0.98	1.02 (0.04)	0.99 (0.02)
0.95	1.02 (0.08)	0.99 (0.04)
0.90	0.91 (0.26)	1.05 (0.14)

TABLE 4-7 STANDARD DEVIATION FOR THE SAME SIMULATIONS AS TABLE 4-6

SNR	$\sigma_\rho\ mm$	$\sigma_d\ mm$
0.98	0.07	0.04
0.95	0.12	0.06
0.90	0.41	0.23

It is impossible to show all the simulation work done, however, it can be said that, for the reconstructions algorithms to work properly, both temporal and spatial temperature evolution are needed, otherwise the fitting becomes unprecise and may fail to converge. We have found that fitting a full thermogram at the end of burst and the timing graph at the geometrical center yields the best results in our configuration. It was also observed that the shape of the defect can be reconstructed regardless of the burst duration that is used as long as both spatial and temporal data is fed into the fitting algorithm and a clear enough signal can be obtained (Mendioroz, Celorrio et al. 2015). Experimentally this is not the case, since larger bursts translate into larger temperature increments, so they may yield better results than short bursts, however a burst that is too long may entail effects due to the finite dimensions of the specimen so a compromise must be found.

3. Experimental Procedure

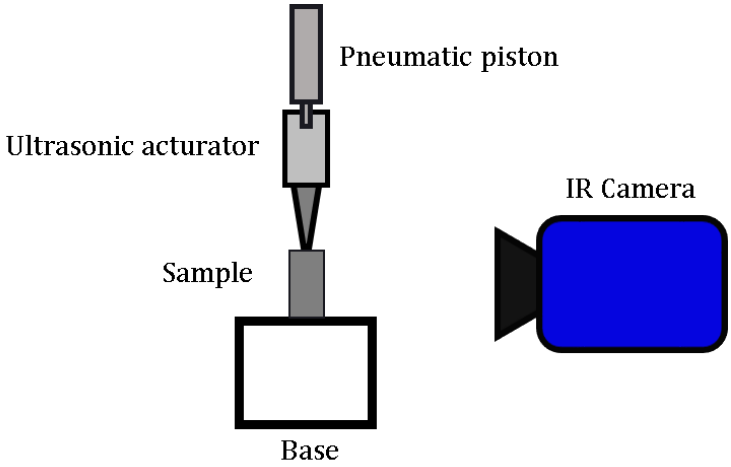

FIGURE 4-9 EXPERIMENTAL SET-UP

Multiple experiments using different samples were performed. The defects in the sample are simulated by using a thin metal foil, usually 38 μm copper. The sample consists of two AISI 304 blocks with flat and rectified common surface. The blocks, with the foil between them, are mechanically pressed together using screws (see Figure 4-10). Two additional foil pieces are placed in the back of the sample, far away from the measuring surface, to avoid any unintentional contact between the steel blocks. Under the influence of the ultrasound friction between the copper foil and the steel surfaces generates the calibrated heat source.

After the sample has been prepared we proceed to submit it to ultrasonic waves using UTvis equipment from EDEVIS at a fixed ultrasound frequency of 23 kHz, which was experimentally determined to be the optimum frequency for our samples. The ultrasonic transducer is pressed against de sample by means of pneumatic piston (see Figure 4-9).

The thermal energy generated by the copper foil diffuses into the material and reaches the surface which has been covered with a thin layer of black pain as to maximize IR emissivity. The surface temperature is recorded using a CEDIP JADE J550M IR camera operating in the 3.5 - 5 μm range and using a 50-mm focal length lens. The pixel resolution achieved is around 135 $\mu m/pixel$.

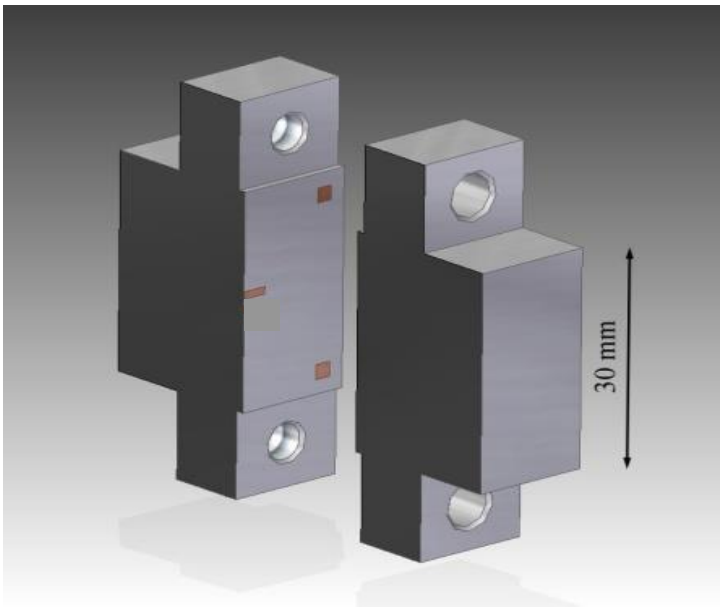

FIGURE 4-10 EXPERIMENTAL SAMPLE (MENDIOROZ, CELORRIO ET AL. 2015)

Once the temperature information has been captured the data is fitted to the model seen before using an algorithm based on the Levenberg-Marquadt algorithm, more information on the LM algorithm is available elsewhere (Moré 1978). Both spatial and temporal data are fitted simultaneously.

4. Results

Through experimentation it was confirmed that the suitable amount of information required to reliably predict the defects dimensions consisted of the temporal evolution of the temperature of the central pixel and the surface temperature distribution at the end of the burst.

A typical experimental result is shown in Figure 4-11. In this case, the defect is located at a depth of 1.1 mm and has a height of 1.5 mm and a width of 1 mm. The upper plots show the result for a 0.5 s burst while the lower plots are for a 1 s burst. Both temporal temperature

evolution of the central point and surface temperature at the burst's end is plotted, contour lines are used represent the temperature across the surface. The plots correspond to the results of sample 6 in Table 4-8.

TABLE 4-8 EXPERIMENTAL RESULTS FOR RECTANGULAR GEOMETRIES

Real values					Fitted values			Error		
Sample	h (mm)	d (mm)	w (mm)	τ (s)	$\hat{h}$ (mm)	$\hat{d}$ (mm)	$\hat{w}$ (mm)	ϵ_h (mm)	ϵ_d (mm)	ϵ_w (mm)
1	2.6	0.7	1.15	0.5	2.7	0.5	1	0.1	0.2	0.2
				0.7	2.3	0.6	1.077	0.3	0.1	0.1
2	2.5	0.75	1	0.25	2.7	0.7	0.8	0.2	0.1	0.2
				0.7	2.4	0.6	1	0.1	0.2	0.0
3	1	0.5	1.2	0.5	0.7	0.6	1.2	0.3	0.1	0.0
				1	1	0.5	1.2	0.0	0.0	0.0
				2	0.9	0.5	1.2	0.1	0.0	0.0
				3	1	0.5	1.3	0.0	0.0	0.1
4	0.9	0.4	1	1	1	0.3	1.15	0.1	0.1	0.2
				0.5	1.1	0.3	1.2	0.2	0.1	0.2
5	1.9	1.1	2.5	1.5	1.8	1	2.3	0.1	0.1	0.2
				1	2.5	0.9	2.1	0.6	0.2	0.4
				0.5	1.4	1.1	0.5	0.5	0.0	2.0
6	1.5	1.1	1	0.5	2.8	0.8	0.9	1.3	0.3	0.1
				1	1.8	0.9	1.0	0.3	0.2	0.0

From this we see that longer bursts seem to achieve greater precision, this is because the signal to noise ratio (SNR) is better for longer bursts since more energy is deposited. In Table 4-8 we can see that the sizing of the cracks provides a good estimate in most of the cases, with longer bursts generally having a lower error. Note that the fittings for the experimental data were done using the natural logarithm of the normalized temperature, this was done simply upon observing a better performance of the algorithm.

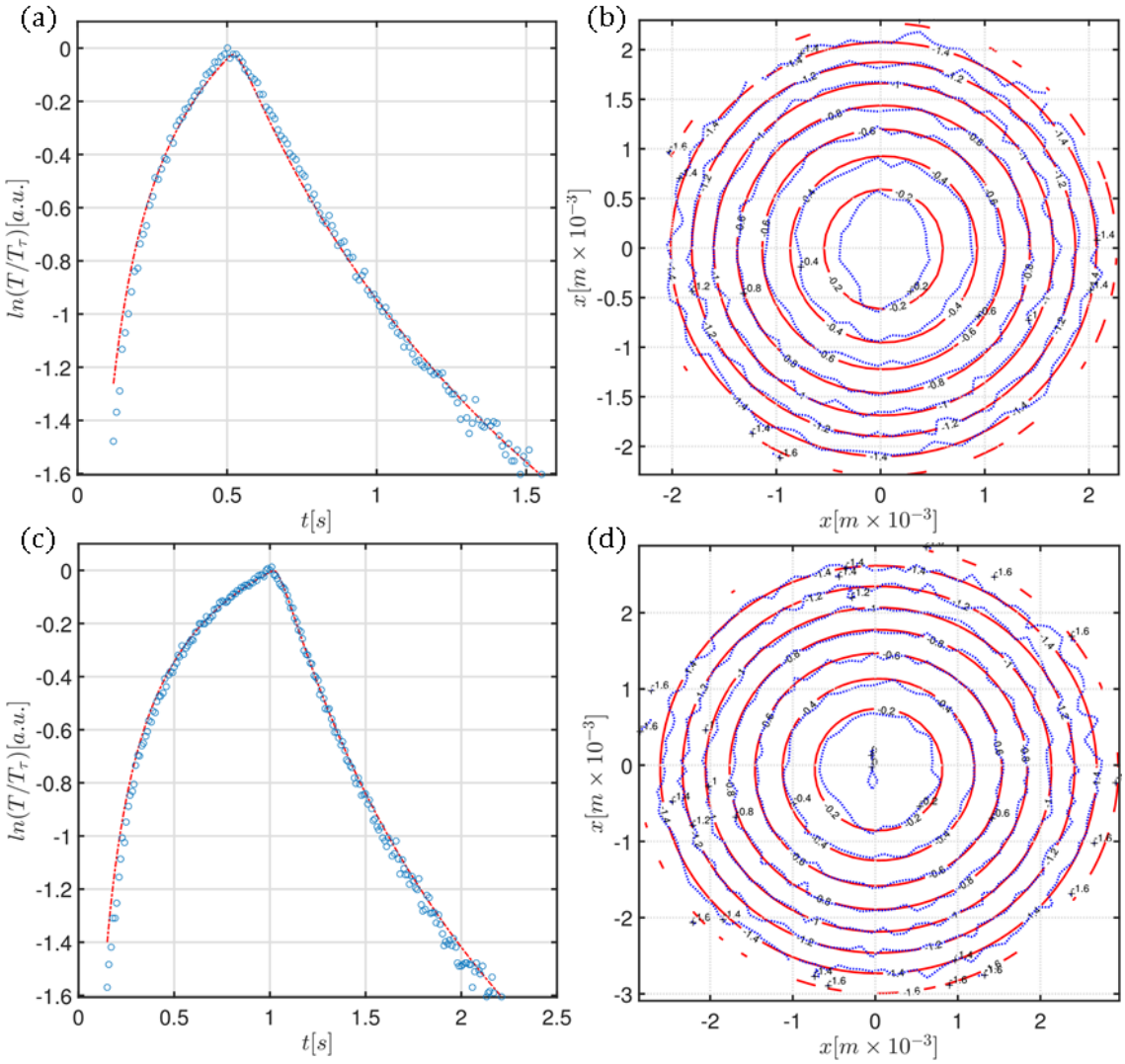

FIGURE 4-11 TYPICAL BURST VIBROTHERMOGRAPHY EXPERIMENTAL RESULTS FOR A RECTANGULAR. LEFT PLOTS REPRESENT THE TEMPORAL EVOLUTION AT THE CENTRAL POINT, RIGHT PLOTS ARE THE TEMPERATURE DISTRIBUTION AT THE END OF THE BURST REPRESENTED BY CONTOUR LINES. (A) AND (B) CORRESPOND TO A BURST TIME OF 0.5 S, WHILE (C) AND (D) CORRESPOND TO A BURST TIME OF 1 S. THE DEFECT CORRESPONDS TO SAMPLE 6 ON TABLE 4-8.

Due to time restrictions fewer tests could be done on semicircular defect geometries, however the few tests carried out gave very good results. Figure 4-12 show an experimental result and fitting of a semicircular defect.

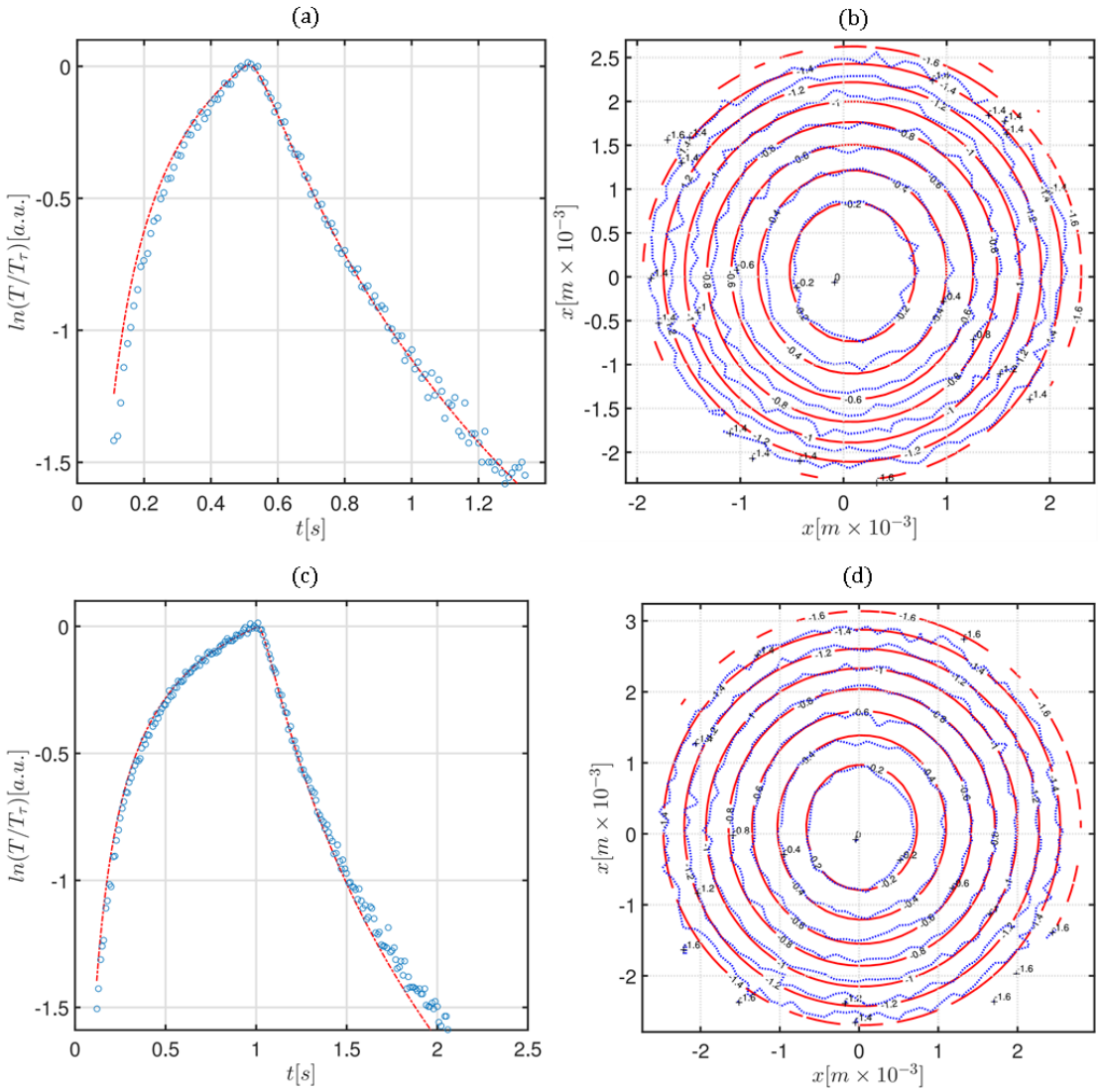

FIGURE 4-12 BURST VIBROTHERMOGRAPHY EXPERIMENTAL RESULTS FOR A HALF-PENNY TYPE DEFECT. LEFT PLOTS REPRESENT THE TEMPORAL EVOLUTION AT THE CENTRAL POINT, RIGHT PLOTS ARE THE TEMPERATURE DISTRIBUTION AT THE END OF THE BURST REPRESENTED BY CONTOUR LINES. (A) AND (B) CORRESPOND TO A BURST TIME OF 0.5 S, WHILE (C) AND (D) CORRESPOND TO A BURST TIME OF 1 S.

The results of the test using a semicircular defect are shown below:

TABLE 4-9 EXPERIMENTAL RESULTS FOR A HALF-PENNY GEOMETRY

$\rho\ (mm)$	$d\ (\mathrm{mm})$	$\tau\ (s)$	$\hat{\rho}\ (mm)$	$\hat{d}\ (mm)$	$\epsilon_\rho\ (mm)$	$\epsilon_d (mm)$
1.3	1	0.5	1.3	1.0	0.0	0.0
		0.5	1.3	0.9	0.0	0.1
		1	1.4	0.9	0.1	0.1
		1	1.4	1.0	0.1	0.0
		2	1.3	0.7	0.0	0.3
		2	1.3	0.8	0.0	0.2

		3	1.5	0.8	0.2	0.2
		3	1.5	0.7	0.2	0.3

5. Conclusions

Burst vibrothermography capabilities to characterize vertical cracks have been shown. The evolution of the temperature distribution was calculated for a heat source emitting a homogeneous and constant flux during a given time interval. Although only rectangular and semicircular geometries are shown in this chapter, the procedure seen here can be used for a vast number of geometries.

The technique has demonstrated its capability to detect and size sub superficial defects, both in simulation and in experimental results. The fast acquisition time make this technique more practical then lock-in detection even though results can be more imprecise.

The effects of random noise on the fitting algorithm were also explore, the algorithm is able to fit noisy data up to a certain point under the understanding that uncertainty in the fitting will increase. After the noise is powerful enough the algorithm might fail to converge, but when convergence does occur it offers good estimates on the size of the defect.

6. References

A, M., et al. (2004). "Fatigue damage detection in graphite/epoxy composites using sonic infrared imaging technique." Comp Sci Tech **64**: 19.

Carslaw, H. S. and J. C. Jaeger (1959). Conduction of heat in solids, Clarendon Press.

Castanedo, C. I., et al. (2011). "Delamination detection and impact damage assessment of GLARE by active thermography." International Journal of Materials and Product Technology **41**(1/2/3/4): 5.

Celorrio, R., et al. (2013). "Characterization of vertical buried defects using lock-in vibrothermography: II. Inverse problem." Measurement Science and Technology **24**(6): 065602.

Favro, L. D., et al. (2000). "Infrared imaging of defects heated by a sonic pulse." Review of Scientific Instruments **71**(6): 2418.

Han, X. (2007). Sonic infrared imaging: a novel NDE technology for detection of cracks/delaminations/disbonds in materials and structures. Ultrasonic and advanced methods for nondestructive testing and material characterization. C.-H. Chen, World Scientific.

Li, T., et al. (2011). "Crack imaging by scanning laser-line thermography and laser-spot thermography." Measurement Science and Technology **22**(3): 035701.

Maldague, X. P. (2012). Nondestructive evaluation of materials by infrared thermography, Springer Science & Business Media.

Mendioroz, A., et al. (2013). "Characterization of vertical buried defects using lock-in vibrothermography: I. Direct problem." Measurement Science and Technology **24**(6): 065601.

Mendioroz, A., et al. (2015). "Characterization of rectangular vertical cracks using burst vibrothermography." Review of Scientific Instruments **86**(6): 064903.

Moré, J. J. (1978). The Levenberg-Marquardt algorithm: implementation and theory. Numerical analysis, Springer**:** 105-116.

P, P. J., et al. (2008). "Nondestructive testing of open microscopic cracks in plasma-sprayed-coatings using ultrasound excited vibrothermography." Nondestr Testing Eval **23**(2): 20.

Reifsnider, K., et al. (1980). The mechanics of vibrothermography. Mechanics of nondestructive testing, Springer**:** 249-276.

Schlichting, J., et al. (2011). "Efficient data evaluation for thermographic crack detection." Quantitative InfraRed Thermography Journal **8**(1): 119-123.

Wang, Y. Q., et al. (1990). "Flying Laser Spot thermal Wave IR Imaging of Horizontal and Vertical Cracks." 511-516.

Conclusions

Through multiple experimental set-ups this work has shown the ability to use imaging devices to accurately apply thermal science so that thermal characterization of materials and sub-superficial defect detection may be performed.

Chapter 2 established that imaging devices can be used to instrument mirage-effect based experiments. In beam-deflection experiments lock-in amplification has been done programmatically as a post-processing technique, allowing the use of non-scientific cameras to monitor the refractive index variations in a medium surrounding a sample undergoing thermal testing.

The shadowgraph method using lock-in amplification has been successfully applied to the thermal characterizations of opaque filaments, seemingly, the first time this application has been given to it. The phase slope method may be applied with extremely good result using a scientific grade camera. Additionally lock-in software was developed to use a common webcam as the detector obtaining encouraging results. This is an important part of this work given that implementing these types of techniques using simple tools allows for a wider spread, including laboratories with low funding and educational facilities.

Chapter 3 demonstrated that the flash technique in a frontal configuration using a fast thermal imaging camera and using thermal mismatch with a liquid may recover both, thermal diffusivity and effusivity. Averaging of many pixels results in a low noise level that allows for the fitting algorithms to recover the values with good accuracy. It also showed that the technique may be used to quantify relative variations in samples such as polymer composites enriched with carbon nanofibers. This work also showed that fluid coupling can be utilized to characterize samples under different experimental regimes. Poor heat conductors have been successfully characterized by using lock-in thermography and air as the coupling fluid.

Chapter 4 verified the capacity to size defects in a metal piece using a thermographic camera and ultrasonic excitation. The encouraging results show an important application of thermal imaging in NDT. The fast measurements result in a highly convenient method that shows great promise for future development.

List of research products

Journal Articles

Published

1 Cifuentes, A., and Marín, E.: 'Implementation of a field programmable gate array-based lock-in amplifier', Measurement, 2015, 69, pp. 31-41

2 Pech-May, N.W., Cifuentes, Á., Mendioroz, A., Oleaga, A., and Salazar, A.: 'Simultaneous measurement of thermal diffusivity and effusivity of solids using the flash technique in the front-face configuration', Measurement Science and Technology, 2015, 26, (8), pp. 085017

3 Vaca-Oyola, L., Marín, E., Rojas-Trigos, J., Cifuentes, A., Cabrera, H., Alvarado, S., Cedeño, E., Calderón, A., and Delgado-Vasallo, O.: 'A liquids refractive index spectrometer', Sensors and Actuators B: Chemical, 2016

4 Pech-May, N.W., Vales-Pinzón, C., Vega-Flick, A., Cifuentes, Á., Oleaga, A., Salazar, A., and Alvarado-Gil, J.J.: 'Study of the thermal properties of polyester composites loaded with oriented carbon nanofibers using the front-face flash method', Polymer Testing, 2016

5 Mendioroz, A., Celorrio, R., Cifuentes, A., Zatón, L., and Salazar, A.: 'Sizing vertical cracks using burst vibrothermography', NDT & E International, 2016, 84, pp. 36-46

6 Cifuentes, A., Marín, E., Cabrera, H., Alvarado, S., and Calderón, J.: 'Thermal Diffusivity Measurement By Lock-in Photothermal Shadowgraph Method', Journal of Applied Physics, 2016, 119, (16), pp. 164902

Under review and in process for publishing

1 Cifuentes, A., Mendioroz, A., Salazar, A.: 'Simultaneous measurements of the thermal diffusivity and conductivity of thermal insulators using lock-in infrared thermography', International Journal of Thermal Sciences.

International Conferences

1 Mendioroz, A., Celorrio, R., Cifuentes, A., Zatón, L., and Salazar, A.: 'Application of burst vibrothermography to characterize planar vertical cracks', (International Society for Optics and Photonics, 2016, edn.), pp. 98610E-98610E-98610

2 Cifuentes, A., Vargas, E., Marín, E., Alvarado, S., Cabrera, H., Delgado, O., and Calderon, A.: 'A Lock-In CCD Camera Based Method for Thermal Diffusivity Measurement by an Improved Photothermal Beam Deflection Slope Method'. Proc. 12th International Conference on Heat Transfer, Fluid Mechanics and Thermodynamic, HEFAT 2016, Costa del Sol, Spain, 2016

3 Mendioroz, A., Celorrio, R., Cifuentes, A., and Salazar, A.: 'Fast geometrical characterization of vertical cracks using burst vibrothermography'. Proc. 2016 Quantitative Infrared Thermography, Poland, 2016

Awards

1 2013 Best Software Award, XERXES, National Polytechnic Institute, Mexico City.
2 2016 Best Paper Award, Application of burst vibrothermography to characterize planar vertical cracks, Thermosense: Thermal Infrared Applications XXXVIII, Baltimore, USA.
3 2016 Best Poster Award, Thermal Diffusivity Measurement by Lock-in Photothermal Shadowgraph, IX International Conference on Surfaces, Materials and Vacuum, Mazatlán, Mexico.
4 2017 Best Poster Award, Thermal Diffusivity Measurement by Lock-in Photothermal Shadowgraph, ICTP Winter College on Optics, Trieste, Italy.

Research Stays

1	Nov-2014 to May-2015	University of the Basque Country, Bilbao, Spain
2	Mar-2016 to May-2016	University of the Basque Country, Bilbao, Spain
3	Feb-2017	ICTP Winter College on Optics, Trieste, Italy